

# Relativistic interaction of ultra-short laser pulses with nanostructured solids

---

## Dissertation

zur Erlangung des akademischen Grades

*Doctor rerum naturalium (Dr. rer. nat.)*



---

vorgelegt dem Rat der

Physikalisch-Astronomischen Fakultät  
der Friedrich-Schiller-Universität Jena

von Dipl.-Phys. Ing. Zhanna Samsonova  
geboren am 11.04.1991 in Oblast Moskau, UdSSR

## Gutachter

1. Prof. Dr. Christian Spielmann  
Institut für Optik und Quantenelektronik  
Friedrich-Schiller-Universität Jena, Deutschland
2. PD Dr. Vincent Bagnoud  
Plasmaphysik Abteilung  
GSI Helmholtzzentrum für Schwerionenforschung GmbH  
Technische Universität Darmstadt, Deutschland
3. Prof. Dr. Victor A. Malka  
Department of Physics of Complex Systems  
Weizmann Institute of Science, Israel

Tag der Disputation: 8. März 2019

*In loving memory of my mother*





# Abstract

Relativistic interaction of ultra-intense laser pulses with nanostructured solids is widely considered to be one of the most promising directions for research in high energy density physics. This thesis investigates the influence of the target morphology on the plasma parameters and produced hard X-ray emission. The study is rather broad and covering a range of emerging applications such as a development of efficient X-ray sources and generation of the extreme states of matter for laboratory astrophysics.

We have performed a sequence of experimental campaigns starting from a benchmark experiment at moderate laser intensities and continuing with measurements at relativistic intensities ( $I\lambda^2 \geq 1.3 \times 10^{18} \text{ Wcm}^{-2}\mu\text{m}^2$ ).

A set of fundamental questions regarding the laser energy absorption and morphology dependent plasma dynamics were addressed. Measurements of the bremsstrahlung emission and K-shell emission helped to draw some very important conclusions. First of all, nanowire targets are impractical for the generation of the cold line emission since they demonstrate essentially the same photon flux as the flat targets. However, according to the detected emission from the highly charged ion states (He- and H-like), nanowire morphology enables an effective generation of hot dense plasmas. Spectroscopic analysis of the produced X-ray emission, as the main diagnostic tool, revealed keV temperatures and solid density ( $\geq 10^{23} \text{ cm}^{-3}$ ) plasmas. In fact, such plasmas can be generated also with a planar target, however only in a thin top layer since the laser cannot deposit energy deeper. The use of NW arrays, on the other hand, increases the laser energy absorption and the interaction volume, resulting in an effective plasma heating, which does not take place for the flat targets. We have also experimentally observed higher flux and higher energies of the ions accelerated away from the front surface of the target matching with the other observations.

The experimental results were supported by numerical simulations. For the chosen

cases, we have synthesized X-ray line spectra using the plasma parameters provided by the Particle-in-Cell (PIC) and Hydrodynamic (HD) simulations. A good correlation between the measured and synthetic spectra has been achieved. The plasma dynamics for the case of flat and nanostructured solids is strikingly different. For hot high-density plasmas, the collisional rates (e.g., ionization, excitation) are high and, therefore, radiative cooling of the plasmas may overrun hydrodynamic cooling, as it happens for nanowire targets. This naturally causes a great increase in the X-ray yield.

The response of the flat and nanowire targets was investigated in the interaction with short- and long-wavelength laser pulses (0.4  $\mu\text{m}$  and 3.9  $\mu\text{m}$ ), corresponding to completely different regimes of interaction. While ultra-short laser pulses in UV, visible and near-infrared are commonly used in laser-induced plasma studies, femtosecond mid-infrared pulses have not been yet extensively applied. In this thesis, we highlight the potential of such long-wavelength drivers to generate hot and dense plasmas. We demonstrate that this becomes feasible only with nanowire targets.

# Zusammenfassung

Die relativistische Wechselwirkung von ultra-intensiven Laserpulsen mit nanostrukturierten Festkörpern wird weithin als eine der vielversprechendsten Forschungsfelder im Bereich der Physik der Plasmen hoher Energiedichte angesehen. Diese Dissertation untersucht den Einfluss der Target-Morphologie auf die erreichten Plasmamparameter und die erzeugte Emission harter Röntgenstrahlung. Die durchgeführten Untersuchungen decken ein weites Gebiet an Themen ab und behandeln ebenfalls die sich daraus eröffnenden Einsatzmöglichkeiten, z.B. die Entwicklung effizienter laserbasierter Röntgenquellen oder die Erzeugung von extremen Materiezuständen im Labor für astrophysikalische Fragestellungen.

Im Rahmen dieser Arbeit wurde eine Reihe von Experimentkampagnen durchgeführt, die mit einem Benchmark-Experiment bei moderaten Laserintensitäten angefangen haben und dann zu Messungen bei relativistischen Intensitäten von  $I\lambda^2 \geq 1,3 \times 10^{18} \text{ Wcm}^{-2}\mu\text{m}^2$  ausgeweitet wurden.

Mehrere fundamentale Fragen bezüglich der Absorption von Laserenergie und der Dynamik des erzeugten Plasmas in Abhängigkeit von der Morphologie wurden behandelt. Messungen der Bremsstrahlungs- und der K-Schalen-Emission haben dabei geholfen, unter anderem folgende wichtige Erkenntnisse zu erlangen: Zunächst weisen nanostrukturierte Targets im Vergleich zu flachen Targets keinen ausgeprägt höheren Photonenfluss an kalter Linienemission auf. Die Emission, die von hochgeladenen Ionen stammt (helium- und wasserstoffähnlich), ist jedoch wesentlich stärker. Dies offenbart, dass bedingt durch die Nanodraht-Morphologie heiße und dichte Plasmen erzeugt wurden. Die spektroskopische Analyse der Röntgenemission (unsere Hauptuntersuchungsmethode) zeigte, dass Plasmen von keV Temperaturen und Festkörperdichte ( $\geq 10^{23} \text{ cm}^{-3}$ ) vorlagen. Solche Plasmabedingungen können zwar auch mit flachen Targets erreicht werden, jedoch nur in einer dünnen oberflächlichen Schicht. Nanodraht-Anordnungen hingegen ermöglichen es, dass der Laser wesentlich mehr Energie in einem wesentlich größeren Volumen

deponieren kann, wodurch das Plasma effektiv aufgeheizt wird. Neben diesem Ergebnis haben wir einen höheren Fluss und höhere Energien von Ionen beobachten können, die von der Vorderseite des Targets wegbeschleunigt wurden. Dies deckt sich mit den anderen Beobachtungen.

Die experimentellen Ergebnisse wurden durch numerische Simulationen unterstützt. Für bestimmte ausgewählte Bedingungen wurden Röntgen-Linienspektren synthetisiert, indem die aus PIC und HD Simulationen gewonnenen Plasmaparameter verwendet wurden. Dabei konnten wir eine gute Übereinstimmung zwischen experimentellen und synthetischen Spektren erzielen. Die Dynamik des Plasmas ist stark unterschiedlich, wenn nanostrukturierte und flache Targets verglichen werden. In heißen Plasmen mit einer hohen Dichte sind die Kollisionsraten (z.B. Ionisation, Anregung) hoch und dementsprechend wird das Abkühlen des Plasmas durch ausgehende Strahlung über das hydrodynamische Abkühlen dominieren, so wie es bei der Verwendung von Nanodraht-Targets der Fall ist. Die Konsequenz ist ein ausgeprägter Anstieg der Röntgenausbeute.

Schlussendlich wurde das Verhalten untersucht, wenn die beiden Target-Morphologien mit Laserpulsen kurzer und langer Wellenlänge ( $0,4 \mu\text{m}$  und  $3,9 \mu\text{m}$ ) beschossen wurden. Dies entspricht zwei komplett unterschiedlichen Wechselwirkungsregimen. Während ultra-kurze Laserpulse im UV, sichtbaren oder nahem Infrarot Bereich weit verbreitet sind, um Plasmen zu erzeugen und zu untersuchen, wurden femtosekundenlange Pulse im mittleren IR Bereich noch kaum eingesetzt. In dieser Dissertation wird das Potential gezeigt, das solche Laser bei der Erzeugung von heißen und dichten Plasmen mit sich bringen. Es wurde dabei herausgearbeitet, dass jedoch erst die Verwendung von Nanodraht-Targets den Einsatz solcher Laser praktikabel macht.

# Acknowledgement

Since it would be impossible to name everyone, who made this work possible and have supported me over the past years, within a couple of pages, I would like to use this opportunity and thank you all. It has been 4 years (and a little bit) of unforgettable experience embracing all aspects of my life.

Foremost, I would like to express my sincere gratitude to my advisor Prof. Dr. C. Spielmann who gave me the possibility to join his (Quantum Electronics) group and work on the project I am truly excited about. All those years you have been strongly motivating me with your vital enthusiasm and great ideas. I would like to thank you for the firm belief and encouragement in work helping me to recognize my own achievements.

I am deeply grateful to Dr. D. Kartashov. Without your careful supervision and useful critiques, I would not have pushed this project to the point it is now. Your wealth of knowledge has been always fascinating me. You have made it available to me and I hope I managed to gain some of it. I could always rely on you and your aid whether it be a work-related issue or a private one.

My heartfelt appreciation goes to Dr. O. Rosmej who became my “Doktormutter” in every sense of the word. It is hard to overestimate the input you made when opening for me a field of X-ray spectroscopy and related fun. Our discussions served as an everlasting source of inspiration for me.

I want to thank Dr. S. Höfer with whom I have performed my first experiments on X-ray generation. We owe you a debt of gratitude for willingness to share with me your great experience and endless positivity. Your ability to find a feasible solution to any arising problem has saved the situation time after time. It has been always a pleasure to work with you, be it a scientific experiment or some hobby project.

I surely cannot overlook my awesome colleagues from the Quantum Electronics group who created a warm atmosphere and an environment in which I felt comfortable from the very first day. Some of you have already left the university, the others

are still around. However, I will always keep the memories of our marvelous time together alive: our shared moments, ups and downs, rare yet great parties, movie-nights, barbecues, restless experimental campaigns and much more... Thank you, guys!

I would like to acknowledge the support of the RS-APS (Helmholtz Institute Jena) and all representatives who were ready to answer my numerous questions. I would like to extend my sincere thanks to Sarah Dürer, the best secretary and a wonderful person. I cannot imagine coping with paperwork without you :P

I strongly appreciate the help of the colleagues from other institutes and universities whose contribution played a decisive role in this work: Dr. R. Löttsch, Dr. I. Uschmann, Prof. Dr. Förster, C. Hanh, Dr. A. Sävert, Dr. J. Polz, G. Becker, F. Ronneberger, B. Beleites, Dr. R. Röder, L. Trefflich, Prof. Dr. C. Ronning, Jun.-Prof. Dr. S. Kroker, T. Siefke, V. Kaymak, Prof. Dr. A. Pukhov, Dr. D. Khaghani, Dr. P. Neumeyer, Prof. Dr. T.Kühl, Dr. A. Pugžlys, Prof. Dr. A. Baltuška... Without your kind collaboration and assistance, it would be essentially not possible to proceed. Furthermore, I would like to thank my friends, those whom I met during my Ph.D. times and whom I know since ages. You saved me from feeling lonely in a new place, distracted me from the daily routines and brought a lot of joy in my life. Thank you all for your tremendous support and being there for me.

Last but not least I would like to thank my family which despite an awful bereavement has grown in number. I have never felt a lack of love and appreciation from your side. I am very thankful to my soul-mate, Björn, without whom I would not be able to manage with stress at the final stage of this work and whose moral and emotional support kept me safe and sound. I hope, the dream of my granddad will soon come true and I will finally accomplish what I have started here :)

Jena, 05.12.18

Zhanna S.

# Contents

<b>1</b>	<b>Introduction</b>	<b>3</b>
<b>2</b>	<b>Fundamentals</b>	<b>7</b>
2.1	The nuts and bolts of relativistic laser-matter interaction . . . . .	7
2.1.1	Ionization mechanisms . . . . .	8
2.1.2	Core concepts and measures in plasma physics . . . . .	11
2.1.3	Plasma absorption mechanisms . . . . .	14
2.1.4	Heat transport in plasmas . . . . .	20
2.1.5	Laser pulse contrast . . . . .	23
2.1.6	Methods of numerical simulations . . . . .	26
2.2	Atomic processes in plasmas . . . . .	28
2.2.1	Basics: Types of processes . . . . .	28
2.2.2	Elements of population kinetics. FLYCHK code . . . . .	37
<b>3</b>	<b>Non-relativistic proof-of-principle experiment</b>	<b>40</b>
3.1	Towards compact plasma-based hard X-ray sources . . . . .	40
3.2	Experimental setup . . . . .	42
3.3	Influence of the target morphology on the produced X-ray emission .	46
3.4	Conclusions . . . . .	53
<b>4</b>	<b>Relativistic interaction with short-wavelength (UV) pulses</b>	<b>55</b>
4.1	Interaction with planar foils . . . . .	55
4.1.1	Measurements & Simulations . . . . .	57
4.2	Studies with nanostructured targets . . . . .	62
4.2.1	Experimental setup & Targets . . . . .	63
4.2.2	Pilot experiment: normal incidence geometry . . . . .	67
4.2.3	Experiments with complex diagnostics . . . . .	69
4.2.4	Si plasma: towards Rydberg states . . . . .	72
4.2.5	Ion generation . . . . .	73

4.3	Conclusions . . . . .	76
<b>5</b>	<b>Relativistic interaction with long-wavelength (mid-IR) pulses</b>	<b>77</b>
5.1	Novel regime of interaction: <i>pro et contra</i> . . . . .	78
5.2	Experimental setup . . . . .	80
5.3	X-ray emission spectra . . . . .	83
5.4	Simulations of the plasma parameters . . . . .	87
5.5	Discussions . . . . .	95
<b>6</b>	<b>Summary &amp; Perspectives</b>	<b>97</b>
	<b>Appendices</b>	<b>101</b>
A	Few-electron ions: transitions . . . . .	101
B	Targets fabrication . . . . .	104
C	JETi-40 laser system . . . . .	106
D	Crystal spectrometers & X-ray detectors . . . . .	107
E	Thomson parabola spectrometer . . . . .	112
F	Reconstruction of X-ray spectra . . . . .	113
G	Target damage introduced during the interaction . . . . .	115
	<b>References</b>	<b>117</b>



# Introduction

“ *Nothing is too wonderful to be true.* ”

— **Michael Faraday**  
(Physicist and chemist)

Lasers have come a long way to improve the performance, increase output energy and get around arising flaws since its invention. The method of chirped-pulse amplification (CPA) invented in mid-80s by D. Strickland and G. Mourou [Strickland85] has become one of the most exciting breakthroughs. This invention has been recognized by the Nobel prize in physics only this year, however, it had already been done a revolutionary impact in strong-field laser science. Many laboratories worldwide have terra- and even petawatt peak power CPA laser systems, with which intensities of  $10^{16}$ - $10^{21}$  W/cm<sup>2</sup> in a several micron focal spot can be achieved. Thanks to this development, various investigations of light-matter interactions on an ultra-short timescale became possible. At high intensities, the matter can be transformed into a highly excited plasma state with just a single laser pulse. This phenomenon is of great interest for a number of applications and fundamental research such as experiments on astrophysics [Remington99; Gregori12] and nuclear fusion [Dittrich94; Ditmire99; Koenig04; Roth13], ultrafast X-ray generation [Pfeifer06], charged particle production and acceleration [Fuchs05; Macchi13; Malka12], and development of efficient plasma-based X-ray lasers [Suckewer09; Zielbauer11; Corde13].

A problem of an effective and rapid energy transfer to matter lies at the center of these investigations since a generation of simultaneously hot (keV) and dense plasmas is rather challenging. For instance, such plasmas can be produced by spherical compression in fusion experiments [Fujioka09; Glenzer10] applying MJ laser pulses at facilities like National Ignition Facility (NIF), GEKKO-XII laser facility or using supersonic heating [Guethlein96; Young98]. The major drawbacks of these approaches are either complexity of experiments and low availability for users or generation of only a small layer of hot and dense plasmas ( $\leq 0.1$   $\mu\text{m}$ ), which is a

fundamental problem. It is well-known that laser radiation cannot access into a plasma far beyond critical density. When ultra-intense laser pulse interacts with a flat solid surface, a thin plasma layer is formed on the leading pulse front. Once the plasma reaches the critical density, the penetration depth of the laser pulse is limited by roughly a skin depth.

A lot of efforts were put into investigations of the ways to overcome it. It has been suggested already over twenty years ago to use structuring of the target surface and at early stages, these attempts were done with microstructured targets [Gordon94; Gavrilov04; Klimo11]. Nanophotonics opens a new chapter in this research giving new groundbreaking perspectives. Early experiments have shown a positive influence of nano-scale roughness and nanostructuring of the target surface on the yield of X-ray line and bremsstrahlung emission [Kulsar00; Nishikawa04; Khattak05; Rajeev02; Rajeev03]. First exciting results triggered further intensive studies with various target morphologies, in particular, with nanowires (NWs) or nanorods [Rasuchine09; Mondal11; Chakravarty11; Cristoforetti14]. The research went beyond the generation of X-ray emission involving new appealing perspectives with NWs, among which hot electron generation [Jiang14a; Jiang16; Sarkar17], ion and proton acceleration [Zigler11; Khaghani17; Luebcke17], neutron production [Curtis18]. For all these studies, an effective laser energy absorption and resulting plasma parameters are the key points.

It was argued that nanowire arrays of a micron scale length allow an effective increase in the penetration depth of the laser energy leading to the so-called volumetric plasma heating [Purvis13; Bargsten17]. As a result, electron densities up to two orders of magnitude above the critical one with multi-keV temperatures can be reached. In Fig. 1.1 an interaction of intense laser pulses with solids (flat and nanowire targets) is illustrated. Vertically oriented NW arrays appear to be the most advantageous morphology. Instead of interacting just with the top surface, a laser pulse can penetrate in between NWs and interact with a larger volume. Firstly, the laser pulse energy is deposited to the regions close to the tips of the NWs and goes deeper into the structure. Propagating along the NWs, it frees electrons by optical field ionization and accelerates them into the gaps between the NWs. These electrons either return back to the parental NW or meet a neighboring NW, where they lose their energy in collisions. The electron density rapidly grows and a hot dense plasma is generated. Meanwhile, the NWs radially expand with the velocity which is defined by the reached electron temperature. If the laser field is strong

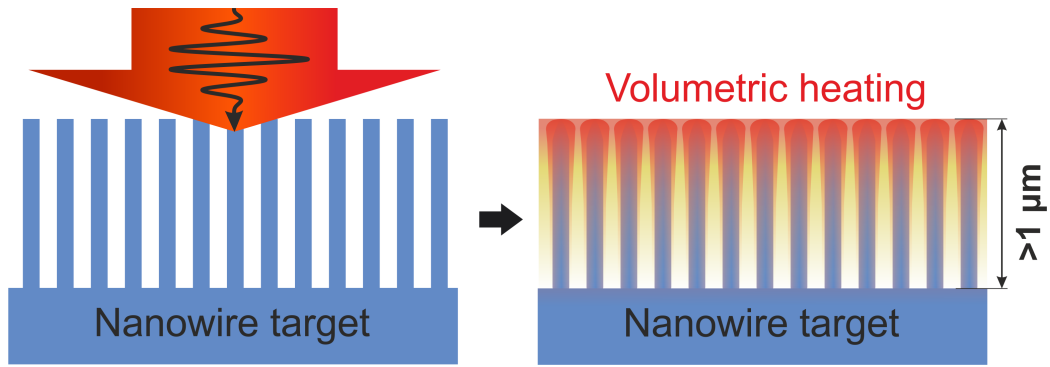


**Fig. 1.1:** Illustration of the interaction of an intense laser pulse with a nanowire solid target.

enough, it induces a return current along the NWs which forms a magnetic field forcing the electrons to stay inside the NWs. The strength of this pinching effect scales with the laser field amplitude and may even cause compression of plasmas [Kaymak16]. The laser pulse can access the volume as long as the gaps between the NWs are free from overcritical-density plasma. To exploit the potential of NW targets it is necessary to have a high contrast laser pulse ( $> 10^{-9}$  for relativistic intensities in the visible-IR spectral range). Ultra-high temporal contrast prevents ionization of the target at the leading front of the pulse and ensures the survival of nanostructures till peak intensity arrival.

Despite the interest, there is still no well-grounded explanation of the sophisticated physical phenomena taking place within and after interaction of ultra-short intense pulses with nanowire arrays. In this thesis, we investigate the possibility to generate ultra-dense and ultra-hot plasmas and hard X-ray emission from nanowire and polished solid targets illuminated by relativistically strong femtosecond laser pulses with high temporal contrast. Employing experimental methods of X-ray spectroscopy and numerical simulations of relativistic laser-plasma interaction and subsequent plasma kinetics, we provide explicit proves and investigate conditions when (and whether) unique plasma parameters predicted in [Purvis13] can be reached with nanowire solid targets.

The structure of this thesis is as follows. In **Chapter 2** some fundamental questions related to the laser-matter interaction and atomic process in plasmas are discussed. The main physical parameters, terms and effects specific to laser-induced plasmas will be introduced. In **Chapter 3** the first pilot experiment on hard X-ray generation with targets of different morphologies is described. The measurements were performed at non-relativistic intensities and are meaningful for further studies at higher intensities discussed in the subsequent chapters. **Chapter 4** presents the series of

experiments carried out with a short-wavelength (400 nm) laser driver. It opens with a description of the experiment with flat Ti foils, which serves as a starting point for the discussion of a relativistic interaction with solids. The obtained results and accompanying simulations implying X-ray spectroscopy tools are given in detail. The chapter proceeds with the findings regarding the plasma generated with nanowire and polished solid targets. The complex experimental setup is outlined. The experimental results on X-ray and ion generation with different target materials (ZnO and Si) are discussed. **Chapter 5** presents the novel regime of interaction when a long-wavelength (3.9  $\mu\text{m}$ ) laser was employed. The advantages of such a regime are first discussed and then demonstrated with experimental results and X-ray spectrum modeling. **Chapter 6** summarizes the main results and draws conclusions of this thesis. Finally, an outlook for further investigations is provided.

” *In theory, there is no difference between theory and practice. But, in practice, there is.*

— **Jan L. A. van de Snepscheut**  
(Computer scientist)

In this chapter, the theoretical framework and basic concepts relevant to this thesis are presented. The first Section 2.1 introduces the key aspects of the laser-matter interaction, turning to electrodynamics and plasma physics. The thesis focuses on X-ray emission measurements and X-ray spectroscopy. In order to address this topic with sufficient understanding, an overview of the atomic processes taking place in plasmas are given in Section 2.2.

## 2.1 The nuts and bolts of relativistic laser-matter interaction

The physics considered in this section is related to the interaction of intense ultra-short laser pulses with solids. The regime of interaction with solids is radically different from the one present with low-density gases. In this case, the interaction with a volume of the target is significantly affected by the interaction with the surface. The rapid ionization of the material by the field of the ultra-short laser pulse forms a plasma at its surface and so even initially transparent materials become reflective. Therefore, a considerable part of the laser energy might get reflected like from a mirror. To understand the dynamics of the plasma formation and heating, it is useful to start with the basic processes occurring within the interaction of a single electron or an atom with a laser pulse. However, we do not go into details and describe these fundamental principles giving only general terms. Instead, the attention is drawn to the collective effects in plasma, in particular, ionization and absorption mechanisms as well as heat transport. Keeping in mind the importance

of laser-plasma interaction at the surface, we address the problem of laser intensity contrast as one of the crucial points for experiments presented in this thesis. The section is completed with a brief overview of the existing approaches to numerical simulations of laser-matter interactions and a short description of the core concept of Particle-in-Cell codes. Our discourse is broadly inspired by the textbooks of laser-induced plasmas [Gibbon05; Kruer88; Chen84; Eliezer02].

## 2.1.1 Ionization mechanisms

The plasma generation implies the creation of free electrons – ionization. Generally, one has to distinguish two categories of the ionization processes: optical ionization caused by the laser field and electron impact ionization due to the collisions of free electrons with atoms and ions. Focused on a solid target, a high power laser pulse rapidly ionizes the matter at the leading front of the pulse. Later on, the ionization proceeds via collisions of the heated electrons with the atoms/ions of the target material. Therefore, the ionization is normally a combination of several time-dependent ionization processes.

### Optical ionization

The most familiar process of the light-matter interaction is the *photoelectric effect* discovered by Einstein about a hundred years ago [Einstein05]. When the photon energy  $\hbar\omega_L$  in the incident light matches the height of the atomic potential barrier (or ionization potential  $I_p$ ), the ejection of an electron from an atom occurs. This is a resonant process. For the outer shells of most elements, this energy lies in the ultraviolet (UV) range corresponding to tens of eV, for inner shells – keV. Therefore, to induce *photo-ionization* in most materials one photon from a standard laser source operating in the infrared/visible/UV spectral range is not enough. This is a situation relevant for this thesis, while the shortest used wavelength was 400 nm ( $\sim 3.1$  eV). Thus, high intensities of laser pulses are required for ionization to take place. In such a regime, *multiphoton ionization* (MPI) and *tunnel ionization* (TI) are the two limiting cases of the ionization process. The regime of ionization is determined by so-called *Keldysh parameter*  $\gamma$  [Keldysh65]:

$$\gamma = \omega_L \frac{\sqrt{2mI_p}}{eE_L} \sim \sqrt{\frac{I_p}{2U_p}}, \quad (2.1)$$

where  $E_L$  and  $\omega_L$  are the amplitude of the laser field and its frequency,  $U_p$  is the ponderomotive potential,  $m$  and  $e$  are the electron charge and mass. It is generally used to separate the two regimes: TI is the ionization mechanism for  $\gamma < 1$ , while MPI prevails for  $\gamma > 1$ .

At high intensities of laser radiation, an electron bounded by Coulomb potential can be freed by absorbing multiple low-energy photons. The probability of the MPI strongly depends on the laser pulse intensity  $I_L$  and in the lowest-order perturbation-theory (LOPT) [Faisal76] the ionization rate is given by:  $\Gamma_n = \sigma_n I_L^n$ . The cross-section  $\sigma_n$  for the  $n$ -photon interaction decreases with  $n$  balancing the growth of  $I_L^n$ . The process is illustrated in Fig. 2.1(a). For high intensities, the number of photons absorbed by an electron can be higher than the required for the MPI number (see Fig. 2.1(b)). This effect is called *above-threshold ionization* (ATI). The ejected electrons, in this case, have discrete kinetic energies and would reveal themselves in the photoelectron spectrum. The MPI process reaches saturation when the probability for a pulse of effective duration  $\tau_L$  is equal to 1:  $\sigma_n I_L^n \tau_L = 1$ . In contrast to MPI, tunnel ionization considers the influence of the laser electric field. This regime of ionization is typically realized for low-frequency fields when photon energy is negligible in comparison to ionization potential. It is typical for mid-IR and longer wavelengths or for near-IR radiation interacting with ions. An electron can tunnel directly through the potential barrier formed by the Coulomb potential and the interaction potential with the laser electric field. The corresponding ionization process is called *tunnel ionization*. While MPI is based on quantum nature of light and resembling an extension of Einstein's photoeffect to multiphoton absorption regime, tunnel ionization is governed by the classical Coulomb force of electric field in the laser pulse and occurs entirely due to quantum nature of

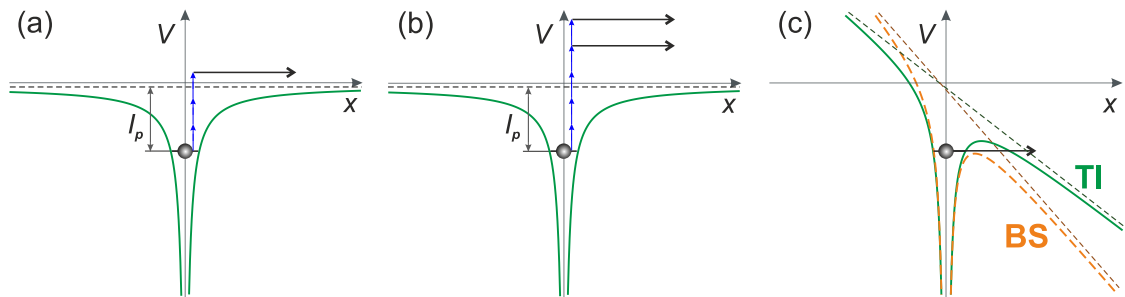


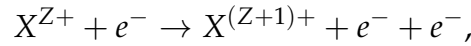
**Fig. 2.1:** Schematic picture of different regimes of the optical ionization: (a) multiphoton ionization, (b) above-threshold ionization, and (c) tunnel and barrier-suppression ionization.  $V$  is the effective potential which, in the cases of TI and BS, is equal to the ionization potential  $I_p$  or falls below it at a certain position, respectively.

electrons. If the potential barrier falls below the ionization potential  $I_p$  under the influence of the laser field, the electron can directly leave the parental atom, without tunneling – this phenomenon is known as *barrier-suppression* (BS) or *over-the-barrier* (OB) *ionization* (Fig. 2.1(c)).

Well-known Perelomov-Popov-Terentiev (PPT) model [Perelomov66] (and later the Ammosov-Delone-Krainov (ADK) model [Ammosov86]) considers the discussed above effects of the ionization of the complex atoms in strong laser fields and provides a general formula widely used for simulations.

## Electron impact ionization

High energy free electrons freed in the process of the photoionization and heated up by the laser pulse enable *electron impact ionization* mechanism. Such electrons collide with an ion or an atom and kick out the bound electrons into the continuum. This ionization mechanism can be described by the scheme:



where the superscript  $Z$ ,  $(Z + 1)$  denote the ionization stages of the ion  $X$ . Generally, the ionization rate can be expressed as:  $R = n_e \langle v_e \sigma_{Z \rightarrow Z+1} \rangle$ , where  $v_e$  is the electron velocity,  $\sigma_{Z \rightarrow Z+1}$  is the collisional cross-section. The cross-section for the impact ionization can be calculated using the semi-empirical Lotz formula [Lotz67a]:

$$\sigma_{Z \rightarrow Z+1} = 4.15 \times 10^{-14} \sum_{i=1}^N \frac{\ln(E_{kin} / I_p^i)}{E_{kin} I_p^i} [\text{cm}^2] \quad (2.2)$$

where  $E_{kin}$  is the kinetic energy of the free electron in eV,  $N$  is the number of the electrons in a given shell,  $I_p^i$  is the ionization potential for the bound electrons. It is clear from Eq. 2.2 that the collisional cross-section  $\sigma_{Z \rightarrow Z+1}$  has a maximum at a certain energy which corresponds to the optimal energy  $E_{opt}$  satisfying the relation:

$$E_{opt} \approx e \cdot \exp \frac{\sum_{i=1}^N (\ln I_p^i) / I_p^i}{\sum_{i=1}^N 1 / I_p^i} \approx e I_p. \quad (2.3)$$

Thus, the optimal electron energy for the collisional ionization up to  $(Z + 1)$  state is nearly  $e$ -times the ionization energy  $I_p$  of  $X^{Z+}$ . For the illustration, we calculated the collisional cross-sections for ionization of the last electron in the L-shell and the first electron in the K-shell for the elements we deal with in this thesis – Si



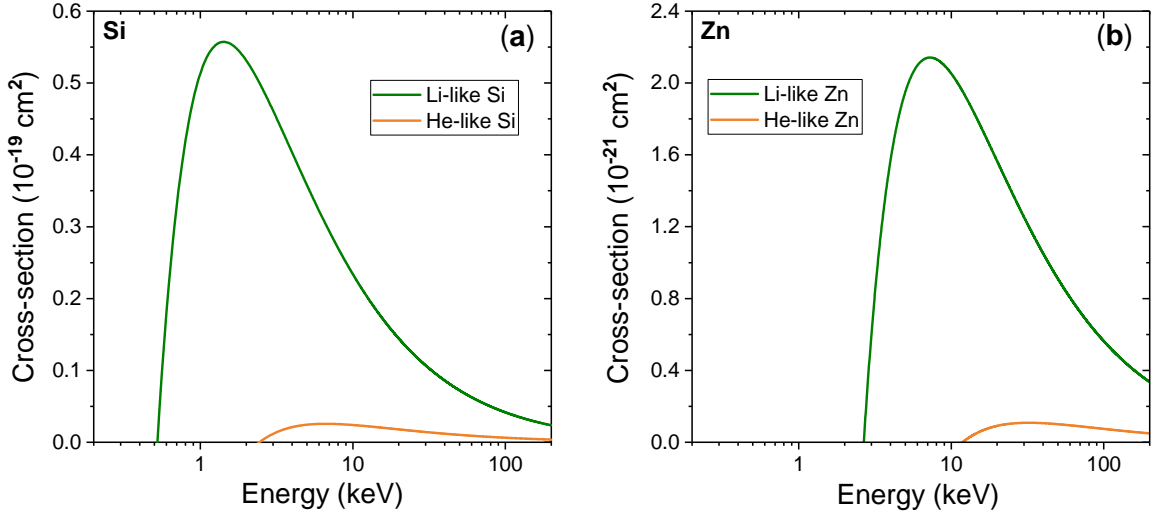


**Fig. 2.2:** The collisional cross-sections for Li-like and H-like ions ((a) Si, (b) Zn) calculated according to the Lotz formula (Eq. 2.2).

and Zn (Fig. 2.2). The ionization potentials were taken from NIST Atomic Spectra Database [NIST]:  $I_p(\text{Si}^{11+}) = 0.52$  keV,  $I_p(\text{Si}^{12+}) = 2.44$  keV,  $I_p(\text{Zn}^{27+}) = 2.67$  keV,  $I_p(\text{Zn}^{28+}) = 11.86$  keV. The heavier the element is, the smaller  $\sigma_{Z \rightarrow Z+1}$  gets.

## 2.1.2 Core concepts and measures in plasma physics

After an electron got ejected from the parental atom or ion via some ionization channel, the laser field continues to govern its motion. If the laser field is weak (at low intensities), linear oscillations of free electrons will be at the same frequency as the driving frequency laser ( $\omega_L = 2\pi c/\lambda$ ). The motion of an individual electron in plasmas with an external electromagnetic (EM) field is given by the *Lorentz equation*:

$$\frac{d\vec{p}}{dt} = m \frac{d\vec{v}}{dt} = e \left( \vec{E} + \frac{\vec{v}}{c} \times \vec{B} \right), \quad (2.4)$$

where  $c$  is the speed of light (here and throughout the thesis),  $m$  denotes the electron rest mass,  $e$  is its charge;  $\vec{p}$  and  $\vec{v}$  are the electron momentum and velocity, respectively;  $\vec{E}$  is the electric field and  $\vec{B}$  is the magnetic field. In the non-relativistic scenario, i.e.  $v \ll c$ , the influence of the magnetic field  $\vec{B}$  can be neglected, so that the resulting motion is defined by the electric field  $\vec{E}$ . In fact, for the linearly polarized electric field, the velocity of the electron can be separated into two components, the average linear velocity  $\langle \vec{v} \rangle$  and the oscillation velocity  $\vec{v}_{\text{osc}}$ , where  $\vec{v}_{\text{osc}} \gg \langle \vec{v} \rangle$ . If we consider a high-frequency EM wave with an electric field component  $\vec{E}(\vec{r}, t) = E_0(\vec{r})\vec{e}_x \cos(\omega_L t - kz)$ , where  $\vec{e}_x$  is the unit vector defining the

polarization direction, the oscillatory solution of Eq. 2.4 to the first order approximation is:

$$\vec{v}_{\text{osc}} = -\frac{e}{m\omega_L} E_0 \sin(\omega_L t - kz) \vec{e}_x. \quad (2.5)$$

Taking an assembly of electrons in plasma instead of a single electron, the derivative of velocity  $\vec{v}$  with respect to time (in Eq. 2.4) can be expressed as the sum of two terms:  $\left(\frac{\partial}{\partial t} + \vec{v} \cdot \nabla\right) \vec{v}$ . Time-averaging of over the optical cycle of the laser field in this case results in:  $\frac{\partial \vec{v}}{\partial t} = -\langle \vec{v}_{\text{osc}} \cdot \nabla \vec{v}_{\text{osc}} \rangle = -\frac{1}{2} \nabla \langle v_{\text{osc}}^2 \rangle$ . Using then Eq. 2.5, we find a time-averaged apparent force proportional to the gradient of the electric field pressure:

$$\vec{F}_p = -\frac{e^2}{4m\omega_L^2} \frac{\partial}{\partial t} \langle E_0^2 \rangle \vec{e}_x, \quad (2.6)$$

which is called *ponderomotive force*. Note that the electron will oscillate at the laser frequency along the direction of the polarization vector.

Adding the second term  $\vec{v} \times \vec{B}$  in the Lorenz equation of motion (Eq. 2.4) (which was dropped earlier), causes a forward drift of the electron. The motion of the electron is then rather complicated but yet periodic. In the frame moving with the average drift velocity in the direction of the laser propagation  $\vec{k}$ , it can be described as a figure-eight motion in the plane  $(\vec{E}_0, \vec{k})$ . Applying a relation between  $\vec{B}$  field and  $\vec{E}$  (Maxwell's equation), we finally obtain a formula for the total *ponderomotive force*:

$$\vec{F}_p = -\frac{e^2}{4m\omega_L^2} \nabla \langle \vec{E}_0^2 \rangle. \quad (2.7)$$

It is often expressed as a minus gradient of a *ponderomotive potential*  $U_p = \frac{e^2 \vec{E}_0^2}{4m\omega_L^2} \sim I\lambda^2$ .

At high intensities, the quivering motion of the electron in the laser field becomes relativistic, e.g. at velocities close to the speed of light  $c$ . Thus, the drift motion along the laser propagation (longitudinal) begins to dominate the transverse motion. The ponderomotive force must be modified for the relativistic case:

$$\vec{F}_p = -\frac{e^2}{4m\langle\gamma\rangle\omega_L^2} \nabla \langle \vec{E}_0^2 \rangle, \quad (2.8)$$

where  $\langle\gamma\rangle \approx \sqrt{1 + a_0^2/2}$  is a cycle-averaged  $\gamma$ -factor defined by a dimensionless parameter – *normalized vector potential*  $a_0$ :

$$a_0 = \frac{v_{osc}}{c} = \frac{eE}{m\omega_L c}. \quad (2.9)$$

It is normally used to classify the regime of interaction. Physically,  $a_0$  defines the laser strength. When  $a_0 \approx 1$ , the dynamics of motion changes and the relativistic regime is entered. In terms of commonly used units, it reads:  $a_0 = 0.85 \times 10^{-9} \sqrt{I} \lambda$ , where  $I$  is the laser pulse intensity in  $\text{W}/\text{cm}^2$ ,  $\lambda$  is the wavelength of the laser light in  $\mu\text{m}$ . For 800 nm light, the relativistic regime starts at intensities  $I_L > 2.15 \times 10^{18} \text{ W}/\text{cm}^2$ . Note, the electron can gain the energy from the laser pulse only if its oscillatory motion is changed by collision with heavy particles in the plasma. Without collisions the electron motion remains in phase with the driving force, thus the electron being periodically accelerated and decelerated and left at the end of the laser pulse with zero balance of energy exchange with the laser field.

In a typical experiment on ultra-intense laser-matter interaction, the laser beam is focused and thus the laser intensity is not homogeneous in the transverse direction. A free electron is pushed out of the region with the highest intensity (focus) by the ponderomotive force. This results in two processes. On the one hand, the electron gains energy traveling between high- and low-intensity regions. On the other hand, the final direction of the electron motion depends on its energy. It has been shown that depending on a viewing angle it is possible to measure ejected electrons of different origin [Moore95; Malka97].

Additional to the Lorenz force triggering oscillations, the motion of electrons is affected by the fields generated due to the charge separation. Here the collective properties of the plasma come into play. One of the fundamental properties of plasmas is electrical quasi-neutrality. This means that the balance of ionic and electron charges can be violated only within a spatial scale of the *Debye length*:

$$\lambda_D = \sqrt{\frac{k_B T_e}{4\pi e^2 n_e}}, \quad (2.10)$$

where  $k_B$  is the Boltzmann constant,  $T_e$  is the electron temperature,  $n_e$  is the electron density. It can be rewritten in the form:  $\lambda_D[\text{cm}] = (T_e[\text{eV}]/n_e[\text{cm}^{-3}])^{1/2}$ . The collective electron density oscillations, caused by charge imbalance against the positive ion background, have a frequency:

$$\omega_p = \sqrt{\frac{4\pi e^2 n_e}{m}} \approx 5.64 \times 10^4 (n_e[\text{cm}^{-3}])^{1/2} [\text{s}^{-1}], \quad (2.11)$$

called *plasma frequency*. A plasma is termed overdense or overcritical if its electron density  $n_e$  is more than the critical density  $n_{cr} = \omega_L^2 m / 4\pi e^2$ . This definition originates from the expression for the refractive index of transversal electromagnetic waves in plasmas:  $n_{refr} = \sqrt{1 - \omega_p^2 / \omega_L^2}$ . Thus, for  $\omega_L < \omega_p$ , the refractive index becomes purely imaginary. Under this condition, the plasma becomes opaque for the EM wave (mirror-like) and shields the target volume from the laser field, strongly affecting the laser energy deposition into the material. In fact, the EM field interacts only with the upper layer and decreases exponentially on a characteristic *skin depth* (collisional):

$$l_s \simeq \frac{c}{\omega_p} \approx 1.68 \times 10^{-6} (n_e [10^{23} \text{cm}^{-3}])^{-1/2} [\text{cm}]. \quad (2.12)$$

The classical formula (Eq. 2.12) is valid only for the low plasma frequencies. However, when the skin depth becomes comparable or smaller than the electron mean free path (the average distance between two collisions of an electron with the other background particles), the penetration depth of the EM energy is determined by the *anomalous skin effect* (see Section 2.1.3).

### 2.1.3 Plasma absorption mechanisms

The laser energy coupling to plasma is one of the most vital research topics in high energy density (HED) physics. The importance of the understanding of the absorption mechanisms and the possibility to predict/increase the absorption efficiency is hard to overestimate considering the present-day applications.

It is well-known that the absorption is strongly affected by the plasma density gradient. This is especially essential for the short-pulse laser-matter interaction, when the pulse duration  $\tau_L$  may be so short that the plasma expansion is insignificant and, therefore, the bigger part of the laser pulse interacts with dense plasmas. On the other hand, for a low temporal contrast intense pulses, the situation becomes more complicated due to the target ionization at the leading front and finite scale length plasma forming by the time of peak intensity arrival. This happens due to the intensity pedestal in the laser pulse arising from the amplified spontaneous emission and/or relatively intense pre-pulses generated in the amplification chain. The influence of the laser pulse structure (shape) on the ionization and absorption is discussed in Section 2.1.5. To estimate the speed of the emerging plasma sheath

(ion ablation by the plasma pressure), a formula for the speed of the acoustic wave  $c_s$  (sound speed in plasmas) can be used as a good approximation:

$$c_s = \sqrt{\frac{Z^* k_B T_e}{M_i}} \approx 3.1 \times 10^7 \sqrt{T_e [\text{keV}] Z^* / A} \text{ [cm/s}^{-1}\text{]}. \quad (2.13)$$

Here,  $Z^*$  is the effective ion charge,  $T_e$  is the electron temperature,  $A$  is the atomic number,  $M_i$  is the ion mass. Now considering an isothermal expansion, we obtain an exponential decrease of the density with density scale length:

$$L \equiv n_e \left( \frac{dn_e}{dx} \right)^{-1} = c_s \tau_L. \quad (2.14)$$

Assuming a Ti foil heated up to 1 keV by a 45 fs-long frequency-doubled (400 nm) Ti:Sapphire laser pulse, a plasma with  $L/\lambda \approx 0.03$  is expected by the end of the pulse (for  $\text{Ti}^{12+}$  (Ne-like Ti)). A similar scale is expected for a heavier element - Zn target also ionized up to  $\text{Zn}^{20+}$  (Ne-like Zn).

One may expect the following scenario: long before the arrival of the main pulse (when the intensity is at the level  $< 10^{11} - 10^{12} \text{ W/cm}^2$ ) the absorption at the very steep plasma gradient is dominated by collisional absorption (inverse bremsstrahlung) and resonance absorption. Close to the peak of the laser pulse the other mechanisms overrule. For irradiances  $I\lambda^2 \geq 10^{15} \text{ Wcm}^{-2}\mu\text{m}^2$ , the plasma temperature rises sufficiently fast making collisions ineffective. Depending on the sharpness of the plasma gradient, the laser light polarization and the incidence angle, Brunel absorption (vacuum heating) or  $\vec{j} \times \vec{B}$  absorption may occur. Speaking of the absorption mechanisms, it is often referred to the corresponding heating mechanisms and the other way round.

## Inverse bremsstrahlung

At the low laser intensity levels, laser photon energy can be transferred to the plasma through the electron-ion collisions. The corresponding collisional mechanism called *inverse bremsstrahlung*. An electron oscillating in the laser field and colliding with ions, on average gains energy from the laser beam. This energy is then transferred to the other electrons and ions. Therefore, the laser beam is getting damped (*collisional damping*), and, as a consequence, the plasma heats up.

To calculate the absorption one can apply two approaches. The assumption of a perfect step-profile of plasma density ( $L \rightarrow 0$ ) allows using the Fresnel equations.

Alternatively, for an arbitrary profile, the Helmholtz wave equations for EM wave propagation in an inhomogeneous plasma can be solved [Kruer88]. The corresponding equation of motion contains a collision term defined by the *electron-ion collision frequency*:

$$\begin{aligned} \nu_{ei} &= \frac{4}{3} \frac{\sqrt{2\pi} e^4 Z n_e}{(k_B T_e)^{3/2} \sqrt{m}} \ln \Lambda \\ &\approx 2.91 \times 10^{-6} Z n_e [\text{cm}^{-3}] (T_e [\text{eV}])^{-3/2} \ln \Lambda [\text{s}^{-1}], \end{aligned} \quad (2.15)$$

where  $\ln \Lambda$  is the Coulomb logarithm accounting for the limits of the electron-ion scattering cross-section. The Coulomb logarithm is equal here to the ratio between the closest approach distance  $l_{min}$  and the Debye radius  $\lambda_D$ :  $\Lambda = \lambda_D / l_{min} = \lambda_D \cdot \frac{k_B T_e}{Z e^2}$ . It has been shown that for an exponential plasma profile the absorption coefficient yields [Kruer88]

$$\alpha_{abs} = 1 - \exp\left(-\frac{8}{3} \frac{\nu_{ei}(n_{cr})L}{c}\right). \quad (2.16)$$

The Eq. 2.16 implies that the absorption is high for the long-density-scale cold high-Z plasmas. Additionally, the absorption of the linearly polarized light reveals an angular dependence. For s-polarization and the incidence angle  $\theta$ ,  $\cos^3 \theta$  has to be plugged in Eq. 2.16 (in exponent). For p-polarization, the solution of the wave equation resembles a resonant behavior of the absorption, which will be discussed in the next subsection. Note, for a rising laser pulse intensity, when the quiver velocity  $v_{osc}$  becomes comparable to the thermal velocity  $v_{te}$ , a correction for an electron temperature  $T_e$  should be included in Eq. 2.15:  $T_{eff} \propto v_{osc}^2 + v_{te}^2$  [Wilks97].

## Resonance absorption

At non-relativistic laser intensities, there is another absorption mechanism present in a special case of a p-polarized light in an oblique incident geometry – *resonance absorption* (RA). Let us consider a plasma expanding in the z-direction and heated by the laser pulse at some non-zero incident angle  $\theta$  (measured with respect to the normal). The complex refractive index  $n(x)$  of plasmas in the collisional approximation is given by:

$$n^2(x) = 1 - \frac{\omega_p^2}{\omega_L^2(1 + i\nu_{ei}/\omega_L)}. \quad (2.17)$$

It can be shown that the light will be reflected at the density lower than a critical

density  $n_{cr}$ :  $n_{cr} \cos^2 \theta$ . For the p-polarized light, the electric field component  $\vec{E}$  is in the plane formed by  $\vec{k}$  and  $\nabla n_e$  (plane of incidence). Some amount of the laser energy can tunnel to the critical density surface. At the turning point,  $\vec{E}$  is parallel to  $\nabla n_e$  and an electron plasma wave will be excited at the resonant plasma frequency  $\omega_p = \omega_L$ . In the case of s-polarized light ( $\vec{E} \parallel \nabla n_e$ ), no plasma wave can be excited. The fraction of the energy transferred to the plasma wave depends on the scale length, the angle of incidence and the laser frequency. If the angle  $\theta$  is too small, the reflection point will be too far from the critical surface, thus the region to tunnel is too long. The damping of the oscillation amplitude here happens mostly due to the wave breaking (collisionless mechanism). The absorbed energy goes into a small fraction of electrons which get accelerated to high kinetic energies. It is found that the effective temperature of these suprathermal electrons forming a hot “tail” in the electron energy distribution function scales according to the *Beg’s law* [Beg97]:

$$T_{hot} \approx (I[10^{18}\text{W}/\text{cm}^2]\lambda^2[\mu\text{m}^2])^{1/3} [\text{MeV}] \quad (2.18)$$

The RA is stronger than the inverse bremsstrahlung absorption when the intensities are higher and the plasma scale length is short. Moreover, the steeped density profile loosens the dependency of RA on the incident angle. At higher intensities, effects such as rippling of the critical surface may increase the absorption providing additional regions where  $\vec{E} \cdot \nabla n_e \neq 0$ . In fact, this can trigger RA even for s-polarized light.

In reality, there are no sharp borders on the intensity range (or ponderomotive potential) defining the domain of applicability of the RA or inverse bremsstrahlung.

### **Brunel (vacuum heating)**

When the plasma gradient is high ( $L/\lambda \ll 1$ ), the resonant absorption cannot work in a classical way (no resonant wave possible). However, there is another mechanism of absorption in which the electric field of the incident laser pulse driving the electron oscillations across the density gradient – the “not-so resonant” *Brunel mechanism* [Brunel87]. In this case, the excursion of the electrons occurs so close to the plasma-vacuum interface, that the electrons can be literally pulled out into a vacuum. And when the field switches the sign, the electrons are pushed back into the overdense plasma region, where the energy will be eventually spread through collisions (Fig. 2.3(a)). This happens within a half laser cycle. It is important to

mention, that the absorption coefficient linearly scales with  $v_{osc}/c$ , and the larger incidence angles result in a higher absorption. In a pure step profile, vacuum heating is expected to be negligible compared to absorption via anomalous skin effect (see in the further subsections).

### $\vec{j} \times \vec{B}$ heating

Physically, relativistic  $\vec{j} \times \vec{B}$  heating is quite similar to the Brunel mechanism, in which the electrons are directly accelerated by the laser field at the steep plasma gradients. But the driving force (see Eq. 2.4) in this case is Lorentz force  $\vec{v} \times \vec{B}$ . Another difference is that  $\vec{j} \times \vec{B}$  mechanism works at any laser light polarization (apart from circular). Consequently, the absorption takes place even at normal incidence, when it can be considered as a form of vacuum heating but with high-frequency oscillations ( $2\omega_L$ ). It can be derived that the longitudinal force arising from  $\vec{j} \times \vec{B}$  mechanism is proportional to  $(1 - \cos(2\omega_L t))$ . The constant term here is simply the ponderomotive force, whereas the oscillation term is liable for acceleration of the electron bunches into the target. The electrons are accelerated in the direction of the laser pulse propagation and their energies are expected to scale with ponderomotive force of the laser pulse (Fig. 2.3(b)).

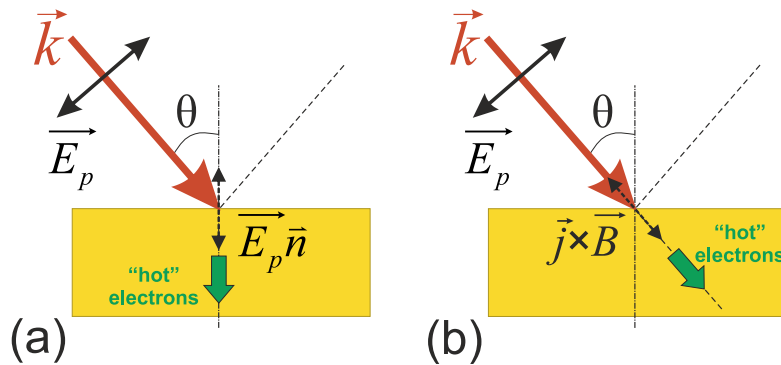


**Fig. 2.3:** Schematic of the heating mechanisms: (a) Brunel heating, (b)  $\vec{j} \times \vec{B}$  mechanism.

### Anomalous skin effect

Let us first consider the situation for the normal skin effect taking place for moderately low intensities ( $I_L \ll 10^{16}$  W/cm<sup>2</sup>). The electrons within the skin layer  $l_s \simeq c/\omega_p(v_{ei}/\omega_L)$ , defined by the generalized form of Eq. 2.12, oscillate in the laser field and lose their energy through the collisions. If we now assume that the plasma electron temperature increases (at higher laser irradiance) and the mean thermal



excursion length  $v_{te}/\omega_L > l_s$ , the physics of interaction changes. In the relativistic regime, the laser field can propagate deeper into overdense plasmas. Physically, this can be associated with the increase of the electron mass (relativistic mass) making it harder to generate a current causing the reflection of the laser light. The collision frequency should be replaced by the effective collision frequency defined by the excursion time in the *anomalous skin layer*  $l_{as}$ :  $\nu_{eff} = v_{te}/l_a$ . Using this correction we obtain the size of the anomalous skin layer:

$$l_{as} \simeq \left( \frac{c^2 v_{te}}{\omega_L \omega_p^2} \right)^{1/3}. \quad (2.19)$$

If the laser period is smaller than the electron transit time through the skin layer, i.e.,  $v_{te}/\omega_L l_s$ , the laser energy can be absorbed in the overdense plasma by another collisionless mechanism called *sheath inverse bremsstrahlung* [Catto77]. The electrons gain the energy from the laser field while being reflected at the plasma-vacuum interface (sheath) back into plasma.

## Morphology-dependent absorption

The reviewed mechanisms of the laser energy absorption were discussed in the framework of a flat surface target. However, considering a different target morphology, for example, nanowire arrays investigated in this thesis, we should extend our discourse. The main idea of using targets with a modified surface structure is to make the energy coupling into the short-living plasma efficient. It is especially important for the creation of hot and dense plasmas. Nanowire (NW) targets can help to overcome the limits set by the critical density  $n_{cr}$  as explained in Chapter 1. For irradiances  $I\lambda^2 \geq 10^{15} \text{ Wcm}^{-2}\mu\text{m}^2$  relevant to our experiments, high pulse contrast plays a decisive role and the collisionless mechanisms of absorption are dominant. Cylindrical NWs provide a significantly larger surface area than a polished target irradiated under the same conditions. A sharp plasma gradient enables a vacuum heating mechanism. If the radius of NWs is smaller or comparable with a skin depth, the laser field can interact with the whole volume of each irradiated NW. Electrons are pulled out of the NWs and accelerated in the gaps between the NWs by the laser field. Depending on the distance between the NWs and the gained energy, these electrons may travel far in the transverse direction colliding with the neighboring NWs, transferring their energy and causing inner-shell ionization. The plasma expansion proceeds mainly perpendicular to the laser propagation

direction, strikingly contrasting with the plasma dynamics of flat solids. Moreover, propagating deep along the NWs laser pulse is, so to speak, trapped in the structure of the target where it is effectively absorbed. A number of theoretical studies on ultra-intense laser-matter interaction with nanostructured targets investigating plasma heating mechanisms and predicting a significant enhancement of hard X-ray emission, strong electron and proton acceleration [Jiang14a; Jiang14b; Cristoforetti17; Luebcke17; Shukla17].

## 2.1.4 Heat transport in plasmas

In the previous sections, we discussed plasma formation and the laser energy absorption mechanisms implying that the laser pulse does not penetrate beyond the critical surface. That said, the energy carried by the laser beam is to be transported into the matter by radiation or by electron thermal conduction. Thus, the transport processes play an essential role in plasma heating. Experimental X-ray spectra contain information integrated over time and space. Therefore, understanding of the heat transfer in produced plasmas is crucial for the interpretation of the results. Besides the actual heat transfer, there are other important transport phenomena taking place in plasma, for instance, diffusion (particle flux), viscosity (momentum flux) and electrical conductivity (current density).

### Thermal conductivity

Plasmas tend to reach the equilibrium as every medium with a temperature gradient. This requires a heat flow from the regions with higher temperature to that with lower temperature. Assuming that the mean electron path is smaller than the temperature gradient (consistent with the Spitzer-Härm model [Spitzer53]), the heat flux, as the energy crossing a unit area per unit of time perpendicular to this area, can be defined by:

$$\vec{q} = -\kappa_e \nabla T_e. \quad (2.20)$$

For the *thermal conductivity* of electrons  $\kappa_e$  the *Spitzer expression* can be used:

$$\kappa_e = \frac{16\sqrt{2\pi}}{3} \frac{n_e v_{te}^2}{\nu_{ei}} = \frac{16\sqrt{2}}{\pi^{3/2}} \frac{(k_B T_e)^{5/2}}{Z e^4 m^{1/2} \ln \Lambda'}, \quad (2.21)$$

where the thermal speed  $v_{te} = (k_B T_e / m)^{1/2}$  and the collision frequency from Eq. 2.15. It depends non-linearly on electron temperature  $T_e$  and is very weakly (via

Coulomb logarithm) dependent on electron density  $n_e$ . From Eq. 2.21 it can be seen that  $\kappa_e$  is proportional to the characteristic collision time  $\tau_{ei} = 1/\nu_{ei}$ , pointing out the important limitation: in this model, only electron-ion collisions are taken into account. For small  $Z$ , the thermal conductivity needs to be corrected by including the influence of the electron-electron collisions. The energy transport can be written for the ideal plasma in the form:

$$\frac{3}{2}n_e \frac{\partial T_e}{\partial t} = -\nabla \cdot \vec{q} + \nabla \cdot \vec{\Phi}, \quad (2.22)$$

where  $\vec{\Phi}$  is the absorbed laser flux. To get an agreement between simulations and experiments and to include an arising inhibition of the thermal conductivity (due to magnetic fields and the pressure gradient), the expression for conductivity has to be modified. This results in the effective conductivity  $\kappa_{eff}$ , which is significantly smaller than the classical value. The heat flux in the so-called flux-limited transport model is given by [Drake06; Kruer88]:

$$|\vec{q}| = f n_e k_B T_e \nu_{te}. \quad (2.23)$$

The factor  $f$ , the flux limiter, varies between different simulation codes (0.03 - 0.1). Since the collision process plays a key role in the thermal conduction, it is feasible to estimate the effectiveness of the different collisions. Basically, the collision time defines the energy relaxation time  $\tau_E$ , i.e., time needed for a particle to transfer most of its kinetic energy to the collision partner. For different types of collisions, one can write [Eliezer02]:

$$\tau_E^{ee} \approx \tau_{ee} = \frac{3\sqrt{6}}{8} \frac{\sqrt{m}(k_B T_e)^{3/2}}{\pi e^4 n_e \ln \Lambda} - \text{electron-electron collision time}, \quad (2.24a)$$

$$\tau_E^{ii} \approx \frac{1}{Z^3} \left( \frac{M_i}{m} \right)^{1/2} \tau_E^{ee}, \quad (2.24b)$$

$$\tau_E^{ei} \approx \frac{1}{Z} \left( \frac{M_i}{m} \right) \tau_{ee}, \quad (2.24c)$$

$$\tau_E^{ie} \approx \left( \frac{M_i}{m} \right)^2 \tau_{ei}. \quad (2.24d)$$

The indices denote the particles, where the first one is the test particle which thermalizes/scatters on the second particle ( $i$  - ions,  $e$  - electrons). Substitution of the known constants into Eq. 2.24(d) yields the following order of magnitude estimate for the collision time:

$$\tau_{ee} \approx 1 \times 10^{-10} \frac{(T_e[\text{keV}])^{3/2}}{n_e[10^{20}\text{cm}^{-3}] \ln \Lambda} \text{ [s]}. \quad (2.25)$$

From the set of equations (Eq. 2.24), it is possible to conclude that the thermalization of electrons via interaction with the other electrons happens on a shorter time scale than with the ions. Also, the electrons reach an equilibrium distribution much earlier than the ions. For example, for a solid density plasma,  $n_e \approx 10^{23} \text{ cm}^{-3}$ , with an ion charge  $Z = 10$ , an electron temperature  $T_e = 1 \text{ keV}$ ,  $M_i/m \approx 4 \times 10^4$ ,  $\ln \Lambda \approx 10$ , the electrons will thermalize in about 10 fs, while the ion temperature will be equal to the electron temperature only  $\sim 40 \text{ ps}$  after the start of laser-matter interaction. For the ultra-short pulses, the plasma evolution happens on a much longer time scale than the interaction itself.

## Radiative transport

The self-emitted radiation may represent a significant contribution to the heat transfer in plasma, especially at high plasma densities and temperatures. The heat conduction is spreading much slower (with the sound speed). Therefore, in the regions which are not yet reached, the energy transport is always imposed by radiation independently of plasma parameters. From a phenomenological point of view, the *radiative transport* can be explained the following way. The hot plasma regions cool down by emitting strong radiation which is a predominant energy loss mechanism in these regions. This radiation is intensively absorbed in the neighboring zones, which initially have a lower temperature. How strong is the radiative flux, where and how effective it can be absorbed depends on the plasma composition and its parameters, e.g., temperature and density gradients, atomic number, degree of ionization.

The energy transport is described by a set of quantities. The radiation energy per frequency interval  $[\nu, \nu + d\nu]$ , crossing a unit area per unit time in the direction  $\Omega$ , within the solid angle  $d\Omega$  can be defined with the spectral radiation intensity  $I_{\nu}$ . The spectral energy density  $U_\nu$  and the spectral energy flux vector  $\vec{S}_\nu$  can be expressed as follows:

$$U_\nu(\vec{r}, t) = \frac{1}{c} \int I_\nu d\Omega, \quad (2.26)$$

$$\vec{S}_\nu(\vec{r}, t) = \int I_\nu \vec{\Omega} d\Omega. \quad (2.27)$$

Clearly, a proper description of the energy transport requires the knowledge of the

losses – absorption and scattering. To account for these processes, the frequency-dependent opacity of the material  $\kappa_\nu$  is introduced:

$$\kappa_\nu = \sum_j n_j \sigma_{\nu j}. \quad (2.28)$$

It shows how much energy per unit length propagation will be absorbed/scattered on particles of type  $j$  with the density  $n_j$ , due to the processes with the cross-sections  $\sigma_{\nu j}$ . The opacity effects strongly depend on the plasma parameters itself (through  $\sigma_{\nu j}$ ) and influence the emission spectra, as it will be shown in the chapters discussing the experimental results.

Finally, the radiation energy conservation of a frequency  $\nu$  in the local thermodynamic equilibrium (LTE)<sup>1</sup> can be described by the transport equation:

$$\frac{\partial U_\nu}{\partial t} + \nabla \cdot \vec{S}_\nu = c\kappa_\nu(U_{\nu p} - U_\nu), \quad (2.29)$$

where  $U_{\nu p}$  is the Planck spectral energy density of a blackbody radiator.

## 2.1.5 Laser pulse contrast

Owing to the advances in laser technologies, nowadays we can experimentally access the phenomena occurring at high field laser-matter interactions. The 2018 Nobel Prize in physics recognized revolutionary inventions in laser physics. One of them is the development of a technique for generating ultra-short intense laser pulses – chirped pulse amplification (CPA) by Gérard Mourou and Donna Strickland [Strickland85]. The solid-state lasers based on CPA generate femtosecond pulses approaching the single-cycle limit. These systems with multi-terawatt peak power, when properly focused, enable peak intensities of up to  $10^{22}$  W/cm<sup>2</sup>.

In reality, the laser pulse does not have an ideal Gaussian shape, meaning that the increase of the intensity of the laser pulse is inevitably accompanied by the growing intensity of the background light (Fig. 2.4). Quantitatively, the contrast of a laser pulse is the intensity ratio of the main pulse to its pedestal or pre-pulses. These background features are the consequences of the CPA technique. For example, pre-pulses (as well as post-pulses) in a CPA system can be generated from multiple reflections or from the light leaking through the pockels cells and amplified in one

---

<sup>1</sup>For more details see Section 2.2.2.

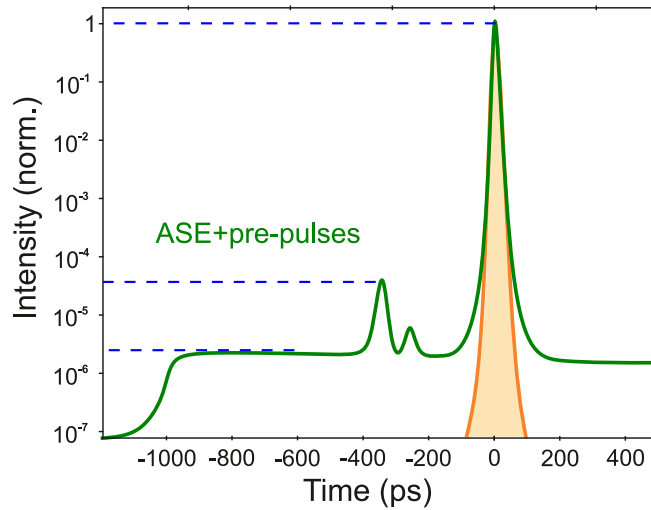


**Fig. 2.4:** Schematic illustration of the temporal structure of a typical (green line) and an ideal Gaussian (shaded orange area) pulses.

of the amplifier stages. An imperfect alignment of the compressor and other optical elements in the beam line may also result in an appearance of the unwanted pre- or post-pulses. While the pre-pulses can be found on a sub-picosecond as well as on a nanosecond scale, the intensity pedestal is present on a nanosecond time scale. It appears mainly due to the amplified spontaneous emission (ASE). Presence of this “parasitic” emission may completely change the regime of laser-matter interaction, thus widely discussed in the context of high power lasers [Keppler15; Bagnoud16]. Indeed, when the intensity level of ASE or a pre-pulse is high enough to create a low-density plasma on the target surface – pre-plasma, the main pulse will not interact with a steep density gradient. For example, the efficiency of high harmonic generation from solids will dramatically drop [Zepf98]. In plasma-based ion acceleration experiments, the shock waves driven by the pre-pulses may completely suppress the acceleration by TNSA (target normal sheath acceleration) mechanism [Roth14]. For the experiments discussed in this thesis, the pulse contrast is of particular importance, since the nanostructures on the target surface must stay intact until the main pulse will arrive. It is worth to mention, that the drawback of pre-plasma formation is rather ambiguous, while the optimized plasma scale  $L$  can enhance the X-ray emission from the flat solids [Zhidkov00; Ziener02] and increase the maximum proton energy [Batani10]. Indeed, it may support an efficient deposition of the laser energy into the target.

Let us consider the measured pulse contrast of the JETi-40 (Institute of Optics and Quantum Electronics, FSU Jena) – Ti:Sapphire system employed in the experiments

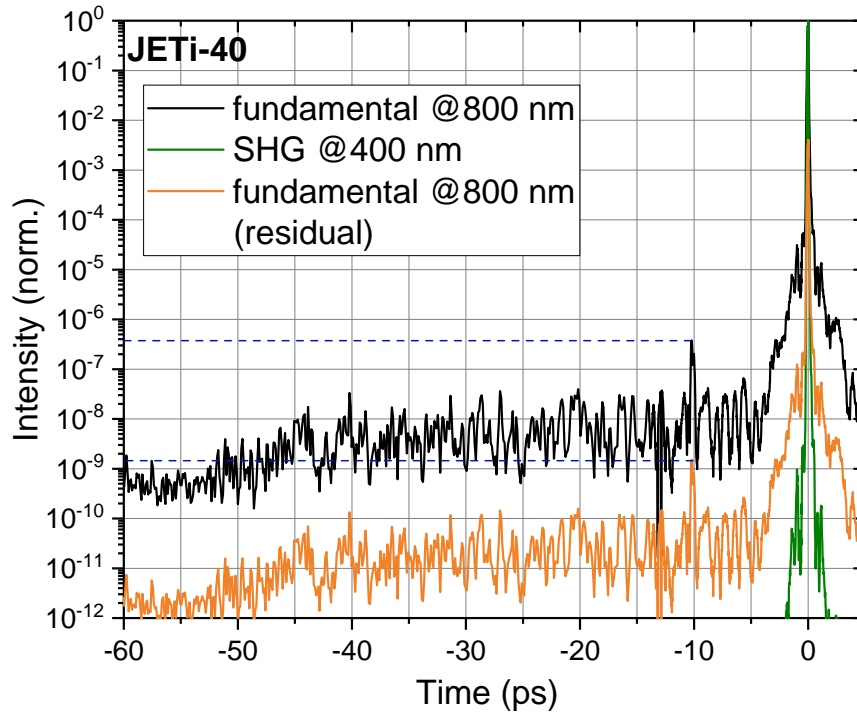


**Fig. 2.5:** JETi-40 laser pulse contrast. The measured third-order correlation trace of the fundamental laser pulse. The pulse contrast was calculated for the frequency-doubled laser pulse (SHG, 20% efficiency). The level of residual radiation at 800 nm (with two dichroic mirrors used) is shown. (Courtesy of Dr. Alexander Sävert.)

described in Chapter 4 (Fig. 2.5). The pulse characterization was carried out with a third order cross-correlator Sequoia (Amplitude Technologies). The initial pulse contrast was not sufficient for the measurements at relativistic intensities. The pre-pulse coming  $\sim 10$  ps before the main pulse is by a factor of  $10^6$  weaker than the main pulse, while ASE intensity is roughly  $10^7 - 10^9$  times weaker. In fact, assuming the peak intensities over  $10^{19}$  W/cm<sup>2</sup>, we would already start to ionize the target with ASE several tens of picosecond before the arrival of the peak intensity. Therefore, to improve the contrast, the laser pulse was frequency doubled by a 700  $\mu\text{m}$ -thick KDP crystal and cleaned up from the residual infrared pulse with several dichroic mirrors (HR@800 nm, AR@400 nm). The expected pulse structure for the 20% conversion efficiency of second harmonic generation (SHG) is given in Fig. 2.5. Using SHG and applying two dichroic mirrors improve the nanosecond contrast of  $10^{-11} - 10^{-12}$  and the contrast at 1 ps to  $10^{-7}$ . Note, a pair of dichroic mirrors reduces the residual radiation at 800 nm by a factor of 250. In different experimental campaigns, we used 2 or 3 dichroic mirrors and depending on the focusing conditions the intensity of the main pulse varied from  $10^{19}$  W/cm<sup>2</sup> to  $10^{20}$  W/cm<sup>2</sup>.

Surely, there are other methods to improve the pulse contrast based on non-linear effects. For example, employment of a plasma mirror helps to enhance the nanosecond contrast, however, it is not suited for the range of a few picoseconds and less before the main pulse [Roedel10; Scott15].

## 2.1.6 Methods of numerical simulations

Theoretical description of plasma is rather sophisticated, and to model the evolution of the parameters of laser-induced plasmas during and after interaction one can consider using numerical methods. Ideally, we would need to follow the trajectories of all plasma particles, similarly to a single-particle problem, and account for self-consistent electromagnetic fields and their dynamic change. This means a continuous update of the fields and particle trajectories within the simulations. Since the number of particles is tremendous, such a straightforward way would bring no results being computationally almost impossible. However, different approaches to the plasma description, like the hydrodynamic (HD) theory, the kinetic theory and the particle theory, enable efficient numerical simulations of short pulse laser interactions we are interested in. The HD (or fluid) simulations are widely used for the description of the plasma expansion/compression when the macroscopic plasma parameters are in focus. However, the assumption of a local thermodynamic equilibrium for physical quantities (e.g., temperature and pressure) strongly limits the applicability of HD codes. The kinetic theory is based on the Maxwell equations coupled to a set of the distribution functions of the particles, which form a set of kinetic equations called *Vlasov-Maxwell system of equations*. For a collisionless plasma, the single-particle distribution function  $f(\vec{r}, \vec{v}, t)$  is described by the *Vlasov equation* [Elliot93]:

$$\frac{\partial f}{\partial t} + \vec{v} \cdot \nabla_{\vec{r}} f + \frac{q}{m} \left( \vec{E} + \frac{\vec{v}}{c} \times \vec{B} \right) \cdot \nabla_{\vec{v}} f = 0, \quad (2.30)$$

where  $\vec{r}$  and  $\vec{v}$  are the coordinates in the phase space;  $q$  and  $m$  are the charge and the mass of the particle under consideration, respectively;  $\vec{E}$  and  $\vec{B}$  - the electromagnetic fields. If collisions are important, the Vlasov equation transforms into the Boltzmann equation by completing Eq. 2.30 with a collisional term  $\left( \frac{\partial f}{\partial t} \right)_{\text{col}}$  [Elliot93]. The phase space is 6-dimensional, what makes the full solution of the problem computationally rather expensive. In the Particle-in-Cell (PIC) codes using the particle theory, a plasma represents a finite number of discrete macro-particles,



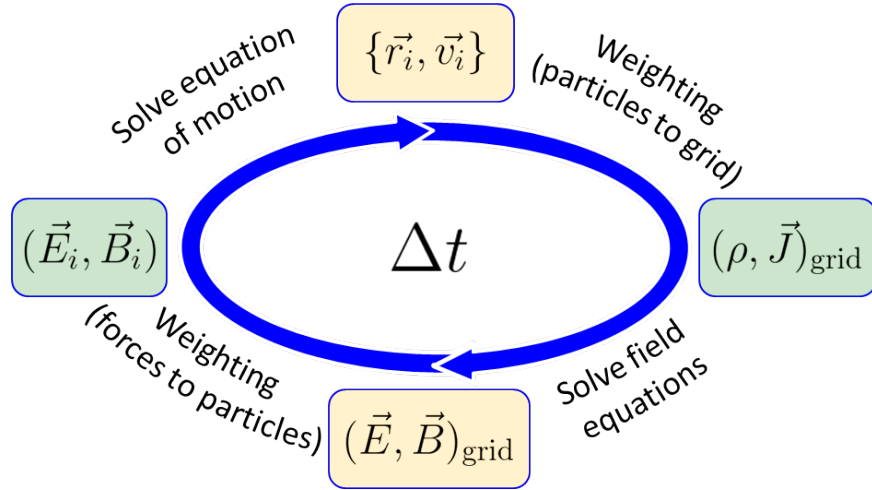


**Fig. 2.6:** The PIC computational cycle. The index  $i$  denotes a macro-particle.

which reduces the complexity of the task. The basic idea is very simple: calculate the motion of those particles in their self-consistent fields. Note that kinetic method and particle theory can be considered as different approaches to the same problem. We will briefly discuss the working principle of PIC codes. Rather than to solve the Vlasov-Maxwell system of equations in the continuous phase space, one can divide the volume into cells by parallel lines forming a mesh (or a grid). In the intersection points (nods) the fields can be calculated and all particle dynamics can be described with respect to these points. A primitive scheme of a computational cycle is presented in Fig. 2.6.

At the first step the initial coordinates  $\{\vec{r}_i, \vec{v}_i\}$  are defined from the equation of motion. Then the charge density  $\rho$  and the current density  $\vec{J}$  on a grid are computed. Next step is to integrate the Maxwell's equations and find the self-consistent electric and magnetic fields. After that, the influence of the fields in individual grid points is projected back to the particles, advancing the particles trajectories. Then the procedure is repeated for the next time step  $\Delta t$ , which should be chosen sufficiently small to resolve the highest frequency effects in the current problem (often the plasma frequency).

In this work we used the results from the three-dimensional electromagnetic relativistic PIC VLPL (Virtual Laser Plasma Lab) code [Pukhov99].

## 2.2 Atomic processes in plasmas

In this section, a short overview of the main atomic processes, governing the radiative and non-radiative transitions in hot plasmas, is given. The properties of electrons/ions in the ionized medium and the EM radiation produced in this medium are the subjects of studies in plasma spectroscopy. One of its sub-fields is X-ray spectroscopy, which we rely on in our experimental studies of the plasma parameters. We briefly present the main processes and discuss relevant parameters, such as probabilities and transition rates. Dealing with hot dense plasma it is feasible to use transitions in the few-electron ionic species (He- and H-like ions) for the analysis. The emission spectra hold information about the plasma parameters and its evolution. The dependency on plasma temperature and density, though, is rather complicated; however, it is still possible to use the measured line spectra for estimations. In order to simulate the experimental results presented in this thesis, we had to recourse to the collisional-radiative code FLYCHK, which is shortly introduced in the concluding subsection. Our discourse is based on [Salzmann98] and the lectures of Dr. Y. Ralchenko [Ralchenko15], Dr. H.-K. Chung [Chung15] and Dr. O. Rosmej [Rosmej17].

### 2.2.1 Basics: Types of processes

The X-ray emission is generated in laser-based plasmas due to the electron transitions. Depending on the type of the transition the emission processes can be attributed to one of three classes: *bound-bound* (b-b), *free-bound* (f-b), *free-free* (f-f).

*Bound-bound transitions* imply a transition of an electron between two discrete energy levels of the atomic system. Each atomic system has its unique structure (arrangement of the energy levels) determined by the interaction between the bound electrons and the nucleus. Therefore, the corresponding emission is in the form of a line with well-defined energy of emitted photons and called *characteristic*. The other two classes of the transitions are responsible for *bremstrahlung* emission.

When a free electron gets captured by an ion, it recombines with a hole in one of the shells and emits its excess energy. This is a *free-bound transition*.

The last class of atomic transitions involves a transition of a free electron through the continuum of free states accompanied by a change of the electron energy. Such a *free-free transition* is possible in the vicinity of other particles, usually ions.

Class	Process	Reaction	Inverse process
b-b	Spontaneous emission $\rightsquigarrow$	$X^{Z+*} \rightarrow X^{Z+} + \hbar\omega$	Photo excitation (resonant absorption)
b-b	Electron impact deexcitation (collisional)	$X^{Z+*} + e^-(E_1) \rightarrow X^{Z+} + e^-(E_2)$	Electron impact excitation
f-b	Radiative recombination (collisional) $\rightsquigarrow$	$X^{(Z+1)+} + e^- \rightarrow X^{Z+} + \hbar\omega$	Photoionization
f-b	Three-body recombination (collisional)	$X^{(Z+1)+} + 2e^- \rightarrow X^{Z+} + e^-$	Electron impact ionization (collisional)
f-b	Dielectronic recombination $\rightsquigarrow$	$X^{(Z+1)+} + e^- \rightarrow X^{Z+**}$ DR: $X^{Z+**} \rightarrow X^{Z+*} + \hbar\omega$ AI: $X^{Z+**} \rightarrow X^{(Z+1)+} + e^-$	Autoionization
f-f	Bremsstrahlung $\rightsquigarrow$	$X^{Z+} + e^{-*} \rightarrow X^{Z+} + e^- + \hbar\omega$	Inverse Bremsstrahlung

**Tab. 2.1:** Important atomic processes in plasma relevant to laser-matter interaction.  $\rightsquigarrow$  indicates radiative processes.  $X^{Z+}$  denotes an ion of type X with charge Z. The symbol \* indicates an excited state.  $E_{1,2}$  - kinetic energy.

The challenge of plasma spectroscopy is to identify which processes are important for a given plasma. In Table 2.1 we present the most important atomic processes in hot dense plasmas. According to the detailed balance<sup>1</sup>, under conditions of thermodynamic equilibrium, each reaction is balanced by its inverse reaction. There are surely much more processes in hot plasma, in particular, many-body processes. However, we concentrate on the ones given in Table 2.1, since they are dominant in the laboratory plasma we study.

## Spontaneous emission

If the energy of the incident electron  $E_{kin}$  is greater than the binding energy  $E_j$  (also called ionization potential  $I_p$ , see Section 2.1.1), it can kick out an electron in the inner shell from a low energy level  $j$ . This vacancy is then filled with another electron transiting from an upper energy level  $i$ . Then for the optically thin plasma

<sup>1</sup>The detailed balance principle states that the ratio of the transition rates of two contrary processes (direct and inverse) is proportional to the ratio of the final state densities of the two processes only and not on any other parameter of interaction [Salzmann98].

(no opacity effects included) the intensity of the corresponding line integrated over the depth of plasma  $s$  is given by:

$$I_{ij} = \frac{1}{4\pi} \int N_i A_{ij} \hbar \omega_{ij} ds, \quad (2.31)$$

where  $N_i$  is the population of the upper (initial) energy level  $i$ , strongly dependent on the plasma conditions, and  $A_{ij}$  is the spontaneous transition probability or *Einstein coefficient* – (almost) purely atomic parameter. Transition probabilities are often expressed via the *oscillator strength*  $f_{ij}$ . It satisfies the following equation:

$$f_{ji} \approx 2.1 \times 10^{-8} \frac{g_i}{g_j} \frac{1}{\Delta E_{ij}} A_{ij}, \quad (2.32)$$

where  $g_i$  and  $g_j$  are multiplicities (degenerations) of levels  $i$  and  $j$ .

When the plasma is cold and weakly-ionized, the hot electrons generated within the laser pulse may cause a strong, so-called "cold" K-shell emission. When the plasma heats up and the ionization degree grows, the nature of the line emission gets more sophisticated.

In plasma, the transition probability and even the energy of a transition  $\Delta E_{ij}$  are strongly influenced not only by the Coulomb interaction between ions but also by the electric potential of the collective plasma dynamics. The radiative transitions include electric dipole, magnetic dipole and electric quadrupole transitions. The electric dipole transitions are optically allowed (*selection rules*) and have the highest probabilities, while the other two types are forbidden transitions whose oscillation strength is much weaker and strongly depends on the ion charge  $Z$ .

## Radiative recombination

This highly exothermic non-resonant process is a one-step process in which an electron is captured by an ion realizing excess energy as a photon (Fig. 2.7(a)). It has its largest influence in low-density plasmas. The *radiative recombination* (RR) cross-section for a free electron interacting with a bare nucleus into H-like ions was derived in [Kramers23]:

$$\sigma_{RR} = 2.105 \times 10^{-22} \frac{Ry^2 Z^4}{n E_{kin} (n^2 E_{kin} + Ry Z^2)} [\text{cm}^2], \quad (2.33)$$

where  $Ry$  is the Rydberg constant in eV ( $\approx 13.606$  eV),  $n$  denotes here the principal

quantum number of the recombined electron with kinetic energy  $E_{kin}$ . This formula predicts that the RR goes preferentially into the lowest states (smaller  $n$ ) and needs correction by a Gaunt factor  $G_n^1$  [Gaunt30]. Eq. 2.33 can be used also for other ionic species, but the ion charge  $Z$  should be replaced with an effective  $Z_{eff}$  charge. For all the collisional processes, a rate  $R$  for a given electron energy distribution  $f(E)$  (typically, the Maxwellian) can be introduced<sup>2</sup>:

$$R [\text{s}^{-1}] = n_e \int_{E_{min}}^{E_{max}} \sigma(E) v f(E) dE = n_e \langle v \sigma \rangle. \quad (2.34)$$

Modifying Eq. 2.33 we get an expression for the rate coefficient of RR [Lotz67b]:

$$\langle v \sigma \rangle_{RR} = 5 \times 10^{-14} \frac{n^2 (E_n [\text{eV}])^{3/2}}{z^2 R y \sqrt{T_e [\text{eV}]} } x_n e^{x_n} E_1(x_n) q_n \left[ \frac{\text{cm}^3}{\text{s}} \right] \quad (2.35)$$

where  $x_n = E_n / T_e$ ,  $E_n$  is the ionization energy of level  $n$ ,  $q_n$  is a factor accounting for equivalent electrons,  $E_1(x_n)$  is the exponential integral of the first order<sup>3</sup>.

## Electron impact excitation/deexcitation

A free electron moving near an ion of charge  $Z$  may lose its energy by inducing a transition of a bound electron from a low (ground or excited) energy state  $n$  to a higher (excited) state  $m$ . In fact, the excitation is possible for outer-shell and inner-shell electrons, and also can involve two electrons – resonant excitation. In the latter process, a free electron is captured by an ion while exciting a bound electron producing an intermediate doubly excited state  $X^{Z+**}$  (*dielectronic capture* (DC)). During the *collisional deexcitation* (CDE) a free electron takes away the extra energy causing a downward transition of the ionic state (Fig. 2.7(b)). The processes do not change the ion charge, but only its state of excitation. The widely used empirical formula for the rate coefficient for the electron impact excitation was proposed by Van Regemorter [Regemorter62] for electric dipole transitions:

<sup>1</sup>The Gaunt factor  $G_n$  takes into account medium effects and quantum corrections and is associated with the principal quantum number  $n$  for a free-bound transition. Generally, it is  $\sim 1$  for atoms and  $\sim 0.2$  for ions.

<sup>2</sup>Note that for the processes involving more particles (like three-body recombination) the rate  $R$  depends on  $n_e^2$  and the equation has to be modified accordingly.

<sup>3</sup> $E_1(x_n) = \int_1^\infty \frac{e^{-ux_n}}{u} du$ .

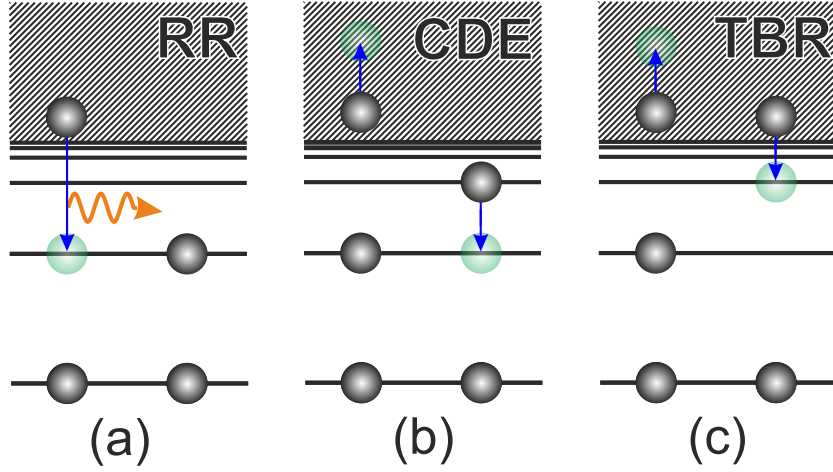


**Fig. 2.7:** Schematic diagram of (a) radiative recombination, (b) electron impact (or collisional) deexcitation and (c) three-body recombination.

$$\langle v\sigma \rangle_{CE} = 3 \times 10^{-6} f_{nm} \frac{e^{-x_{nm}}}{x_{nm} (T_e [\text{eV}])^{3/2}} \left[ \frac{\text{cm}^3}{\text{s}} \right], \quad (2.36)$$

where  $x_{nm} = E_{nm}/T_e$ . For the intercombination transitions (spin change  $\Delta S = 1$ ) one may use the following expression [Mewe72]:

$$\langle v\sigma \rangle_{CE}^{\text{inter}} = 1.6 \times 10^{-6} f_{nm} \frac{1 - x_{nm} [\ln(1 + 1/x_{nm}) - 0.4(1 + x_{nm})^2]}{(T_e [\text{eV}])^{3/2}} \left[ \frac{\text{cm}^3}{\text{s}} \right]. \quad (2.37)$$

The rate coefficient for the electron deexcitation process is connected to its inverse process through the detailed balance principle (Boltzmann relation):

$$\langle v\sigma \rangle_{CDE} = \langle v\sigma \rangle_{CE} \frac{g_n^z}{g_m^z} \exp(-x_{nm}) \left[ \frac{\text{cm}^3}{\text{s}} \right]. \quad (2.38)$$

The rate coefficient for the electron impact excitation  $\langle v\sigma \rangle_{CE}$  is rather low when the electron temperature  $T_e$  is much lower than the transition energy  $E_{nm}$ . When  $T_e$  approaches  $E_{nm}$ ,  $\langle v\sigma \rangle_{CE}$  rapidly rises and reaches its maximum. For the further increase of  $T_e$  it slowly drops. It is noteworthy that at higher temperatures ( $T_e$  several times higher than  $E_{nm}$ ) the probability to excite an electron into a discrete state becomes smaller than to ionize it into the continuum.

## Electron impact ionization

Electron impact ionization along with photo-ionization was discussed earlier in Section 2.1.1. Here we are interested in the rate coefficient for the ionizing shell  $nl$  with  $k$  electrons, which in accordance to the Lotz's formula (Eq. 2.2) is given by:

$$\langle v\sigma \rangle_{CI} = 3.14 \times 10^{-6} k \frac{E_1(x_{nm})}{x_{nm}(T_e[\text{eV}])^{3/2}} \left[ \frac{\text{cm}^3}{\text{s}} \right], \quad (2.39)$$

where  $x_{nm} = \Delta E_{nm}/T_e$ ,  $\Delta E_{nm}$  the energy difference between the level  $n$  in the ion with charge  $Z$  and level  $m$  in the ion with charge  $(Z + 1)$ . This formula gives reasonably accurate results and, therefore, is widely used.

### Three-body recombination

When two free electrons are in close vicinity of an ion at the same time, one of them can be captured and the other one carries away the extra energy (Fig. 2.7(c)). Clearly, such *three-body recombination* (TBR) is of great importance for a high-density plasma as well as its inverse process. Knowing the collisional rate coefficient for the ionization (Eq. 2.39), it is easy to find the rate coefficient for TBR using the detailed balance principle:

$$\langle v\sigma \rangle_{TBR} = \langle v\sigma \rangle_{CI} \cdot \frac{1}{n_e S} = \langle v\sigma \rangle_{CI} \frac{g_n^Z}{g_m^{Z+1}} \frac{\exp(\Delta E_{nm}[\text{eV}]/T_e[\text{eV}])}{6 \times 10^{21} (T_e[\text{eV}])^{3/2}} \left[ \frac{\text{cm}^3}{\text{s}} \right], \quad (2.40)$$

where  $S$  is the so-called *Saha factor*,  $g_n^Z$  and  $g_m^{Z+1}$  are the multiplicities of level  $n$  in the ion with charge  $Z$  and of level  $m$  in the ion with charge  $(Z + 1)$ , respectively. Virtually  $n$  and  $m$  denote the states of excitation before and after the interaction. In contrast to RR when ions recombine primarily into the ground state, TBR happens likely to the excited states.

### Dielectronic recombination and autoionization

As it is shown in Table 2.1, *dielectronic recombination* (DR) is a two-step process. First, a free electron with energy  $E_{\text{kin}}$  is captured by an ion inducing excitation of a bound electron and forming an intermediate doubly excited state – dielectronic capture (DC) (Fig. 2.8(a)). This step is possible only if:  $E_{\text{kin}} + I_p = E_m - E_0 \pm \delta E_m$ , where  $I_p$  is the binding energy for the recombined state,  $E_m - E_0$  is the energy of the doubly excited state above the ground state,  $\delta E_m$  is the width of the excited state. This illustrates the resonant nature of DR and *autoionization*<sup>1</sup> (AI). Then, the doubly excited state has two possible channels of decay: by radiative decay of one of the excited electrons (Fig. 2.8(b)) or by autoionization (Fig. 2.8(c)). That is why

<sup>1</sup>Autoionization is often associated with *Auger effect*. Indeed, both processes are caused by inter-electronic interactions. However, in the case of Auger decay of an inner-shell hole, a high-energy electron is emitted, whereas during autoionization a low-energy valence electron is ejected.

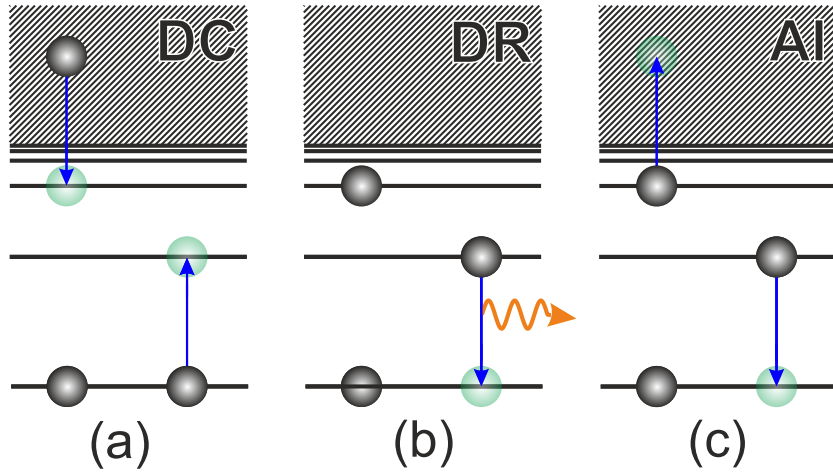


**Fig. 2.8:** Schematic diagram of (a) dielectronic capture, (b) dielectronic recombination (Li-like dielectronic satellite) and (c) autoionization.)

autoionization is a competing non-radiative process, rather than an inverse process for DR.

In most of the situations, the radiative decay goes to the lower possible state because of a larger oscillator strength. The rate coefficient for DR can be calculated using the Burgess formula [Burgess65]:

$$\langle v\sigma \rangle_{DR} = 10^{-13} B_d \beta^{3/2} e^{-\beta\chi_d} \left[ \frac{\text{cm}^3}{\text{s}} \right], \quad (2.41)$$

where

$$\begin{aligned} B_d &= 480 f_{m0} \left( \frac{Z\chi}{Z^2 + 13.4} \right)^{1/2} \\ &\times [1 + 0.105 \times (Z + 1)\chi + 0.015 \times (Z + 1)^2 \chi^2]^{-1}, \\ \beta &= \frac{(Z + 1)^2 R_y}{T_e}, \\ \chi_d &= \chi \left[ 1 + 0.015 \frac{Z^3}{(1 + Z)^2} \right]^{-1}, \\ \chi &= \frac{E_m - E_0}{(Z + 1)R_y}. \end{aligned} \quad (2.42)$$

Though there is no widely accepted formula for  $\langle v\sigma \rangle_{DR}$ , Eq. 2.41 gives a good approximation for the radiative transitions with  $\Delta n = 0$ .

It is important to mention that the radiative transition happens in an electric potential which is slightly different from the potential, which ion has without the captured electron (spectator electron). Therefore, the energy of the emitted photon is slightly different from the expected value for the corresponding transition in the



ion with charge  $(Z + 1)$ . For example, the energy of the line emission appearing as a result of recombination of the doubly excited Li-like ions, such as  $1s^22l - 1s^22l2l'$  ( $l, l' = s, p$ ), is very close but does not exactly match the corresponding He $_{\alpha}$  lines ( $1s^2 - 1s^22p$ ). Consequently, there is a set of lines to be observed red-shifted to the parent line He $_{\alpha}$ , called Li-like dielectronic satellites. Similarly, a set of He-like *dielectronic satellites* ( $1s2l - 2l2l'$ ) can be seen next to Ly $_{\alpha}$  lines. Actually, there are even more lines corresponding to the different upper levels on which the spectator electron could be captured. The intensity of the dielectronic satellites can be rather high and they can be easily seen in the experimental X-ray spectra with a high resolution (see Chapters 4-5).

DR is rather common in hot low-density plasmas. When the plasma electron density is high, the continuum lowering washes out the highly excited ionic levels limiting the possibility for DC.

### Bremsstrahlung and inverse bremsstrahlung

Classically, a moving charge can lose or gain energy if it is retarded or accelerated. In *bremsstrahlung*, a photon is emitted in the scattering (deacceleration) of an electron from an ion whose internal state remains the same. Assuming a plasma in thermal equilibrium with electrons having Maxwell-Boltzmann velocity distribution, we can obtain the emitted power per unit volume per unit frequency [W/(m<sup>3</sup>Hz)]:

$$\epsilon_{\nu}^{ff} = 6.8 \times 10^{-52} T_e^{-1/2} Z^2 n_e n_i \exp\left(-\frac{h\nu}{k_B T_e}\right) G_{ff}(\nu), \quad (2.43)$$

where  $G_{ff}(\nu)$  is the Gaunt factor, which in practically interesting cases is close to unity;  $n_e$  and  $n_i$  are the electron and ion densities;  $\nu$  is the emission frequency. In the inverse process, the bremsstrahlung emission gets absorbed by the electrons on the way out of the volume. This absorption is particularly decisive at low energies (few eV), while for very high energies (few tens of keV and above) Compton effect plays a major role. The absorption coefficient [m<sup>-1</sup>] for the free-free emission can be calculated by using *Kirchoff's law*:

$$\alpha_{\nu}^{ff} = 3.7 \times 10^{-2} T_e^{-1/2} \nu^{-3} Z^2 n_e n_i \left[1 - \exp\left(-\frac{h\nu}{k_B T_e}\right)\right] G_{ff}(\nu). \quad (2.44)$$

Eq. 2.43 indicates the thermal bremsstrahlung. But the real continuum emission from laser-produced plasma has a significantly more complicated time-dependent

structure and its simulation requires an appropriate velocity distribution [Batani02]. This problem is concisely discussed in reference to the experimental results in Chapter 3.

### Other atomic effects in hot dense plasmas

The plasma environment strongly modifies the electrostatic potential which influences the atomic processes. It can be mathematically shown that the binding energies can be strongly reduced in a dense plasma. The upper bound states can be even shifted into the continuum and vanish. This phenomenon is called *pressure ionization* or *continuum lowering* [More82; Salzmann98]. For example, at solid density plasmas ( $10^{23} - 10^{24} \text{ cm}^{-3}$ ) one can already expect that M-shell states of He-/H-like ions disappear in the continuum.

Another effect that can be observed is a shift of the characteristic lines, known also as *polarization shift*. However, this shift is extremely sensitive to the plasma conditions and quite small to be easily measured in an experiment.

Besides the shift, the emission lines also broaden as the electron density grows. When the ion is isolated and completely shielded from any external EM fields, the line width of the emission is determined by the lifetime  $\tau_{ij}$  of the excited state  $i$  (and also the lifetime of the low state  $j$ , if it is not a ground state):

$$\tau_{ij} = A_{ij}. \quad (2.45)$$

The thermal motion of the radiating ions with respect to the laboratory frame causes additional broadening of the spectral lines, called *Doppler broadening*. It depends on the plasma temperature only: the higher the temperature, the broader the line is. However, the relative impact of this broadening is rather small.

The interaction of the emitting ions with the electrons also influences the line width via so-called *electron impact broadening*. When the collision time is much shorter than the natural lifetime of the level, the individual radiator experiences disturbances and, thus, an instantaneous shift of the wavelength.

The origin of *quasi-static Stark broadening* resides in the slowly changing electric fields generated by the nearby particles. These fields strongly perturb the energy levels of the radiator and split its energy levels. This is the case when the interaction time is longer than the time between collisions. For the high electron densities, the line width is mainly defined by Stark broadening. The effect has a rather complicated

nature and its behavior depends on the strength of the electrostatic fields. An increase of electron density leads to complex non-linear behavior. The measurement of the Stark broadening of the emission lines is a very powerful spectroscopic method for the determination of the electron density  $n_e$ . In this thesis, we apply this tool for the line shapes of highly excited (Rydberg) ions, using an analytical model developed and implemented in an interactive tool "Plasma Formulary Interactive" [Stambulchik11].

One of the most important effects to be considered is *plasma opacity*. The generated X-ray emission can be trapped within the volume, significantly changing the measured line spectrum expected for the certain plasma parameters. Physically, the emission produced by an ion in plasmas can be absorbed and re-emitted by the neighbors. Therefore, the radiation can be lost on the way out of the volume. The merit of this effect is the *optical depth* of the plasma  $\tau$ . It is defined by  $\tau = \kappa_\nu l$ , where  $l$  is the path length for the emission and  $\kappa_\nu$  is the opacity. When  $\tau > 1$ , the plasma is called optically thick - strongly absorbing for the particular transition; when  $\tau \ll 1$  - the plasma is optically thin and the opacity effect is negligibly small.  $\kappa_\nu$  depends on the transition and local plasma density (see Eq. 2.28). In high-density plasmas, the effect is especially pronounced and causing additional line broadening (related to the transport of the emission from the radiation region). The ratios of the line intensities of few-electron ionic species are often used to estimate the plasma parameters (see Appendix A). In this case, it is necessary to take into account the plasma opacity to avoid a huge error. Normally, the simulations, with no opacity included, underestimate the plasma electron density.

## 2.2.2 Elements of population kinetics. FLYCHK code

In order to understand and simulate the characteristic X-ray emission, one requires the knowledge not solely about the plasma parameters but also the evolution of the charge states. When the rate of the ionization processes in plasma is larger than the rate of the recombination processes, the ion charge is continuously growing. The plasma is then termed *ionizing*. Otherwise, it is a *recombining* plasma. And only when the rates are equal, a steady state is attained. A plasma is considered to be in *thermodynamic equilibrium* (TE) if the following conditions are fulfilled:

- the energy distributions follow a Maxwell-Boltzmann distribution;
- the distribution of the excited states is of Boltzmann type;

- the distribution of the ionized states is given by Saha distribution:

$$\frac{N_{z+1}}{N_z} = 2 \left( \frac{mT_e}{2\pi\hbar^2} \right)^{3/2} \frac{g_{z+1} \exp(-I_p/T_e)}{g_z n_e}; \quad (2.46)$$

- the radiation has a Plank energy distribution function.

In a real plasma, the radiation may easily escape from the plasma volume, so that the photons are not necessarily in equilibrium. If the equilibrium holds in a local sense, the plasma is in local thermodynamic equilibrium (LTE). In LTE conditions according to the detailed balance, the rates of direct and inverse processes are connected via the Boltzmann and Saha factors for processes without and with a change of an ion charge, respectively. We already used these factors to obtain the rate coefficients for electron impact excitation (Eq. 2.37) and for three-body recombination (Eq. 2.40). Note that LTE is valid only when the collisions prevail over the radiation processes.

The LTE Saha equation (Eq. 2.46) does not work for all plasma parameters, since for  $n_e \rightarrow 0$ :  $N_{z+1}/N_z \rightarrow \infty$ . It can be shown that LTE can be applied only when the recombination processes are dominated by TBR. The validity condition can be expressed in the form

$$n_e > 1 \times 10^{14} (I_p[\text{eV}])^{5/2} (T_e[\text{eV}])^{1/2} [\text{cm}^{-3}]. \quad (2.47)$$

Another condition ensuring a Boltzmann distribution for the excited states [Griem63] has to be satisfied too:

$$n_e > 1.4 \times 10^{14} (\Delta E_{01}[\text{eV}])^3 (T_e[\text{eV}])^{1/2} [\text{cm}^{-3}], \quad (2.48)$$

where  $\Delta E_{01}$  is the energy of the first excited state above the ground state. For example, He-like Si plasma at  $T_e$  of several hundred eV should have  $n_e > 10^{25} \text{ cm}^{-3}$  what is higher than the solid density.

At low densities, TBR can be neglected. For such a plasma, the ratio  $N_{z+1}/N_z$  is independent of electron density  $n_e$  and the recombination is defined by radiative and dielectronic recombination rates. This regime in steady-state conditions is called *corona equilibrium* (CE). The charge state distribution in coronal plasma depends on the electron temperature  $T_e$ . However, in the intermediate electron density region, a simple two-level approach, as in CE and LTE-Saha models, is not valid. The

ionization from the excited states should be included – a corresponding model is known as *collisional-radiative (CR) model*. It is significantly more complicated than its low- and high-density limit models and requires a complete set of atomic data. The population distribution in CR is governed by the rate equations for the given plasma temperature and density.

A set of coupled basic rate equations can be written in the following form:

$$\frac{d\hat{N}(t)}{dt} = \hat{A}(t, \hat{N}(t), n_e, T_e, T_i, \dots) \cdot \hat{S}(t), \quad (2.49)$$

where  $\hat{N}(t)$  is the vector of populations for all atomic states involved,  $\hat{A}(t)$  is the rate matrix including the rates of all processes between the levels (off-diagonal elements) and the depopulation rates for a level (diagonal elements),  $\hat{S}(t)$  is the source function if present. For a rapidly evolving plasma, especially relativistic laser-induced plasma, the time-dependence included in Eq. 2.49 is essential.

The tool of our choice assisting spectral analysis is a collisional-radiative code FLYCHK, which includes a large atomic base and solves the rate equation considering the atomic processes [Chung05]. The code is rather flexible and can perform calculations for coronal, LTE or CR plasmas in a steady-state or in transient cases. It is worth mentioning that it accounts for such plasma effects as radiation transport (opacity) and line broadening (Doppler and Stark) in plasmas. It is a compact, comparably simple code allowing to perform quick simulations of laboratory plasmas with reasonable accuracy. However, the code is not suitable for low-temperature and weakly ionized plasmas. With the help of FLYCHK it is possible to synthesize the time-dependent emission spectra. In a transient case, which is of interest for the simulations of ultra-short laser-plasma interaction, the history of plasma parameter evolution ( $n_e, n_i, T_e$ , etc.) has to be provided as input data.

# Non-relativistic proof-of-principle experiment

To conduct a self-consistent study of the laser-matter interaction with nanowire targets it seems rather logical to start with an investigation of the non-relativistic regime. In this Chapter, we present our first experiment examining hard X-ray emission from ZnO solid targets generated by a moderate-energy laser. The target morphology and laser field polarization strongly influence the flux of bremsstrahlung and characteristic emission. In this proof-of-principle experiment, we explore the potential of nanowire targets for the efficient generation of hard X-rays with a laser pulse at intensities below  $10^{17}$  W/cm<sup>2</sup>.

Section 3.1 gives a brief overview of the compact high-repetition-rate laser-induced plasma sources and type of emission they can produce. The pilot experiment dedicated to the generation of X-ray emission with nanowire targets was carried out in the laboratory of the group of Prof. Förster (XRO, IOQ, FSU Jena). The description of the experimental setup and used targets are outlined in Section 3.2. We present the results of our measurements and discuss the observed tendencies in Section 3.3. The chapter is wrapped up with a summary of the experimental results and possible implications in Section 3.4.

Parts of this chapter have been published in [Samsonova18].

## 3.1 Towards compact plasma-based hard X-ray sources

Owing to the intensified research on laser-solid interaction, nowadays plasma-based ultrafast X-ray sources are of great importance for many intriguing applications. Their relatively compact size and accessibility justify the scientific interest, which covers well-defined line and continuous spectral emission. The various regimes of interaction define the parameters of the generated plasmas and, thus, the properties

of the produced emission. At relativistic intensities ( $I\lambda^2 > 1.3 \times 10^{18} \text{ W}\mu\text{m}^2/\text{cm}^2$ ), the laser pulse can strongly ionize solid/liquid targets and accelerate electrons beyond 1 MeV [Umstadter03]. Furthermore, plasmas produced within this interaction act as bright sources for X-rays and particles (electrons, protons, neutrons). The corresponding experiments are typically carried out at powerful laser systems with sub-picosecond and nowadays femtosecond pulse duration in a single-shot regime (for instance, [Beg97; Cowan00; Schwoerer01; Park06; Fourmaux16]). That type of interaction is discussed in Chapter 4. However, in order to increase the attraction and accessibility for users, who are mainly interested in a bright source of pulsed X-rays, the driving laser should be as simple as possible such a kHz, multi-mJ femtosecond laser system. Though in this case the laser-matter interaction is non-relativistic and the available laser pulse energy is significantly reduced, mJ-level laser systems are successfully used as drivers for X-ray sources [Hagedorn03; Zamponi09; Silies09; Holtz17]. Such table-top sources with high brilliance are proved to be a powerful tool, e. g. for time-resolved X-ray diffraction [Hoefler16]. Depending on the application, either a narrow-line emission at a certain wavelength or a broad-band emission is required. For the cold K-shell emission, there is no need to produce hot and dense plasmas since the characteristic emission arises from cold material bombarded by fast electrons. Therefore, a non-relativistic interaction is the most suitable and effective way to generate, for example, a strong  $K_\alpha$  yield. Bremsstrahlung emission, in this case, is often considered as a background which has to be suppressed. Therefore, insignificant attention has been paid for the investigation of possibilities to effectively generate X-ray photons over 20 keV at a high repetition rate. Nevertheless, hard X-ray continuous emission has also been made use of. In high energy density experiments, like inertial confinement fusion, bremsstrahlung sources are widely used as a "back-lighter" in inverse-bremsstrahlung absorption for time-resolved measurements of electron density [Park08; Remington15]. Meanwhile, softer bremsstrahlung emission is sufficient for X-ray absorption near-edge spectroscopy (XANES) and extended X-ray absorption fine-structure spectroscopy (EXAFS) [Benesch04; Fullagar07].

One of the methods to enhance the yield of the generated X-rays is related to the target geometry. A positive influence of the surface roughness, nanoparticle coating and, later on, specially synthesized nanostructures has been strongly emphasized in the early experimental studies [Kulsar00; Rajeev02; Rajeev03]. It has been shown theoretically that nanoscale structures optimized for the current laser parameters

can significantly increase the absorption of the laser energy [Andreev13; Purvis13]. Consequently, this leads to a more efficient generation of hot electrons and, thus, X-ray photons. Smartly developed nanostructured targets tend to be quite beneficial also for the high-repetition hard X-ray production. Detailed study of the effect of Si nanostructured targets on the X-ray yield as well as the influence of the pre-plasma formation and laser pulse polarization were reported in [Cristoforetti14]. However, this investigation was performed for significantly high pulse energies and does not engage with X-ray energies above 25 keV. In this chapter, we present our first experiments dedicated to the investigation of the potential of dielectric (zinc oxide) nanostructured targets to generate hard X-rays being irradiated by a moderate energy ultra-short laser pulse.

## 3.2 Experimental setup

This pilot experiment was performed with targets made of zinc oxide. Rather simple techniques of the growth make the production of ZnO nanostructures inexpensive. The details on the synthesis methods used for our samples are given in Appendix B. We used two types of nanowire (NW) morphology. The first type, which we shall refer to as 'vertically oriented NW' sample, represents an array of standing NWs perpendicular to the substrate surface (Fig. 3.1(a)). The second type (hereafter 'randomly oriented NW' sample), consists of a batch of NWs chaotically arranged along the sample surface (Fig. 3.1(b)). The substrate used for both of the types is a 500  $\mu\text{m}$ -thick Si wafer. The diameter and the length of the NWs having a diameter of 100 - 200 nm are typically 5  $\mu\text{m}$  and 15  $\mu\text{m}$  long in the case of vertically oriented and randomly oriented arrays, respectively. For the reference, all measurements

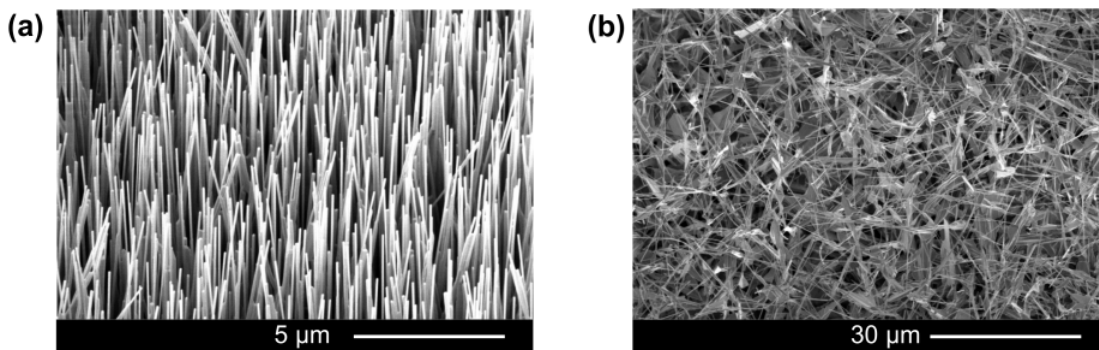


**Fig. 3.1:** SEM images of the investigated ZnO nanowire targets: (a) vertically oriented and (b) randomly oriented NWs.



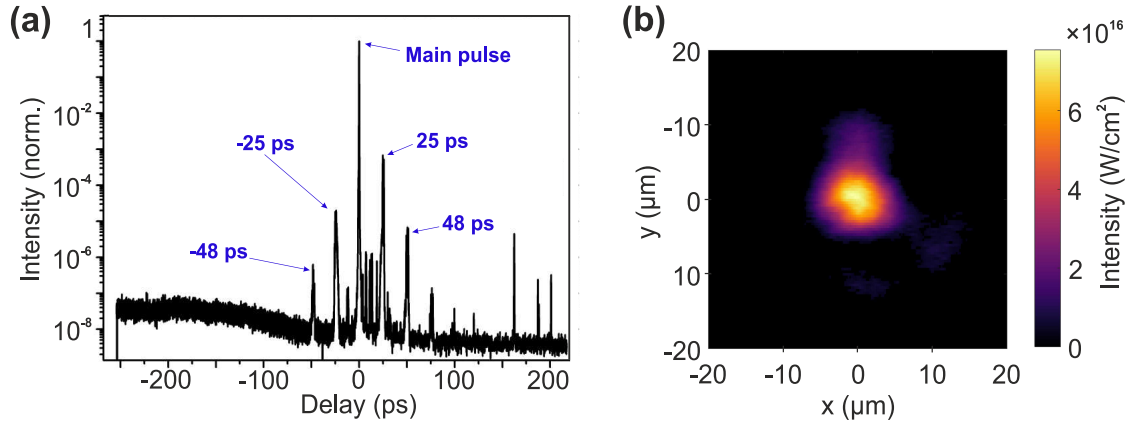


**Fig. 3.2:** (a) The pulse contrast measured with a third-order cross-correlator Sequoia. Adapted from [Hoefer14]. (b) The beam profile in the focal plane.

were repeated for the same experimental conditions on polished ZnO substrates (CrysTec GmbH) which are  $10 \times 10 \times 0.5 \text{ mm}^3$  in size and oriented along the [0001] direction<sup>1</sup>.

To drive the plasma source a 1 kHz Ti:Sapphire laser system (Quantronix), delivering pulses with the energy up to 3.5 mJ (85% of which reach the target) at the central wavelength 804 nm, was used. The temporal characteristics of the laser pulse were measured directly before the experiment, and a pulse duration of 60 fs was determined with a second-order autocorrelator. Since a strong pre-pulse can destroy NWs before the main pulse arrives dismantling any possible influence of the morphology, a good pre-pulse contrast is of great importance in our experiments. Additionally, if a formation of pre-plasma takes place, it will become quite complicated to sort out the different absorption mechanisms. However, for moderate intensities of the laser pulses ( $10^{16} - 10^{17} \text{ W}/\text{cm}^2$ ) used here, the requirements for contrast are more relaxed. So the measured nanosecond and picosecond contrast of about  $10^{-5} - 10^{-4}$  is sufficient because the corresponding fluence of  $<0.3 \times 10^{18} \text{ J}/\text{cm}^2$  is below the material damage threshold. The short delay contrast was measured with a commercially available third-order cross-correlator Sequoia (Amplitude Technologies) (Fig. 3.2(a)). Pumping laser pulses entering the vacuum chamber were focused onto the target by a  $60^\circ$  off-axis parabolic mirror ( $F/1.5$ ) to a  $6.8 \mu\text{m}$  spot (FWHM) providing the peak intensity of  $5 \times 10^{16} \text{ W}/\text{cm}^2$  (Fig. 3.2(b)). The incident angle of the laser pulse on the target was fixed to about  $41^\circ$ . The

<sup>1</sup>The direction of the growth is designated by the 4-index notation - Miller-Bravais notation. Accordingly, the orientation of the single-crystal hexagonal ZnO along c-axis can be defined as [0001].

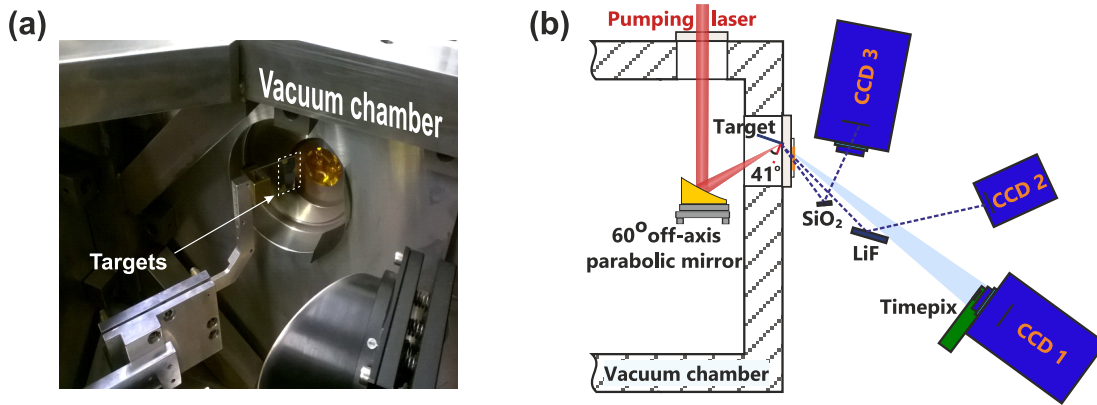


**Fig. 3.3:** (b) Interior of the vacuum chamber (photo). (a) The scheme of the experimental setup. The CCD 3 camera recording the X-rays reflected from the quartz ( $\text{SiO}_2$ ) crystal detected also signal not reflected from the crystal.

resulting laser pulse intensity onto a target surface corresponds to a normalized vector potential  $a_0 \cong 0.15 \ll 1$  implying non-relativistic interaction.

Since the Rayleigh length of the incident laser beam ( $\approx 65 \mu\text{m}$ ) is significantly longer than the NWs, the same irradiation conditions are guaranteed along the NWs. The target was mounted on an XYZ-translation stage allowing to provide a fresh spot on the target for the exposure and to change the position along the focus (Fig. 3.3(a)). With a half-wave plate the polarization of the incident laser pulses can be rotated from s- to p-polarization. Note, throughout the thesis s- and p-polarizations are used to refer to the laser pulses with the electric field oscillating perpendicular or parallel to the plane of incidence ( $kn$ -plane), respectively. A schematic representation of the electric field orientation with respect to the orientation of NWs for both of the used types of targets is given in Fig. 3.4(a,b). Along the given definition and a finite angle of incidence, p-polarized laser pulses have always a field component  $\vec{E}_p \cdot \vec{n}$  normal to the target surface. Therefore, for the vertically oriented NW targets and p-polarized light, the electrons oscillate not only along the axis of the NW but also perpendicular to them. For randomly oriented NW target, the direction of the field is not as crucial because of the chaotic orientation of the NWs.

The diagnostics were placed outside the chamber (Fig. 3.3(b)). The expected K-shell line emission and especially the hard X-rays are weakly absorbed over a propagation distance of about 1 m of air. For the line spectra measurements, two bent crystal spectrometers were set up. The first one, based on a toroidal quartz 10-1 crystal, measured spectra with a high resolution in a narrow spectral window (8.56 - 8.68 keV). This spectrometer enabled us to take a closer look at the

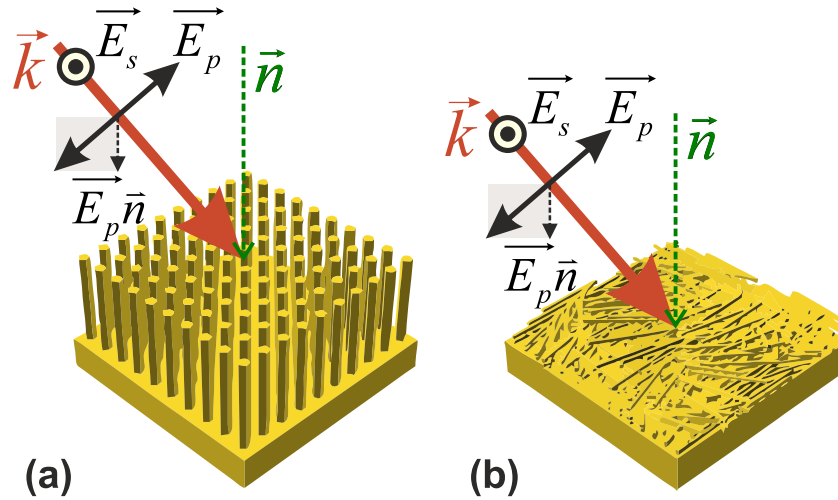


**Fig. 3.4:** The laser-target interaction geometry for (a) vertically and (b) randomly oriented NW targets (ZnO).  $\vec{E}_p$  and  $\vec{E}_s$  – p- and s-polarized electric fields of the incoming laser pulse with  $\vec{k}$ , respectively.  $\vec{n}$  – a normal vector of the target surface.

$K_\alpha$ -doublet from zinc. The second spectrometer with a cylindrically bent LiF 220 crystal works in a broader range of energies – 8.4 - 9.8 keV, which covers the band from  $K_\alpha$  to  $K_\beta$  emission lines of Zn. The detection of the spectra reflected by the bent crystals was done by cooled back-illuminated X-ray CCD cameras with their own vacuum-supporting containers (Roper and Andor - CCD 2 and CCD 3 in Fig. 3.3(b), respectively). For more details see Appendix D. Since moderate laser pulse intensity was used, there was no need to install any additional protection against disruptions by the following electromagnetic pulse (EMP).

For detecting the bremsstrahlung emission, another Andor CCD (CCD 1) camera and a Timepix detector [Hahn16] were installed. The distance from the targets for both detectors was roughly the same. However, CCD 1 with a 40  $\mu\text{m}$ -thick silicon chip is sensitive up to 20 keV, whilst the Timepix detector based on 1 mm-thick CdTe chip can register photons with energies up to 800 keV. Though, due to the dramatic decrease of quantum efficiency for higher energies, reliable measurements of bremsstrahlung spectra over a broad range with the same CCD camera are somewhat cumbersome. Additionally, the Compton scattering becomes more important for higher energies enhancing the count rate. Therefore, for higher energy X-rays, these two counter-acting processes must be carefully considered. The obtained spectra must be not only corrected for the absorption of the air and the Kapton window, but require additional Monte Carlo simulations considering the two above mentioned efficiency scaling with photon energy (e.g., [Sjoegren03; Chen09]). For our setup, test simulations have shown that for the given experimental parameters

and detected spectra the introduced correction for the absorption will be sufficient to obtain reliable data, which yet should be interpreted with caution. Therefore, we restrict our analysis to the relative comparison of the spectra. As we use no wavelength dispersive elements for measuring the continuous X-ray spectra, we have to ensure that our detectors are operated in the “single-photon counting regime”, meaning in the particular case that the ratio of the number of photons divided by the number of pixels must be  $\leq 0.15$  [Loetzsch12a]. Additionally, we have applied an algorithm accounting for the close located pixels. Briefly, each cluster of the pixels with non-zero counts was treated separately and either summed up as a single event or split into several events depending on the count distribution within the cluster (Appendix F). These technical aspects were tested in other experiments (e. g., [Loetzsch12a; Livet00]).

The experiment was conducted in a single-shot regime. The area of the target surface was large enough to take over 200 shots, providing statistically good results, i.e., the results can be summed up and averaged over many shots. The damaged area after exposure did not exceed 300 - 400  $\mu\text{m}$  in diameter, therefore, the step size of 500  $\mu\text{m}$  is sufficient. For the higher laser pulse intensities, the damaged area is obviously larger, which requires a larger step size (see Appendix G). It is worth to mention that we were able to operate the setup at 10 Hz repetition rate without applying any specially designed target holder. Firstly, the position of the target with respect to the beam focus was optimized to the highest radiation dose measured with a dosimeter and then tuned to the maximum of the X-ray signal on the spectrometers. The interaction of the laser pulse with the targets was performed inside the vacuum chamber pumped down to  $10^{-4}$  mbar.

### 3.3 Influence of the target morphology on the produced X-ray emission

In the energy region below 20 keV, the X-ray emission spectra detected by CCD 1 for different target morphologies look rather similar, especially for p-polarized laser pulse (Fig. 3.5). The spectra contain the K-shell emission lines of Zn –  $K_\alpha$  and  $K_\beta$ , as well as fake lines at twice the energy appearing due to the pile-up of K-shell photons. The signal from the polished sample strongly varies as a function of the polarization and maximized for p-polarization. In contrast, the emitted flux from

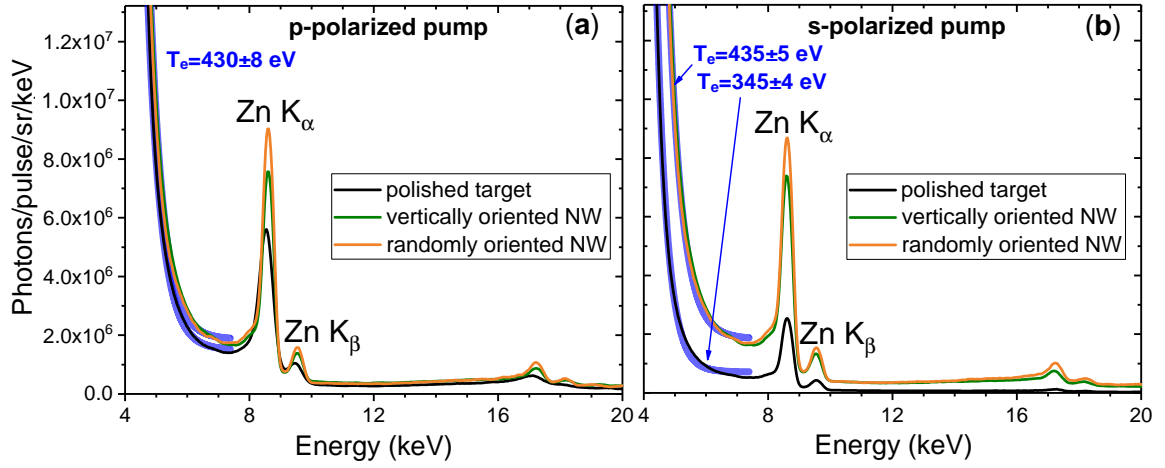


**Fig. 3.5:** The X-ray spectra from the polished and nanowire ZnO targets for (a) p-polarization and (b) s-polarization measured by CCD 1 in single-photon counting mode. The solid blue lines correspond to the exponential fits providing an estimation of the electron temperature  $T_e$ .

the nanostructured samples, especially from the randomly oriented NW sample, is almost insensitive to the laser field polarization. The integrated photon flux at 8.64 keV (Zn  $K_\alpha$ ) is about  $1\text{-}4 \times 10^6$  photons/pulse/sr, which at 1 kHz repetition rate yields about  $10^{10}$  photons/s. Comparable X-ray fluxes obtained in similar experimental conditions have been reported [Zamponi09; Uschmann09]. Having high expectations it might seem surprising, that, neglecting the polarization dependence, the NW targets emit only slightly more K-shell photons than polished ZnO samples. This observation is discussed in detail below.

For the energy region above 50 keV, the tendency for the polarization dependence remains the same (Fig. 3.6). The bremsstrahlung spectra presented in Fig. 3.5 and Fig. 3.6 suggest an electron energy distribution function (EEDF), which could be described as the superposition of several sub-ensembles of electrons with different mean temperatures. Following the approach suggested in [McCall82], we have applied an exponential fit (Maxwell distribution) to the low-energy spectra (Fig. 3.5), which yields a slope corresponding to electron energy of 350 - 435 eV. The spectra in the high energy region (Fig. 3.6) can be fitted with a two-temperature distribution revealing electron temperatures of 12 - 15 keV and 40 - 50 keV. Evidently, the uncertainty of the average energy is fairly high and is attributed to the definition of the approximation interval. Similar multi-temperature electron distributions in laser-generated plasmas have been reported in the past [Rosmej18; Ivanov13; Sherlock09; Burnett86]. The origin of such a complicated EEDF is not yet well understood. It was argued, that the observed electron temperatures are generated

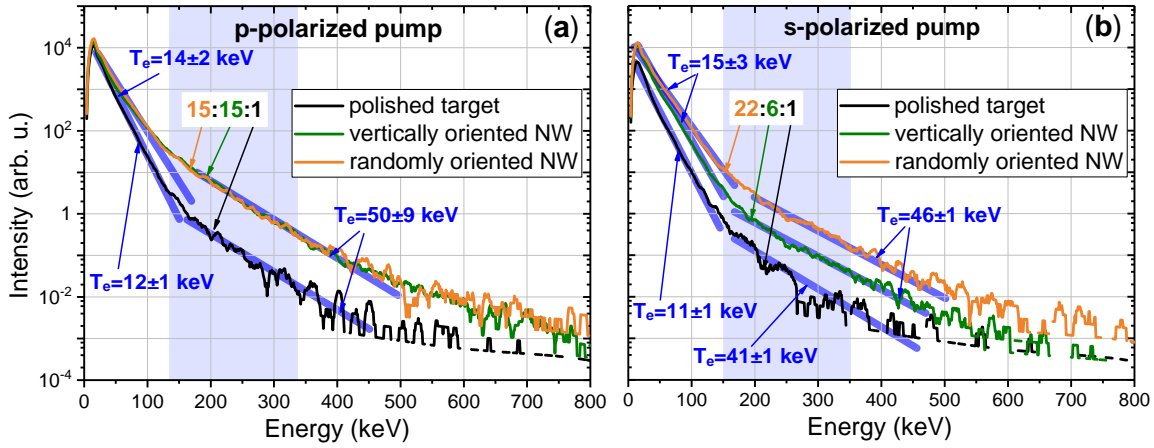


**Fig. 3.6:** The hard X-ray spectra from the polished and nanowire ZnO targets for (a) p-polarization and (b) s-polarization measured by Timepix detector. The ratios of the hard X-ray flux from NW and polished targets are given for the marked (blue) energy range. The spectra were fitted with an exponential function (solid blue lines) providing an estimation of the electron “hot” temperatures  $T_e$ .

by different mechanisms [Kruer88; Chen01]. The “hot” (suprathermal) electrons gain their energy in the electric field of the laser pulse and form two groups of electrons depending on the instant of time (phase) they become free and reenter the target [Mulser12]. Note, in the particle acceleration community, only a tiny fraction of those electrons accelerated at most is termed “hot”. The “cold” fraction of the electrons, which are also referred to as bulk electrons, is formed due to collisional heating and constitutes the absolute majority of the electrons. Generally, the dominant absorption mechanism for the given laser pulse intensity level depends on the density profile. For a high pulse contrast, like in our experiments, the formation of the pre-plasma is suppressed which leads to a sharp density profile. In this case, for oblique incidence of the laser beam Brunel (or vacuum) heating is the dominant mechanism [Brunel87; Gibbon92]. The electrons are dragged away from the target surface, turned around and accelerated back into the highly over-dense region within a half laser cycle. The interaction regime is governed by the laser polarization. It is important to notice that the detected spectra are integrated over time, meaning that emission generated at different times is summed up. Therefore, we observe the contributions from all the electron fractions ever existing during the plasma evolution. In fact, there is no widely accepted model predicting the observed electron distribution with several temperatures. More recent theoretical attempts consider many of the important processes and guess a scaling for the electron temperature but only for the hottest ones [Haines09; Chen01; Liseykina15]. The higher the intensity of the laser driver is, the more complicated EEDF and its

time evolution get. Due to the lack of a consistent and accepted model, we refrain from a quantitative comparison with the models, which is out of the scope of this work.

The hard X-ray flux obtained from the vertically and randomly oriented NW samples is significantly stronger than from the polished sample. For instance, in the region of 150 - 350 keV, we obtained 15 and 22 times higher integrated flux for p-polarized and s-polarized laser pulses, respectively (Fig. 3.6). However, the enhancement with the s-polarized driving pulse is related to a significant drop of the signal from the polished target as it has been shown for the low-energy bremsstrahlung spectra. The enhancement coefficient for the higher energy photons might be a bit higher; yet, due to the low signal-to-noise ratio, it was not retrieved. This behavior can be justified if we account for the interplay between the morphology of the sample and the laser polarization. For s-polarization, the flux of generated photons is low because the electric field of the pump has only a tangential component and the direction of the field oscillations does not assist effective electron heating. In other words, the vacuum heating is suppressed, which explains the experimental results for the polished/flat surface. Meanwhile, samples with NWs are supposed to behave differently, because NWs arrays represent elongated hexagonal prisms perpendicular to the flat surface. For any laser beam polarization, there is always a component of the field perpendicular to a surface of a NW (Fig. 3.4). So it is obvious that for s-polarized light, the vertically oriented NW are more efficient emitters of hard X-ray photons than the polished sample (6-fold enhancement for 150 - 350 keV). Despite the observed electron heating with s-polarized light, for the vertically oriented NW morphology, the p-polarized light is still more efficient to transfer energy to the electrons, which results in a higher flux. In contrast, for randomly oriented NW targets it seems the polarization plays no role. Indeed, at any orientation of polarization, there is always a component of the field normal to the local plasma gradient and responsible for the efficient bremsstrahlung. Our observations are in agreement with recent experiments using copper nanorods with similar length as NWs length (10  $\mu\text{m}$ ). Although the average density of the Cu target material [Mondal11] is higher than in our case, the reported X-ray flux is the same as in our experiments. According to the results in [Bagchi11] obtained with multiwalled carbon nanotubes, we might expect a notably higher flux if we increase the intensity above  $10^{17}$  W/cm<sup>2</sup>.

The K-shell emission spectra measured with the two crystal spectrometer for all



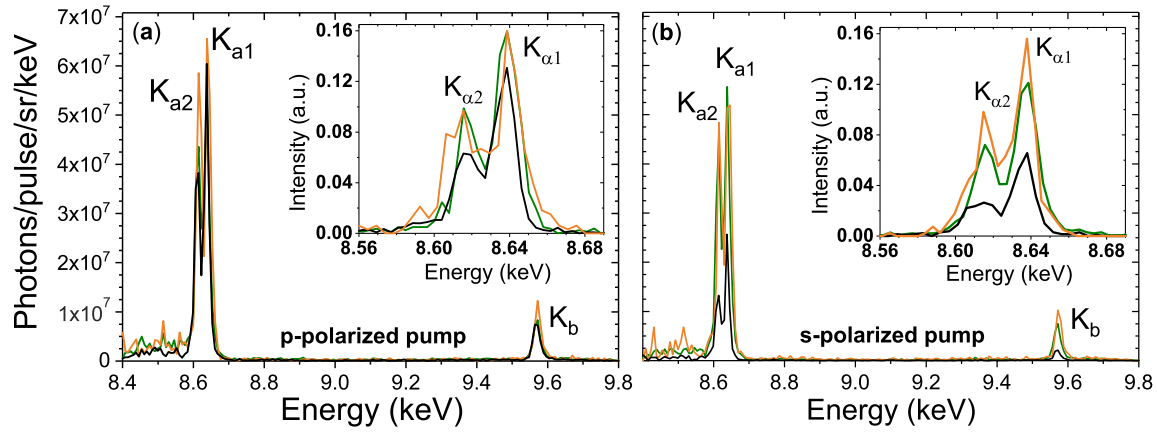


**Fig. 3.7:** The K-shell emission and  $K_\alpha$ -doublet (*Insets*) from ZnO targets (polished (black), vertically (green) and randomly (orange) oriented NW targets) detected with LiF and SiO<sub>2</sub> bent crystal spectrometers, respectively. The spectra were obtained from interaction with (a) p-polarized and (b) s-polarized laser pulse.

investigated samples are presented in Fig. 3.7. The observed lines correspond to the K-L ( $K_\alpha$ ) and the K-M ( $K_\beta$ ) radiative transitions in a cold material of weakly ionized Zn. Note that  $K_\alpha$  and  $K_\beta$  may represent a superposition of the overlapping emission lines from Zn<sup>1+</sup> - Zn<sup>20+</sup> ions. No lines indicating transitions in highly charged Zn ions were observed and, thus, no ions with the charge state higher than 20+ are generated under our experimental conditions. An accurate measurement of the  $K_\alpha$  line profile can provide more precise information about the degree of ionization in a plasma, but for that a high-resolution well-calibrated spectrometer is required. Considering the non-relativistic intensity and rather modest laser energy deposited into the material ( $\leq 3$  mJ), such a high ionization degree can be safely ruled out. For the different polarizations the line spectra show similar response as observed for the continuous X-ray spectra (Fig. 3.5, 3.6): for the vertically oriented NW target there is a weak polarization dependence, and the randomly oriented NW target shows the same emission for both polarization orientations. No significant enhancement of this characteristic line emission, also known as "cold" emission, was registered. However, this is not particularly surprising in the light of the arguments given further. The yield of the bremsstrahlung emission in the range of photon energy below 100 keV is the same or very similar for polished and nanostructured targets (see Fig. 3.5 and Fig. 3.6). Therefore, the density of corresponding electrons should be comparable for all types of targets. But these are the electrons contributing the most to the generation of the  $K_\alpha$  emission in Zn [Salzmann02]. Therefore, despite the assumed deeper penetration of the laser pulse into the NW targets and volumetric heating, the yield of the  $K_\alpha$  emission will be not enhanced.



Additionally, the hot electrons can go far into the target volume (12  $\mu\text{m}$  for 50 keV electrons) creating the K-shell holes. However, these high-energy electrons do not enhance the  $K_\alpha$  generation due to the reabsorption and absence of reflux in thick targets [Neumayer10]. Besides that, in the case of NW targets, the substrate is made of Si and, thus, this volume does not make any contribution to the Zn  $K_\alpha$ . Furthermore, the density of material for NW and flat targets is quite different (by a factor of 4 - 6). Interacting with the s-polarized pulse the randomly oriented target generates 3 times more photons at 8.6 keV (Zn  $K_\alpha$ -doublet) than the polished one, while in the case of p-polarization the increase of the flux reaches a factor of 1.31 only. Concluding the results on  $K_\alpha$  emission, it is noteworthy, that the ratios of the integrated  $K_\alpha$  fluxes from the investigated ZnO targets calculated from the data measured with two crystal spectrometers and one CCD camera (CCD 1) with no dispersive element are in a good agreement with each other. The mean values for the  $K_\alpha$  yield enhancement are given in Table 3.1. It is worth to mention that the observed polarization dependence for the  $K_\alpha$  emission has basically the same origin as the discussed above bremsstrahlung emission (both types of radiation are related to the generation of hot electrons).

	polished	vertically oriented NW	randomly oriented NW
p-polarization	1	$1.19 \pm 0.04$	$1.31 \pm 0.05$
s-polarization	1	$2.79 \pm 0.11$	$3.18 \pm 0.08$

**Tab. 3.1:** The mean values of the integrated Zn  $K_\alpha$  emission for the investigated targets obtained with p- and s-polarized laser pulse. The values are normalized on the integrated Zn  $K_\alpha$  flux from the polished sample.

In this experiment, the focus of attention was on the generation of the X-ray emission within non-relativistic laser-matter interaction. However, an interesting finding supporting our observations has been made. To record the spectrum reflected from the quartz crystal, CCD 3 has been installed as shown in Fig. 3.3(b). However, the camera also detected a signal, which was going directly to its chip and not reflected from the crystal. This background emission measured with the blocked crystal has been further analyzed (Fig. 3.8). Interestingly, for the nanostructured targets, the signal above 150 keV is especially pronounced. Moreover, it can be clearly seen that it is polarization-dependent for the vertically oriented NW and the polished samples. Since the origin of the signal had been unclear, additional tests have been made. 1) First of all, we checked whether the signal is reflected/produced by the

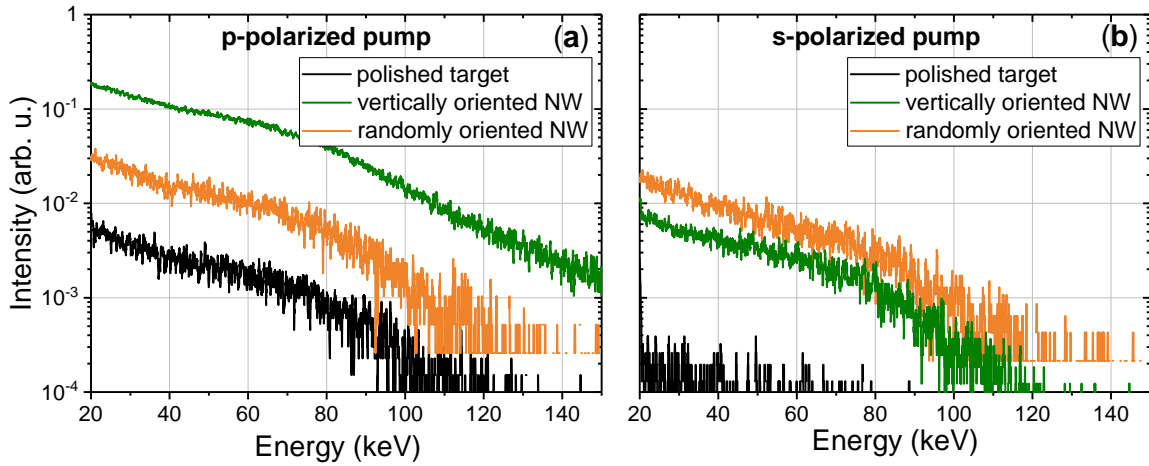


**Fig. 3.8:** The background signal from the polished and nanowire ZnO targets for (a) p-polarization and (b) s-polarization detected by CCD 3 (in quartz crystal spectrometer setup).

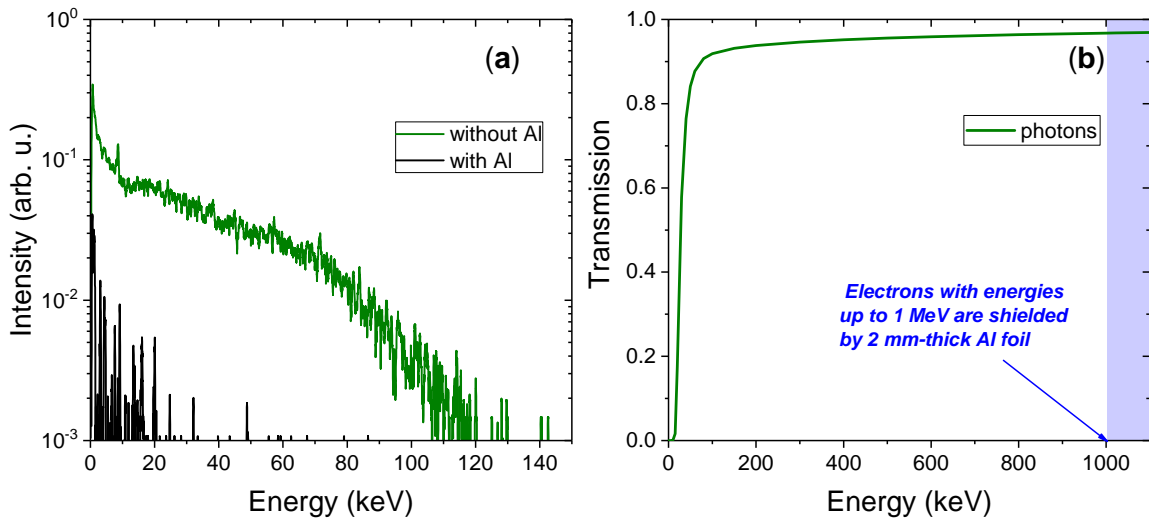


**Fig. 3.9:** (a) The test measurements of the background signal: with and without Al foil blocking the exit of the vacuum chamber. (b) The transmission of X-ray photons through a 2 mm-thick Al foil.

crystal. It appeared to be not the case. 2) When we blocked the vacuum window with a 2 mm-thick Al foil, the signal on the CCD camera disappeared (Fig. 3.9(a)). Note, such a foil transmits photons with energies over 30 keV quite well (>70% [Henke93]) (Fig. 3.9(b)), but at the same time stops hot electrons (up to 1 MeV [ESTAR]). In Fig. 3.9(b) the shaded blue area illustrates the range of electron energies starting from which electrons will not be stopped by the Al foil. The CSDA range<sup>1</sup> for a 1 MeV electron is  $0.555 \text{ g/cm}^2$  [ESTAR]. As shown in Fig. 3.8, we detected a

<sup>1</sup>The continuous slowing down approximation (CSDA) range is a close approximation to the mean path length traveled by a charged particle in a matter before coming to rest.

large number of photons above 30 keV, so we should have still registered a signal behind the Al foil if these would be photons from the target. We also exclude the influence of any secondary sources of the X-ray emission inside the chamber. Therefore, based on this simple test it can be concluded that the signal on CCD 1 is not stray light, but emission generated from a huge flux of hot electrons, which is substantially higher for the NW samples. The detected signal can be explained by X-rays emitted by these electrons colliding with each other or, simply, scattered in the air. Using the data for the radiative stopping power of electrons in the air [ESTAR], we estimate that the spectra in Fig. 3.8 can be produced by electrons with kinetic energies above 100 keV. Given that our findings are based on an indirect measurement, the conclusions we made should be treated cautiously. Nevertheless, it is evident that the NW targets irradiated by non-relativistic laser pulses can generate a stronger electron flux with energies of several hundred keV than the polished targets. This observation is supported by the enhanced hard X-ray flux.

## 3.4 Conclusions

The described in this chapter work represents the very first experiment within our study of the laser-matter interaction with nanostructured targets. Examination of the influence of the target morphology on the X-ray emission generated within the interaction with non-relativistic laser pulses is an essential step to the better understanding of phenomena to be expected at higher (relativistic) intensities. It also appeared to be a self-consistent study which may result in the development of an effective kHz hard X-ray source driven by a moderate intensity laser.

Replacing flat crystalline samples by NW targets allows enhancing the bremsstrahlung flux by 15 - 22 times in the energy range 150 - 300 keV. Moreover, photons with energies above several hundred keV (gamma range) were produced, which, to the best of our knowledge, has not been so far evident for laser-solid interaction at the laser intensity below  $10^{17}$  W/cm<sup>2</sup>. The comparison of the results obtained with different polarization of the driving laser pulse reveals the major influence of the vacuum heating mechanism for the X-ray generation in our conditions.

However, the increase for Zn K-shell emission under our experimental conditions was almost negligible. We discussed the possible explanations for this observation in Section 3.3 and concluded that it can be attributed to the density of the target material, different material of the substrate and reabsorption effects in a larger

volume of generation. Nevertheless, the number of  $K_\alpha$  photons generated per pulse is comparable with the results widely reported for copper targets (copper has one proton less than zinc) at comparable laser intensities. The experimental investigation of the role of different surface morphologies is of great importance and one can see a remarkable difference in their response. Indeed, smartly developed nanostructured targets tend to be quite advantageous for the high-repetition hard X-ray production. The results of the measurements infer that there are no strict requirements for the incidence geometry as well as for the laser beam polarization when disordered nanostructured targets, like randomly oriented NW, are employed. Our study seems to show that for the bremsstrahlung it is profitable to have nanostructured targets with a high surface-to-volume ratio. These results may, therefore, contribute to the development of an effective kHz hard X-ray source driven by moderate intensity lasers. However, the findings might not be simply generalized to the relativistic regime of interaction, where the presence of the NW might play a significant role in plasma heating.

# Relativistic interaction with short-wavelength (UV) pulses

The past decade has witnessed a rapid growth of the studies of plasmas generated with solid low-density targets at relativistic laser intensities. However, the involved physics appears to be disputable and requires further research. The investigation of the interaction of ultra-intense femtosecond pulses with nanowire targets at high temporal contrast is the primary aim pursued in this thesis. Chapter 4 addresses the relativistic regime with a short-wavelength laser driver studied within a sequence of experiments. Even for the classical case, when the interaction is performed with flat targets, only a little research has been done at high laser pulse contrast. Therefore, to enhance the current knowledge, we have first carried out an experiment with planar foils. Then, we have explored the potential of solid nanowire targets directly comparing the experimental results obtained with NW and flat targets under the same experimental conditions.

Section 4.1 discusses the possibility of generation of keV dense plasmas with planar Ti foils, evident in the experiment at JETi-40 (IOQ, Jena) suggested and led by Dr. Olga Rosmej (GSI Darmstadt/Frankfurt University). In Section 4.2 we switch to the studies performed with nanowire targets (ZnO and Si). The description of the setup with complex diagnostics is followed by the obtained X-ray and ion spectra. Using somewhat simplified X-ray spectra simulations, we examine the parameters of the generated plasmas. The observations are further summarized and interpreted in Section 4.3.

Section 4.1 reflects the essential parts reported in a joint publication [Rosmej18]. Some results of this chapter are used for preparing a manuscript [Samsonova17].

## 4.1 Interaction with planar foils

The regime of interaction, specifically, at relativistic laser intensities is governed by the temporal structure of the pulse and value of the normalized vector potential  $a_0$ . A presence of an optimized pre-pulse can strongly support the generation of a

substantial fraction of suprathermal electrons with MeV temperatures [Pugachev16; Andreev16; Ivanov17] and increase X-ray flux, generating it in a larger volume. A pre-pulse coming to the solid target some pico- or nanoseconds before the pulse peak may generate a pre-plasma and strongly modify the surface of the target. In Section 2.1.5 we discussed this aspect in detail and pointed out its importance in the case of nanostructured targets. A “clean” ultra-intense laser pulse allows the interaction of the peak intensity with a solid matter or a matter with a very short pre-plasma scale length launching an entirely different regime. This type of interaction and corresponding plasma parameters are subjects of research crucial not only for experiments with nanostructured solids but also for better understanding and optimization of proton acceleration via radiation pressure acceleration (RPA) mechanism [Kaluza04; Aurand13].

In this section, we present the key results of the joint work on the study of plasmas produced with thin Ti foils. The complex diagnostics provide an opportunity to measure directly or to infer the temperatures of different electron fractions which conform to an electron energy distribution function calculated (EEDF) with the PIC code. In order to retrieve information about electron bulk temperature and density extra efforts employing X-ray spectroscopy tools were undertaken.

The experiment was carried out at JETi-40 – a Ti:Sapphire laser system. A frequency doubled laser pulse (@ 400 nm) with an energy up to 200 mJ was focused onto the target under  $45^\circ$ . Frequency doubling is a necessary step for the pulse contrast improvement as it is discussed in Section 2.1.5. The peak intensity reaching  $1.7 \times 10^{19} \text{ W/cm}^2$  corresponds to  $a_0 \approx 1.4$ . The pulse duration was 45 fs (FWHM). Titanium flat foils with a thickness of 25  $\mu\text{m}$  were used as targets. The detectors were placed from the front and the rear side of it. An X-ray spectrometer based on a cylindrically bent Highly Ordered Pyrolytic Graphite (HOPG) crystal was oriented parallel to the target normal from the front side. The available spectral window spread over a wide range from 4.4 keV to 7.9 keV. To detect the run-away electrons in a specular direction of the incoming laser pulse, a magnet spectrometer was set. Both mentioned devices were equipped with image plates<sup>1</sup>. The bremsstrahlung spectra were measured from the rear side with a Timepix detector and a hard X-ray detector working on a filter-attenuation principle [Borm16].

---

<sup>1</sup>Image plate (IP) is a film-like radiation detector comprised of a specifically designed phosphor layer that traps and stores the radiation energy.

## 4.1.1 Measurements & Simulations

As it was discussed in Chapter 3, a full-scale simultaneous measurement of EEDF is a rather challenging task. An attempt to obtain its energetic part in this experiment was performed with the help of the electron spectrometer and Timepix detector. The measured spectra manifest that there are two fractions of electrons, like from our results in the non-relativistic regime of interaction, the mean temperatures of which are  $\sim 20$  keV and  $\sim 0.4$  MeV. The results also allowed to speculate that the bulk electron temperature corresponding to the main part of the free electrons was about 1.5 keV. The experimental spectra contain time-integrated information and some of the features existing during some short time could be wiped out. The 3D-3V PIC simulations demonstrated that at the moment when the peak of the laser pulse reaches the target, the EEDF can be characterized by 4 effective temperatures which somewhat agree with the experiment. The simulations claim that the bulk electron fraction dominates at all times, while the other fractions are present only shortly and disappear one after another after the laser pulse (within  $<100$  fs). The amount of the latter is extremely small, which brings to the important conclusion that the hot electron generation under the relativistic interaction at high pulse contrast is strongly suppressed.

Further analysis of the plasma parameters was based on the simulations of the line emission spectra from Ti foils. The K-shell radiation of highly charged ions is very suitable for the diagnostics of the bulk electron temperature and density reached in the experiment [Basov85]. The measured spectrum of the K-shell emission in the range of 4.5 - 5.0 keV is given in Fig. 4.1. It consists of the cold emission from Ti ions up to  $\text{Ti}^{12+}$  (Ni-like Ti), emission from the intermediate charge states and a group of lines attributed to  $\text{Ti}^{19+}$ ,  $\text{Ti}^{20+}$  and  $\text{Ti}^{21+}$  (Li-, He- and H-like Ti, respectively). The last group of lines was used for the plasma diagnostics. A related point to consider is that one should ensure the dominant role of the collisional ionization in approaching the highly charged states. Indeed, the applicability of the basic X-ray spectroscopy methods will be justified if there are no external fields causing ionization and excitation in few-electron ions. According to the estimations based on ADK theory [Ammosov86], the applied laser field intensity is capable to strip Ti to B-like Ti ( $\text{Ti}^{17+}$ ). Further ionization is defined by the parameters of the created plasma and must be then driven by the collisions. Moreover, to reach few-electron ion states for Ti on a sub-picosecond time scale, plasma has to be dense and hot.

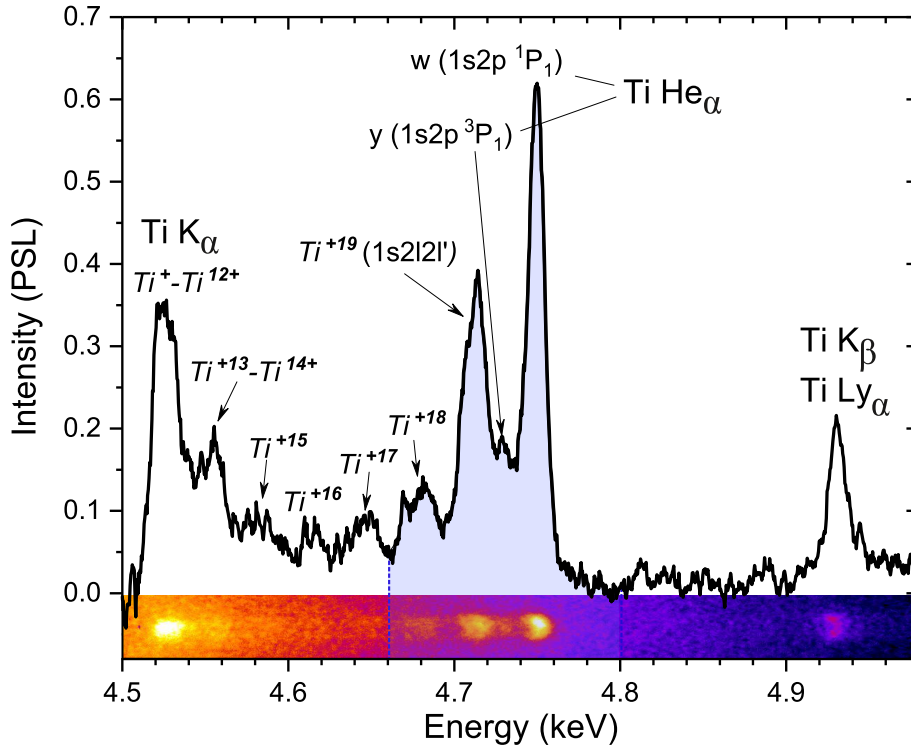


**Fig. 4.1:** K-shell emission spectrum from a planar Ti foil measured with the HOPG crystal spectrometer (the intensity is in PSL units (Photo Stimulated Fluorescence)). The shaded blue part of the spectrum corresponds to the emission from the densest and hottest plasma region. *Inset:* The spectrum recorded on the image plate before the reconstruction.

Therefore, the presence of  $\text{He}_\alpha$  and  $\text{Ly}_\alpha$  lines in the spectrum serves on its own as a proof of high electron temperature and density.

One of the methods to determine a bulk electron temperature is to analyze a sensitive to it ratio of the line intensities:  $w$ -line – He-like resonance transition ( $1s^2\ ^1S_0 - 1s2p\ ^1P_1$ ), and dielectronic satellites ( $1s^22l - 1s2l2l'$ ,  $l, l' = s, p$ ) originating from the doubly excited states of Li-like ions [Schollmeier06]. The higher the plasma temperature, the stronger the  $w$ -line in comparison to the dielectronic satellites.

To estimate electron density, the ratio of the resonance line ( $w$ ) intensity to the intercombination line intensity ( $y$ :  $1s^2\ ^1S_0 - 1s2p\ ^3P_1$ ) in He-like Ti can be used. Note that this approach can be used only for a limited number of elements if a high-density plasma is under consideration. For heavy elements, this ratio becomes sensitive for high electron densities (e.g.,  $n_e > 10^{23}\ \text{cm}^{-3}$  for Fe ( $Z=26$ )), but at the same time the emission lines get closer to each other and overlap in the spectrum. Taking into account the above discussed approaches, the hot part of the experimental spectra (Fig. 4.1, shaded blue range) was fitted with a synthetic spectrum calculated with the FLYCHK code [Chung05]. A steady-state approximation, which



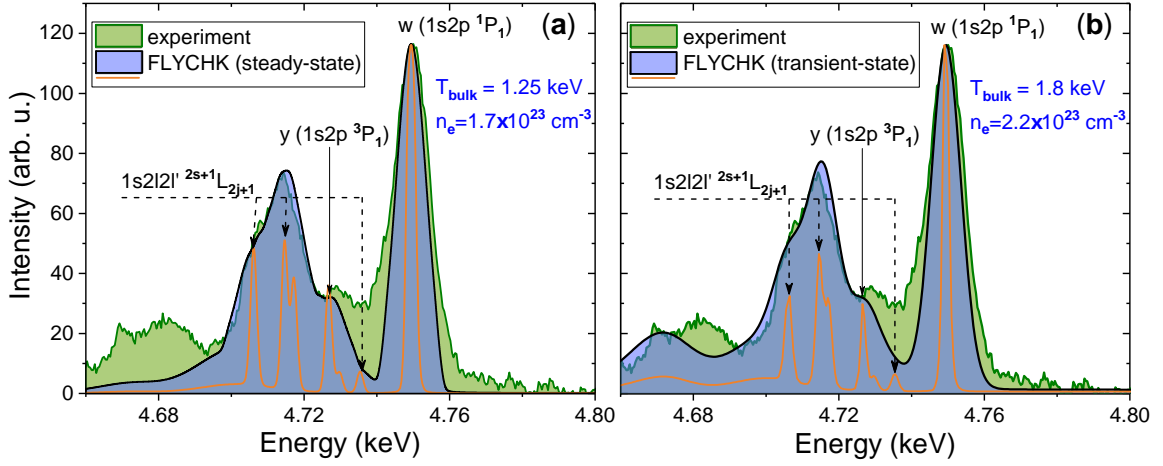


**Fig. 4.2:** The measured and the simulated X-ray spectra for the Ti foil. The simulations in FLYCHK [Chung05] are performed for (a) a steady-state approximation and (b) a transient-state plasma. The fine structure of the spectra from FLYCHK (no convolution with instrument function) visualizes the contribution of the various line groups into the final spectra (orange line).

assumes a homogeneous layer of plasma staying constant in space and time, suggests  $T_{bulk} = 1250$  eV and  $n_e = 1.7 \times 10^{23} \text{ cm}^{-3}$  for an optically thin case (Fig. 4.2(a)). Note that the critical density  $n_{cr}$  for 400 nm (the wavelength of the used laser) is  $6.9 \times 10^{21} \text{ cm}^{-3}$  and the ion solid density of Ti is  $5.6 \times 10^{22} \text{ cm}^{-3}$ . This means that the estimated density is 15% solid density. The inclusion of the opacity for expected 100 - 200 nm-thick plasma layer would result in a slightly higher  $T_{bulk}$  and  $n_e$ , while  $y$ -line and the dielectronic satellites are optically thin.

However, since the time of the laser-target interaction is shorter than the times of the collisional ionization and collisional excitation, which were estimated for the plasma parameters predicted by in the steady-state approximation. Thus, the simulations with time-dependent plasma parameters are required. The time evolution of the ion charge and the correct treatment of the forbidden transitions with long relaxation times, e. g.  $y$ -line, are meaningful for the reliable estimation of the electron temperature and density in transient plasmas [Rosmej95]. In order to get a synthetic spectrum containing the information over the plasma evolution (we considered the period up to 750 fs after the laser pulse), we used the plasma parameters predicted by the PIC simulations. The amplitude and the rate of the electron density evolution were adjusted to obtain the best agreement between the experimental and the synthetic spectra, while the ion density remained constant at the level of  $10^{22} \text{ cm}^{-3}$ . The spectrum calculated with the transient-state simulations in FLYCHK is demonstrated in Fig. 4.2(b). The calculated electron density reaches  $2.2 \times 10^{23} \text{ cm}^{-3}$ , while the maximum electron bulk temperature

$T_{bulk}$  is 1.8 keV. The fitting well describes the main features of the hot part of the experimental spectrum and, which is more, even features of the emission from  $Ti^{18+}$  (Be-like Ti) around 4.68 keV. However, in both cases, steady- and transient-state, the experimental profiles of  $\gamma$ - and  $w$ -lines cannot be reproduced due to the absence of the high order dielectronic satellites ( $1s^22l - 1s2lnl'$ ,  $n > 3$ ) in the FLYCHK code. The difference between the calculated bulk electron temperatures is notable, but not huge (1.25 keV in the steady-state and 1.85 keV in the transient-state) and the corresponding synthetic spectra look similar (Fig. 4.2). The reason for this is a high electron density and, consequently, high collisional rates governing the ion charge evolution and dynamics of the population of the excited states. Generally, under conditions of rapidly changing electron density/temperature, the temperature required to reach highly charged states is coupled to the  $n_e \times \tau_p$  parameter, where  $n_e$  is a plasma electron density and  $\tau_p$  is the plasma lifetime of the hot dense state. In the heating phase, such a plasma would reveal lower charged states than expected at those temperatures in a steady-state, and in the cooling phase the situation will be opposite. For instance, the simulations also show that the He-like Ti ions appear with a delay with respect to the laser intensity peak and emit as long as the electron energy is sufficient for the excitation (Fig. 4.3). In fact, if for the time demanded to settle a steady-state ion charge distribution the plasma density stays high, then time-integrated spectra can be analyzed in the steady-state approximation even for short-scale interaction processes as in this experiment.

Another aspect of the relativistic interaction with a planar solid, which will be important for the comprehensive understanding of the observations presented in the next sections, was studied with the help of the one-dimensional hydrodynamic simulations (1D HD) [Povarnitsyn13]. These simulations were performed for a Fe solid target and the laser parameters given above and accounted for the absorption of the laser pulse energy, ionization, electron and radiative heating, plasma expansion (procured by Prof. N. E. Andreev (RAS, Moscow)). The evolution of the bulk electron temperature in depth of the target is illustrated in Fig. 4.4. For high pulse contrast, a very sharp plasma gradient with near-solid density in the skin layer is expected. Therefore, the laser field is strongly reduced in a thin absorption layer. At the maximum of the laser pulse intensity ( $t = 0$  fs) the bulk electron temperature rises up to 2.5 keV in a top 50 nm-thick layer. The target warms up further due to the heat conductivity and at the end of the pulse the  $T_{bulk}$  already exceeds 1.5 keV within upper 100 - 150 nm. Additional experiments with Ti foils

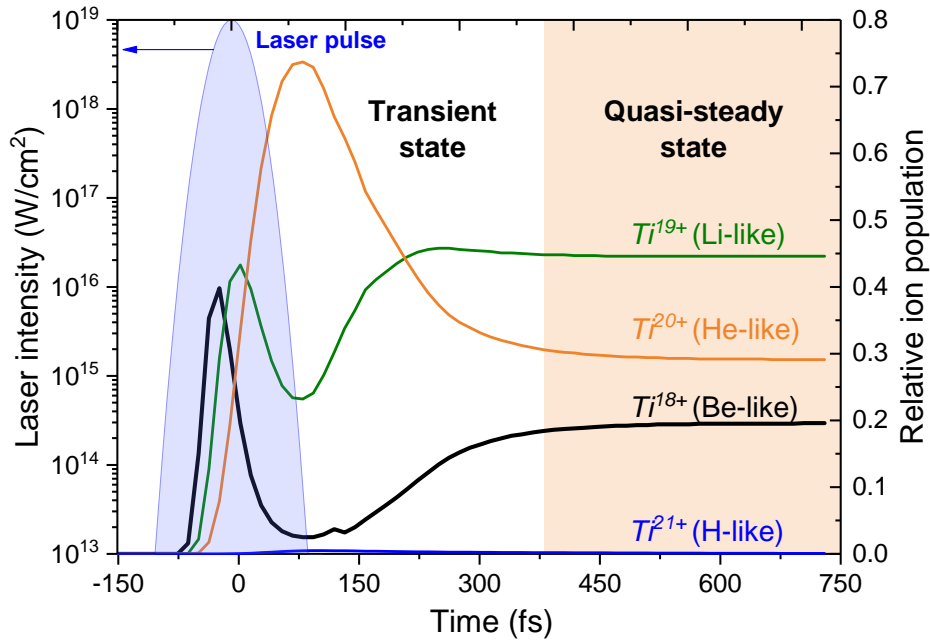


**Fig. 4.3:** The evolution of the Ti ion charge states calculated with FLYCHK code. Only the highly charged states are shown ( $Ti^{18+}$  -  $Ti^{21+}$ ).

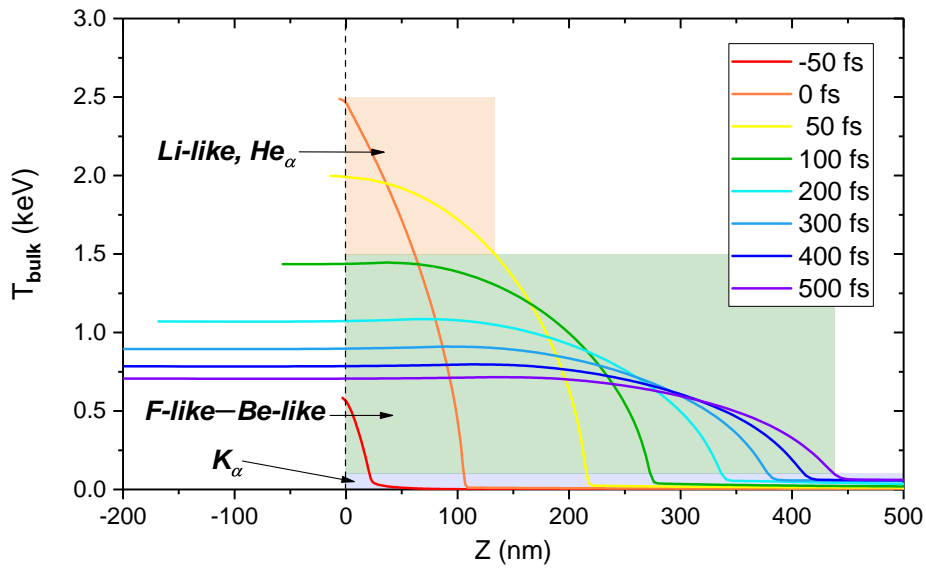


**Fig. 4.4:** Hydrodynamic simulations of the bulk electron temperature distribution  $T_{bulk}$  over the Fe target depth for different times during and after the laser pulse. The shaded areas correspond to the regions of the target from where K-shell emission in certain ion species may originate.

covered with a thin layer of Fe support this finding. In later times, the temperature drops, while deposited energy is redistributed over the thicker layer. The shaded areas (Fig. 4.4) illustrate the regions of the target where the  $T_{bulk}$  is high enough to cause collisional excitation of the certain ion species. Note, the emission from the low and intermediately charged Fe ions can be generated only with the hot

electrons, and the "cold" target region producing  $K_\alpha$  emission is significantly larger than shown in Fig. 4.4. Though the influence of the hot electrons is not included in these HD simulations, the discrepancies caused by it are considerably small because, as it was shown in the experiment, the amount of these electrons generated under our experimental conditions is rather insignificant. The inclusion of the hot electron fraction would change the initial conditions where, instead of the room temperature, a target temperature of several tens eV as a consequence of preheating by the hot electrons should have been taken. However, this did not introduce a visible change of the results because the HD code accounts for the radiative heating, which acts faster than the volumetric heating by the hot electrons. More details can be found in [Rosmej18].

In conclusion, this study has shed light on the properties of the plasma generated under a relativistic interaction with flat surfaces at high laser pulse contrast. The collisionless absorption and electron impact processes play a crucial role in the interaction with a steep density profile and the electron heat conductivity transfers the energy further. Taken together, it suggests that keV-hot near-solid electron density plasma can be obtained even with flat-surface targets. Though, the volume of such a plasma is rather limited and, according to our observations, goes about 150 nm in depth of the target. These findings are not trivial and become especially important when one speaks about the advantages of the nanostructured targets. Moreover, we have applied X-ray spectroscopy approach for the diagnostics of hot dense plasmas and discussed the relevant constraints. Using the steady-state approach it is possible to infer the electron temperature and density, which could be used as the lower limits of the real plasma parameters. Clearly, with transient-state simulations, the fitting of the experimental spectra is more accurate. But it requires a knowledge of temporal behavior of the plasma (at least  $T_{bulk}(t)$ ), meaning that additional PIC and/or HD calculations have to be conducted.

## 4.2 Studies with nanostructured targets

This section is dedicated to the series of experiments at relativistic intensities with short-wavelength laser pulses. Interaction of the intense laser pulses with nanowire targets has received much attention in the last several years. As it was mentioned in Chapter 1, a number of publications (e.g. [Purvis13; Bargsten17]) suggest that only with nanowire morphology it is possible to reach extremely high-density and

high-temperature plasma under the interaction with an intense laser pulse of ultra-high contrast. However, the superiority of this type of targets is much debated and many experts contend that the evidence provided in [Purvis13] is not conclusive. We have shown in Section 4.1 that even with metal foils it is possible to reach high electron temperature and high density of the laser-induced plasmas. In our experiments, we attempt to extend current knowledge about the physics of the laser-matter interaction at high pulse contrast. For this, we have conducted a number of experiments with ZnO and Si targets of different morphologies measuring not only X-ray emission but also ions generated under the interaction. In this section, we present and discuss a selection of our results.

### 4.2.1 Experimental setup & Targets

This series of experiments was carried out at JETi-40 as the study discussed in Section 4.1. To ensure a high temporal contrast, the laser pulse was frequency doubled pulse (to 400 nm) and, after passing several dichroic mirrors, was focused onto the target by a 45° off-axis parabolic mirror. The resulting energy of the laser pulses was in the range of 120 - 160 mJ (about 20% of the energy in the fundamental beam). A typical experimental setup is illustrated in Fig. 4.5(a). Note that the number of the dichroic mirrors and the incidence geometry varied from experiment to experiment. The focal spot was kept below 4  $\mu\text{m}$  ( $1/e^2$ ). Though the quality of the beam profile was daily optimized with an adaptive mirror in the beamline, the focal spot (its ellipticity and side features) deviated from an ideal Gaussian one. Therefore, the peak laser intensity on the target surface ranged from  $10^{19}$  W/cm<sup>2</sup> to  $7 \times 10^{19}$  W/cm<sup>2</sup>, which corresponds to  $a_0 = 1.2 - 2.8$ .

#### **X-ray diagnostics**

The K-shell line emission is of great importance for the plasma diagnostics because, as it was discussed in Section 4.1, it contains an imprint of plasma evolution. It is especially informative for interaction with femtosecond laser pulses when the excited states and ion species are short living. Naturally, the target element primarily defines the X-ray energy range we are going to measure.

For ZnO targets, a crystal spectrometer based on a cylindrically bent LiF 220 crystal and a back-illuminated Roper CCD was used in a von Hamos geometry. It was set to detect photons with energies in the range of 8.4 - 9.8 keV (as in the pilot experi-

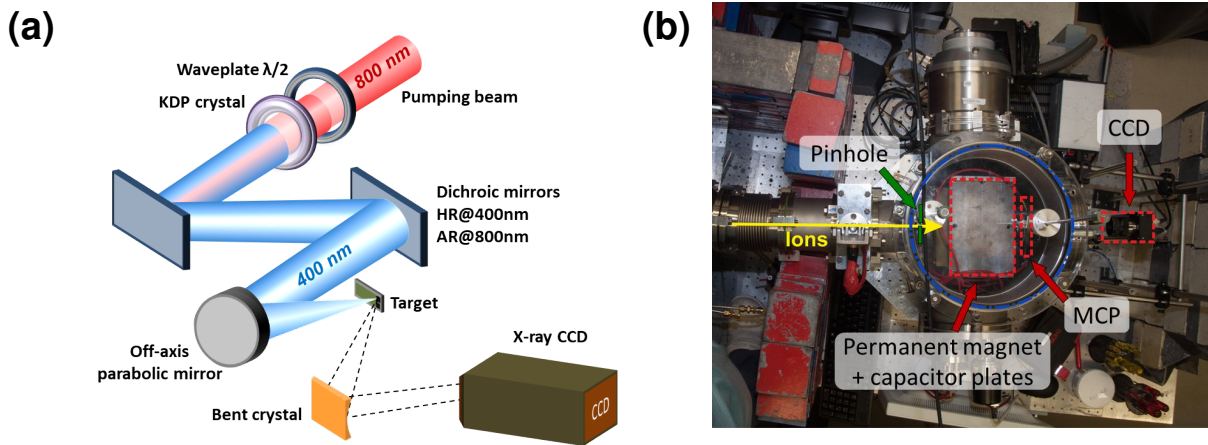


**Fig. 4.5:** (a) Simplified scheme of the setup for the experiments at JETi-40. (b) Vacuum chamber with the Thomson parabola setup.

ment described in Chapter 3). For Si targets, a flat KAP<sup>1</sup> crystal was employed as a dispersive element of the second spectrometer. Thanks to the simple geometry, it is relatively easy to adjust the energy window of the detected signal. We measured Si emission lines in two different bands: 1.7 - 2.1 keV and 1.8 - 2.7 keV. Both of the crystals were delicately shielded with a plastic housing covered with lead. The flux of the generated electrons of the target was so strong that a set of deflecting magnets had to be installed in front of the target. The CCD cameras and the controllers were stored in copper boxes and shielded with aluminum foils.

Bremsstrahlung emission was recorded with a Timepix detector placed more than 4 m away from the target. Unfortunately, the measured spectra of the continuous emission were spread only up to 150 - 200 keV which can be explained by a rather low statistical probability and extremely low number of shots per sample. In comparison with the non-relativistic interaction, the damaged area of the target after a single shot is more than 1 mm in diameter (see Appendix G).

## Ion diagnostics

We also have measured ion spectra witnessed an enhancement of cut-off energies and total flux. The Thomson parabola spectrometer was positioned on a distance of about 1 m away from the plasma source and registered ions flying in the backward direction close to the target normal (Fig. 4.5(b)). The spectrometer consists of a permanent magnet and two parallel plate capacitors, which introduce parallel to

<sup>1</sup>Potassium acid phthalate

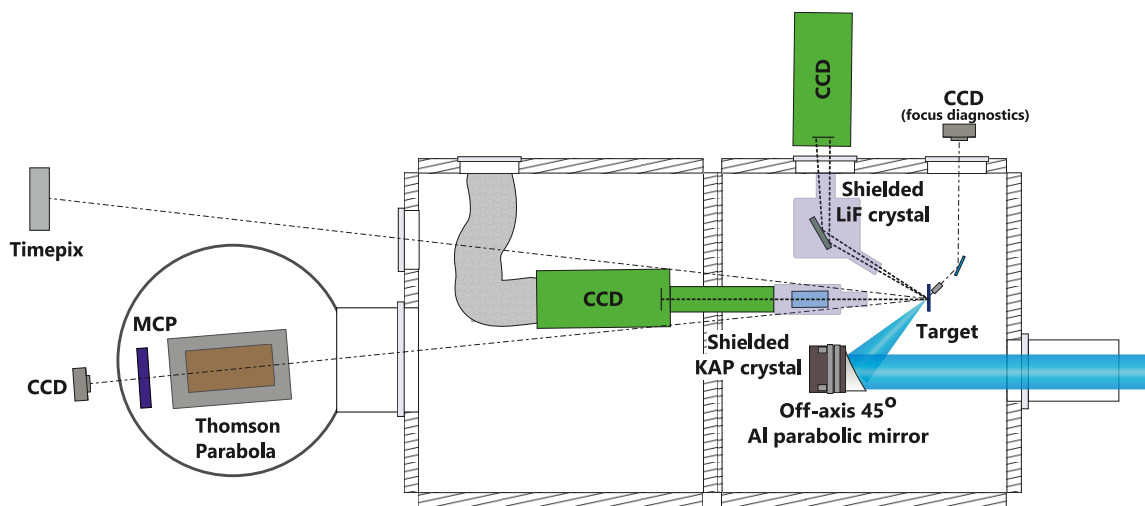


**Fig. 4.6:** The diagnostics setup (top view): two crystal spectrometers (KAP and LiF crystal spectrometers), a Timepix detector, a Thomson parabola, and a focus diagnostics setup.

each other magnetic ( $\approx 0.525$  T) and electric ( $\approx 2.8 \times 10^5$  V/m) fields, respectively (Appendix E). With this, the different ion species are separated according to their charge and energy. Two pinholes ensure that only a narrow ion beam going perpendicular to the introduced fields could reach the detector – a micro-channel plate (MCP). The signal on the MCP was registered by a triggered optical CCD.

The arrangement of the diagnostic devices can be seen in Fig. 4.6. Since the used targets are rather thick, all measurements were conducted from the front side. The crystal spectrometers were set in the orthogonal planes (their Rowland circles<sup>1</sup> were mutually perpendicular). The focus diagnostics included a microscope object, a steering mirror, and an optical CCD camera.

## Targets

The measurements have been performed with targets made of two different materials – ZnO and Si. Besides the content, the main difference between the NW targets is the synthesis/growth process (see Appendix B), which determines not only the production cost but, more importantly, the properties of the NW array. In this set of experiments, we used NW targets with up-right standing NWs only. As it was shown in Chapter 3, the ZnO NW samples (termed earlier as the vertically oriented)

<sup>1</sup>The X-ray source, the crystal, and the detector lie on the circumference of the so-called Rowland circle.



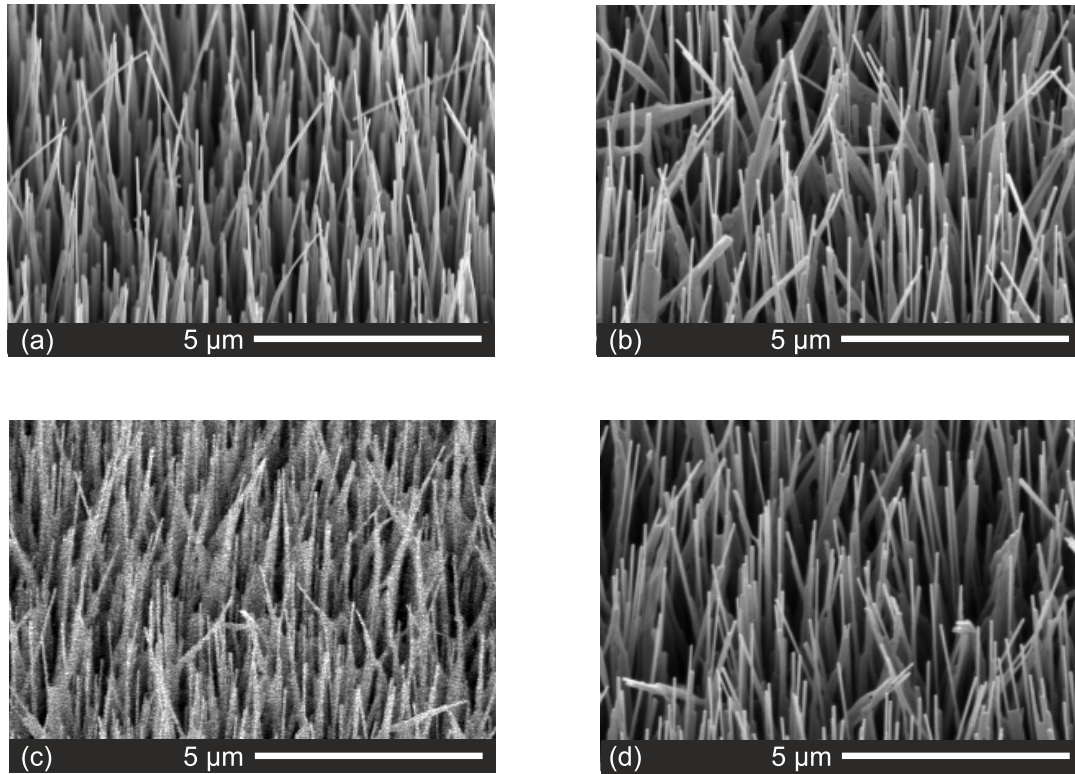


**Fig. 4.7:** SEM images of some of the investigated ZnO nanowire samples (the samples were tilted by  $20^\circ$ ).

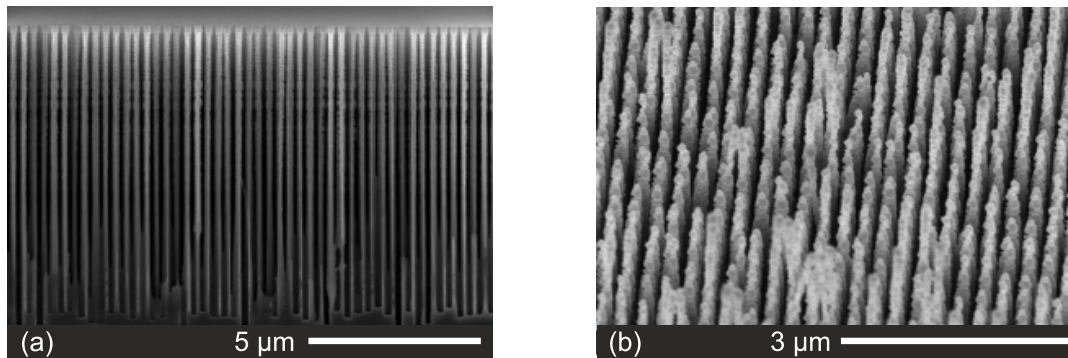


**Fig. 4.8:** SEM images of one the investigated Si nanowire samples: (a) side view; (b) the sample was tilted by  $30^\circ$ .

can be called ordered to a certain extent. Moreover, the parameters of the NW even within one sample may vary a lot. Comparing results obtained with different NW samples it is important to keep in mind possible discrepancies. However, we attempted to select similar samples for our studies (Fig. 4.7). The substrate of all the targets is  $500\ \mu\text{m}$ -thick and made of silicon. The typical NW diameter is  $60 - 90\ \text{nm}$  and its length is about  $10\ \mu\text{m}$ . It is essentially unattainable to define the material



density of the NW arrays, however, our rough estimations give about 12 - 20% of a solid density ( $\approx 4 \times 10^{22} \text{ cm}^{-3}$ ).

In contrast, the Si NW arrays are strictly periodic (Fig. 4.8). This became possible with the lithographic method used for the production of these samples. The major drawback is the complexity and time required for the production of a target. It can be seen that Si NWs are closely located (approaching 40% solid density) which is not necessarily optimal. We investigated Si NWs with a diameter of about 100 - 300 nm and a length of  $\sim 10 \mu\text{m}$ . The NWs are grown on a 500  $\mu\text{m}$ -thick silicon substrate.

## 4.2.2 Pilot experiment: normal incidence geometry

We present the results obtained within our very first campaign with NW targets at JETi-40. Being inspired by the results published in [Purvis13], we performed a similar experiment with ZnO instead of Cu targets. Though the laser pulse energy was only 150 mJ (more than 3 times less), the other parameters were rather close. Assuming that, we could have expected to observe an analogous tendency for flat and nanostructured targets. The obtained results were published in [Samsonova17]. The frequency-doubled laser pulses interacted with the target under a small incident angle ( $< 11^\circ$ ) – close to the target normal. The laser peak intensity reached  $2 \times 10^{19} \text{ W/cm}^2$  which corresponds to  $a_0 \approx 1.5$ . Despite tight focusing, the Rayleigh length (50  $\mu\text{m}$ ) was longer than the NWs. To measure the X-ray line emission, we set the LiF crystal spectrometer with a CCD camera as a detector.

The K-shell emission spectra obtained with the polished and NW ZnO targets have the same features (Fig. 4.9(a)). The most pronounced lines are the cold  $K_\alpha$  emission and  $\text{He}_\alpha$ -triplet. However, the spectral lines partially overlap with each other making it difficult to attribute the flux to a certain line. It is evident that the emission from the dense and hot plasma (high-charge states) is significantly weaker from the polished sample. The  $\text{He}_\alpha$  line emission from the NW ZnO target is dominated by the resonance line  $w$  ( $1s^2 \ ^1S_0 - 1s2p \ ^1P_1$ ) and the intercombination line  $y$  ( $1s^2 \ ^1S_0 - 1s2p \ ^3P_1$ ), whereas the intensity of the emission from  $\text{Zn}^{27+}$  (Li-like Zn) is much lower. It is remarkable that the intensity of the lines from the highly-charged ions is comparable to the intensity of  $K_\alpha$  in the case of the NW target. The corresponding flux of  $\text{He}_\alpha$  (integrated triplet) is  $7 \times 10^9$  photons/pulse which is more than 75% of  $K_\alpha$  flux. This supports the suggestion that the reached bulk electron temperature  $T_{bulk}$  is indeed higher than obtained with the polished ZnO sample.

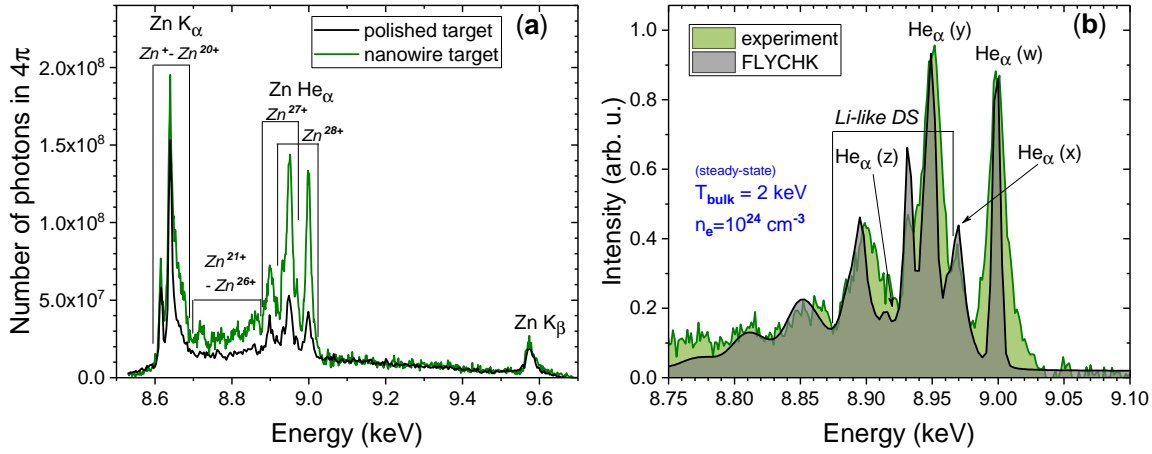


**Fig. 4.9:** (a) Spectra of K-shell emission from the polished and the nanowire ZnO targets (normal incidence). (b) The measured and simulated X-ray spectra for the Si nanowire target. The simulations are performed for a steady-state approximation.

To estimate the parameters of plasma in this experiment, we simulated the high-charge state region (from 8.8 keV to 9.2 keV) of the measured emission spectra with the FLYCHK code [Chung05]. Having no additional simulations, we used a steady-state approximation. For the NW target, the best fit of the emission lines shows that the line ratio between  $He_{\alpha}$ -triplet and Li-like lines emission can be matched only assuming  $T_{bulk} \approx 2\ keV$  and electron density of  $10^{24}\ cm^{-3}$  (Fig. 4.9(b)). Such a density corresponds to the solid-density Zn plasma fully ionized up to He-like state and is more than two orders of magnitude above the critical plasma density. The influence of a small fraction of hot electrons (several hundred keV) in our case is negligible. The thickness of a plasma layer was set to 300 nm. The bulk electron temperature can be underestimated and the electron density might be a bit lower than predicted if, in reality, the thickness is larger (the opacity effects are stronger). The attempts to fit the spectrum obtained with the polished ZnO sample (not presented here) result in a rather low electron density ( $< 10^{23}\ cm^{-3}$ ) and  $T_{bulk} < 1\ keV$ . However, we would require additional knowledge from PIC or/and HD simulations to conduct a justified spectral analysis for both cases.

This study has led us to the conclusion that with NW targets the laser-induced plasma can reach higher temperatures than with flat targets. Nevertheless, as we have also seen in the experiment with Ti foils (Section 4.1), the electron density can approach the solid density and the bulk electron temperature can reach rather high values (in keV-range). Furthermore, a high ionization degree of both types of targets observed within our experiment can be explained by a strong field ionization. A simple estimation done within Popov-Perelomov-Terentiev (PPT) ionization model

[Perelomov66] shows that Zn can be directly ionized by the given laser field up to  $\text{Zn}^{20+}$  (Ne-like Zn). However, the appearance of a strong  $\text{He}_\alpha$  emission corresponds to the ionization up to  $\text{Zn}^{28+}$  (He-like Zn), which could then be reached only by collisional ionization. Our results do not seem to confirm previously published results in [Purvis13], where the conclusions regarding a flat target are based on a spectrum with extremely low signal-to-noise (SNR) ratio. In fact, we have demonstrated that the increase in the electron temperature of produced plasmas is not sensational if present at all. The strength of the line emission speaks for a larger plasma volume in the case of NWs. Though, this point has to be dealt with in depth and supported by further deeper study and accompanying simulations.

### 4.2.3 Experiments with complex diagnostics

The next series of experiments was performed employing a complex diagnostic setup. Besides the bent crystal spectrometers, we also set a Timepix detector and a Thomson parabola spectrometer as sketched in Fig. 4.6. Assuming that the main mechanism of the laser energy absorption is Brunel mechanism (Section 2.1.3), the incidence angle of about  $45^\circ$  was chosen.

With ZnO targets we have obtained similar K-shell emission spectra as in our pilot experiment (Fig. 4.9(a)). Strong emission from the cold material followed by the K-shell emission from intermediately charged states and radiative transitions in He-like Zn were registered for the polished and nanowire targets (Fig. 4.10(a)). However, in this case, the polished sample produced significantly less emission from the highly charged ion states than in the other experiment with the same  $a_0$ . This apparent discrepancy is not entirely clear, but perhaps can be accounted for in part by the different incidence geometry and the laser pulse structure (a number of the dichroic mirrors was three instead two as in the pilot experiment). Hard X-ray emission was measured only up to 150 keV due to the bad statistics (we could accumulate only 10 - 15 shots per target) (Fig. 4.10(b)). Clearly, one should expect also photons with much higher energies (several hundred keV) to be produced under such an interaction. This would result in an energetic tail in the electron energy distribution going beyond several hundred keV [Khaghani17]. The exponential fit gives for both morphologies  $T_{hot} \approx 20$  keV. In the measured range, the hard X-ray flux obtained from the polished targets is a bit higher than from the nanowire target, which agrees with the intensity of  $\text{K}_\alpha$  line. With ZnO targets,

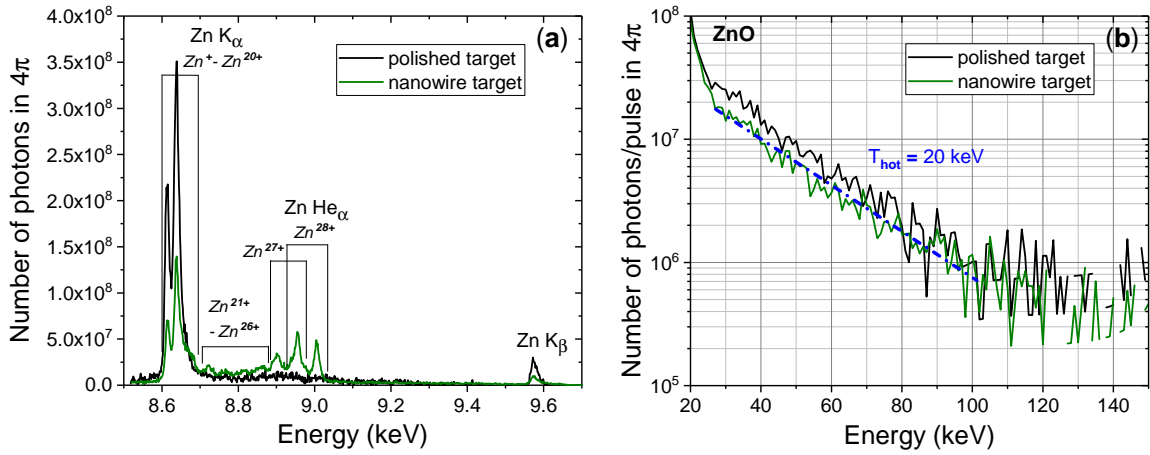


**Fig. 4.10:** (a) Spectra of K-shell emission from the polished and the nanowire ZnO targets ( $45^\circ$  incidence). (b) Hard X-ray emission spectra with an exponential fit.

we were not able to generate emission from H-like Zn (around 9.3 keV) meaning that the bulk electron temperature of the plasma was below 3 keV required for a collisional ionization of He-like Zn. However, the density of the produced plasmas (for the polished and nanowire targets) should be close to the solid density.

The fluctuations of the focus spot quality allowed us to collect data for different  $a_0$ . In these measurements, the laser energy and the pulse duration remain constant, but the laser intensity varied. From the obtained X-ray spectra we extracted X-ray fluxes for the line emission and bremsstrahlung. In Fig. 4.11(a) the relative change of the fluxes as a function of  $a_0$  is plotted. The intensity of  $K_\alpha$  line does not change much, whereas the ratio of  $He_\alpha$  lines grows. Note that this increase is related to the strong depletion of the signal from the polished Si sample, while  $He_\alpha$  emission from the nanowire sample only slightly rises. The same tendency can be seen for the bremsstrahlung emission in the range of 35 - 80 keV. The  $Zn^+$  ion spectra obtained for the different  $a_0$  follow the same trend as the X-ray emission spectra (Fig. 4.11(b)). We come back to the ion spectra in Section 4.2.5. Though the reasons for these observations are not completely understood, we suppose that the heating of the polished sample becomes even less efficient when the laser pulse intensity goes up. Increasing the intensity we move the ionization threshold of the target even further away from the peak of the pulse – the plasma can be generated earlier. The NW samples seem to be less sensitive to it and the laser energy absorption stays high. To confirm it, additional experiments with more data points are required.

Analogous measurements were performed with Si targets. The material has a rather low  $Z$  ( $Z = 14$ ) and, therefore, the role of the optical field ionization is dominant. In fact, with  $2 \times 10^{19}$  W/cm<sup>2</sup> of the laser intensity a Si atom can be stripped down to

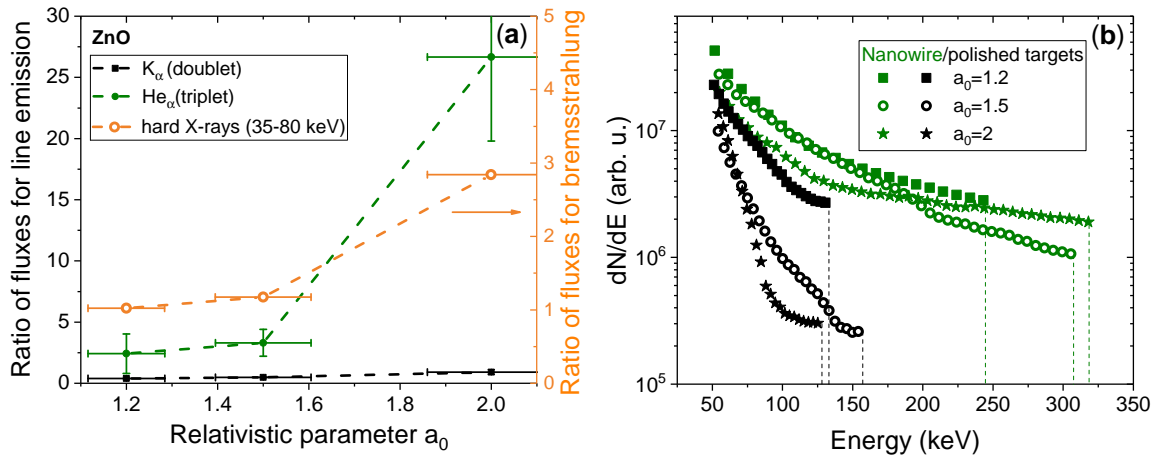


**Fig. 4.11:** (a) Ratio of the flux obtained from the nanowire sample to the flux obtained with the polished sample ( $K_\alpha$ ,  $He_\alpha$  and bremsstrahlung emission). (b)  $Zn^+$  ion spectra measured with the polished and the nanowire ZnO samples at different values of the normalized vector potential  $a_0$ .

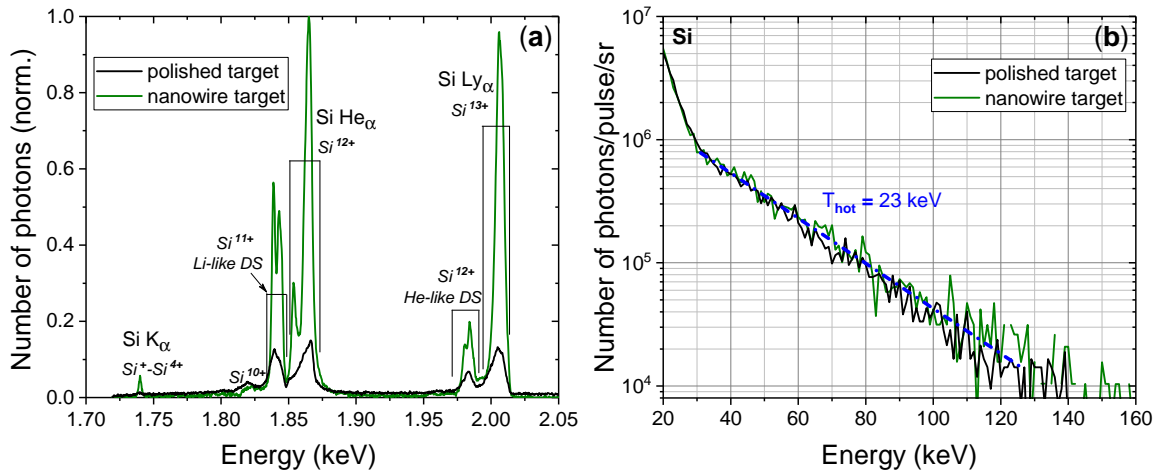


**Fig. 4.12:** (a) Spectra of K-shell line emission from the polished and the nanowire ZnO targets. (b) Hard X-ray emission spectra with an exponential fit.

the He-like state ( $Si^{12+}$ ) [Perelomov66]. Emission from He- and H-like Si prevails in all experimental spectra (Fig. 4.12(a)). However, the intensity of the lines in the case of the NW target is 10 times stronger than from the polished sample pointing out that, even if the plasma parameters are not dramatically different, the activated volume is significantly larger. As it was discussed in [Rosmej18], analysis of the relative intensities of the resonance line  $w$  and the recombination line  $\gamma$  of Si would not give information about electron density of plasma above  $10^{21}\ cm^{-3}$ . The bremsstrahlung spectra exhibit the same features as the spectra measured with a higher  $Z$  material (Zn): no visible difference in the flux and hot electron temperature in the measured range (Fig. 4.12(b)).

## 4.2.4 Si plasma: towards Rydberg states

Further increase of the laser intensity and new setup of the KAP crystal spectrometer enabled investigations of the X-ray emission in a new spectral region – up to 2.7 keV. Tight focusing of the laser beam and higher conversion efficiency of SHG allowed us to reach intensity up to  $7 \times 10^{19} \text{ W/cm}^2$ , which corresponds to  $a_0 = 2.85$ . The available spectral range covered not only K-shell emission lines from few-electron ions but also Rydberg series<sup>1</sup> of He- and H-like Si. The experimental spectra corrected on the absorption on the propagation (12  $\mu\text{m}$ -thick Mylar foil and 400 nm-thick Al foil) are shown in Fig. 4.13. Lines up to  $\text{Ly}_\delta$  (K-O transition) can be clearly seen in the spectra. The number of the Rydberg lines in the spectra is restricted due to the lowering of the ionization potential in dense plasmas. Theoretically, it is possible to use the cut-off of Rydberg lines for electron density diagnostics. The higher the density of the plasma, the lower the number of the observed lines. However, it is rather hard to make any reasonable conclusion about the cut-off from the experimental spectrum. Note that the size of the CCD chip limited the spectral range and is responsible for a cut-off around 2.7 keV (see Fig. 4.13). Another possibility to retrieve the plasma parameters is to analyze the Stark-broadening of the line profiles of Rydberg series [Stambulchik08]. Due to the evolution of the ion charge states and population of the excited states, the observed emission lines correspond to the hot and dense part of the plasma at its different evolution stages, i.e., each group of lines represents different combinations of bulk electron temperature and electron density. Therefore, the idea is to consider each group separately and calculate the Stark widths of the lines. However, the method requires a knowledge of the plasma size, since the opacity effects may strongly modify emission lines. The corresponding simulations are already in progress. The first rough estimations suggest that the bulk electron temperature of the generated plasma reached several keV. The analysis of the line broadening shows that the electron density obtained with the polished target appeared to be higher than with the NW targets. Although, the difference is not striking. Keeping in mind that average material density of the NW array is about 3 times smaller than the solid density (flat target), it is remarkable that the intensities of the emission lines in Rydberg series obtained with the Si NW target are significantly higher ( $\sim 10$ ) in

---

<sup>1</sup>Emission lines corresponding to the radiative transitions in highly excited ions.

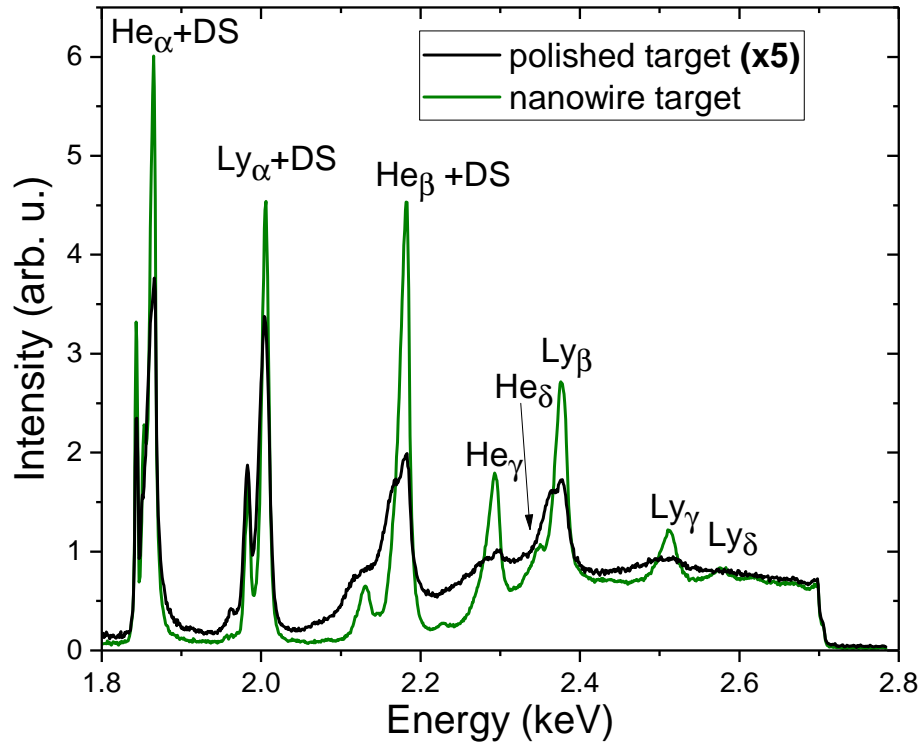


**Fig. 4.13:** Emission spectra of He- and H-like Rydberg ions measured from the polished and nanowire Si targets. The spectrum from the polished target is 5x magnified.

comparison with the polished target. This can be explained by a larger plasma volume or/and longer lifetime of a hot dense plasma in the case of NWs.

## 4.2.5 Ion generation

The effect of the target nanostructuring on the acceleration of the ionic species has been explored much less than X-ray and electron generation. Although, the laser-driven generation of fast ions and protons itself has attracted widespread interest in the past decades [Badziak07; Roth14]. In the scheme which employs thick targets (like in our case), the ions are emitted in the backward direction. The question we addressed in our experiments is whether the ion acceleration can be more effective when we use nanowire targets instead of flat ones and which ion species can be observed. The images of the ion tracks measured with the Thomson parabola spectrometer illustrate a diversity of ion species produced with the polished and the NW Si targets (Fig. 4.14). Being rich on a number of the detected tracks, Fig.4.14(b) shows also that the amount of the produced ions (brightness) and cut-off energies are increased in comparison with the image from the polished target (Fig. 4.14(a)). Besides Si ions produced from the target materials, C and O



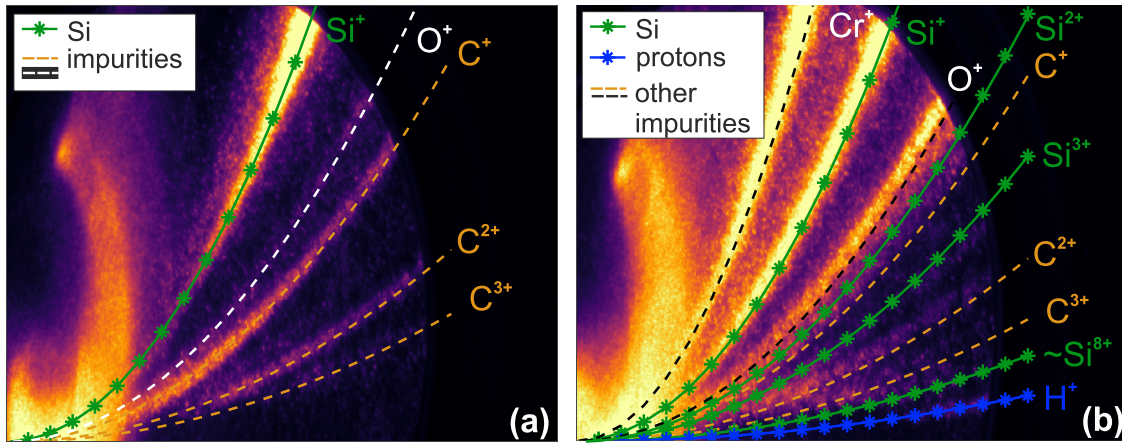


**Fig. 4.14:** MCP images of the ion spectra recorded from the polished (a) and nanowire (b) Si targets. The traces of the identified ions (Si and impurity elements) are marked.

ion tracks coming from impurities were detected. One can also see a  $\text{Cr}^+$  ion track originating from the residual chromium layer used during the target fabrication. Moreover, a weak proton signal was observed only with the NWs. The number of the  $\text{Si}^+$  ions was enhanced by more than an order of magnitude (Fig. 4.15(a)). The cut-off energies are  $\sim 190$  keV and  $\sim 360$  keV for the polished and the NW Si targets, respectively. The trend is valid for the ZnO targets too (Fig. 4.11(b)). The corresponding cut-off energies of  $\text{Zn}^+$  spectra reached with NWs are 2 times higher than with the flat-surface targets (about 300 keV instead of 150 keV). The increase of the ion energy was also observed for the impurities, for instance,  $\text{C}^+$  (see Fig. 4.15(b)). Similar findings were reported in [Dalui15], when the measurements were performed with nanoparticle coated Cu targets. Analogously, we confirm the preferential acceleration of weakly ionized target ions ( $\text{Si}^+$  and  $\text{Si}^{2+}$ ,  $\text{Zn}^+$ ) over protons. This conclusion seems to contradict to expectations that ions with a lower charge-to-mass ratio are easier to accelerate and, thus, their tracks should dominate. Nevertheless, it can be reasonably assumed that ions may undergo a charge reduction by capturing a free electron or even get neutralized [Dalui17]. Clearly, neutral atoms do not produce any parabolic trace but hit an MCP around the zero-deflection point. A three-step model of neutralization has been suggested in [Tata18] (Fig. 4.16). First, the material is getting ionized on the leading front of the laser pulse. Then the main pulse excites an electrostatic wave at the top layer of the target resulting in a strong charge separation field. At the last step, ions capture free electrons co-propagating with them in the expanding plasma. At high pulse contrast, as in our experiments, the charge transfer is expected to have a rather low probability. However, it has



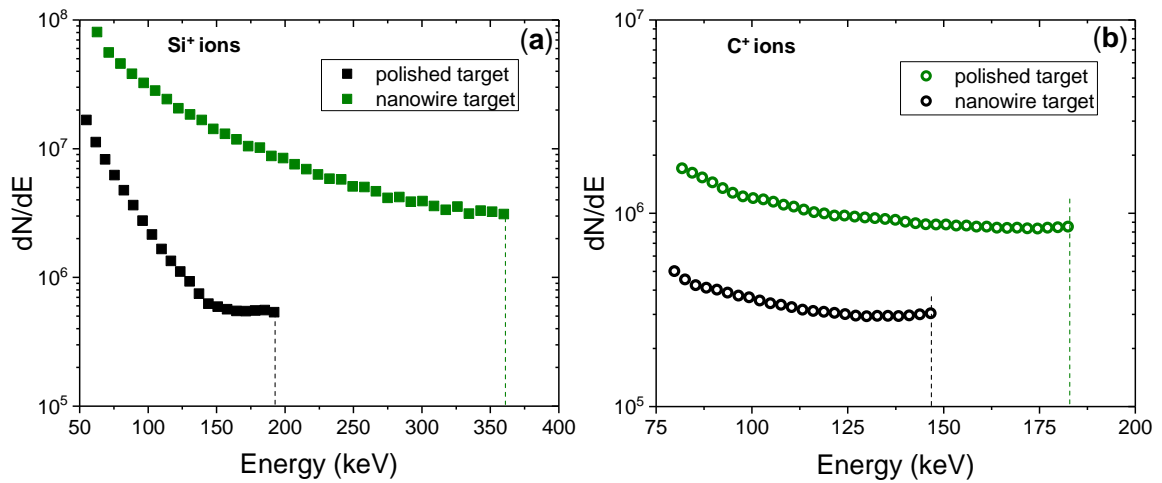


**Fig. 4.15:** Reconstructed ion spectra from the polished and nanowire Si targets: (a)  $\text{Si}^+$  ions, (b)  $\text{C}^+$  ions.

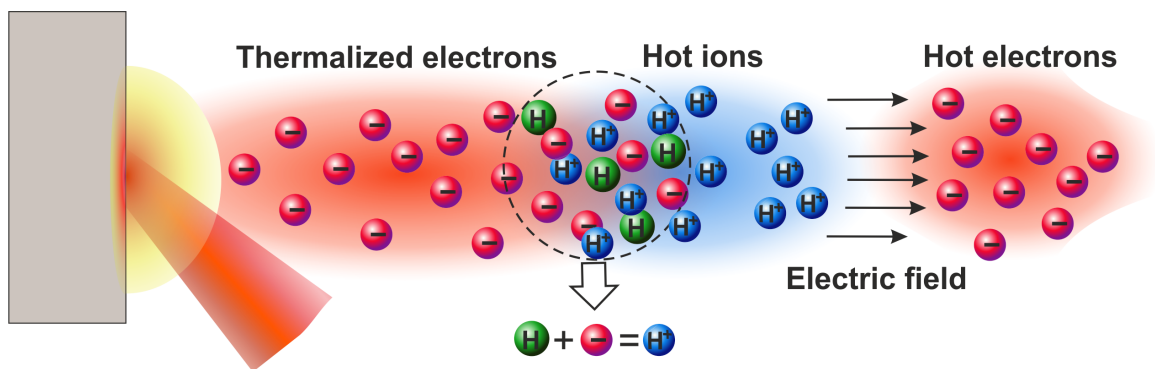


**Fig. 4.16:** Scheme of ion acceleration and neutralization with a cold bunch of co-propagating electrons. Adapted from [Tata18].

been shown that the situation is more complicated. It is very likely that the detected by the Thomson parabola ions were emitted long after protons left the target. Their acceleration in this case could be explained not by the electromagnetic forces but by thermokinetic forces. According to our results, the energies of these ions are quite low (several hundred keV) which supports this hypothesis. The hot electrons are too fast to contribute to the neutralization or charge transfer, but the bulk electrons could play a major role in it. The relative velocities of these electrons (in the ion reference frame) are low what increases the interaction time and length. Though we assume the number of free electrons and ions produced under relativistic laser-matter interaction with nanostructured targets is higher than with polished ones, it stays unclear whether NWs somewhat influence the neutralization process.

## 4.3 Conclusions

In this chapter we have presented original results on relativistic laser-matter interaction at high pulse contrast. We can indicate the main findings regarding the influence of NW morphology compared to polished targets in a few points:

- we have evidenced that keV-hot solid density plasma can be produced from both polished and nanowire solid targets under interaction with ultra-high temporal contrast, relativistically intense ultra-short laser pulses;
- we have observed a significant (an order of magnitude) enhancement of the X-ray emission from the highly charged ions when NW targets were used. This supports the assumption that NW targets enable more effective heating of the plasma volume which is significantly larger than possible with polished targets;
- we have performed spectroscopic analysis and numerical simulations supporting the previous points;
- we have archived a strong increase in the ion cut-off energy and ion flux for the NW targets.

It is worth to mention that the performed experiments were carried out using different materials (Si, Ti, ZnO). However, the observed tendencies are consistent with each other and the results are reproducible. We are aware that the performed studies are rather broad and, therefore, cannot deal in depth with all possible aspects of the relativistic interaction with nanostructured targets. Nevertheless, we were able to make the first important conclusions and have specified further promising techniques to be applied to the already obtained data.

# Relativistic interaction with long-wavelength (mid-IR) pulses

” *The important thing in science is not so much to obtain new facts as to discover new ways of thinking about them.*

— **Sir William Lawrence Bragg**  
(Physicist and Nobel Prize winner, 1915)

Recent progress in powerful laser systems delivering milli-Joule femtosecond pulses in the spectral range above 2  $\mu\text{m}$  opens a new page in the development of plasma-based X-ray sources. Unfortunately, far too little attention has been paid to the study of plasmas generated in such conditions, which would be an important step to exploit the arising advantages. Chapter 5 presents the findings of the research related to the interaction of mid-infrared ultra-short laser pulses with nanowire targets.

In Section 5.1 we discuss the novel regime of the interaction pointing out its main features and emphasize the principal differences in the physics of laser-plasma interaction with short- and long-wavelength drivers. All corresponding experimental campaigns were carried out in collaboration with the group of Prof. Baltuška (Vienna University of Technology). The setup and the experimental conditions are described in Section 5.2. In Section 5.3 the X-ray spectra obtained with different targets are presented. In the subsequent Section 5.4, we show the results of the PIC simulations conducted by Vural Kaymak and Prof. Alexander Pukhov (Heinrich-Heine-University Düsseldorf) and demonstrate simulations performed with the FLYCHK code. Finally, in Section 5.5, we elaborate on the experimental and theoretical results and conclude the chapter.

Parts of this chapter are submitted for publication [Samsonova19].

## 5.1 Novel regime of interaction: *pro et contra*

The absolute majority of the studies have been conducted with lasers in the visible or near-infrared wavelength range as a driver. However, in comparison with commonly used Ti:Sapphire (800 nm) and its frequency doubled pulses (400 nm), the longer duration of an optical cycle of mid-infrared laser pulses allows the electrons to gain more energy from the field. The relativistic interaction determined by the condition  $a_0 \geq 1$  is reached for long-wavelength sources at lower intensities than for a short-wavelength source. In other words, with moderate energy, a mid-infrared driver can still accelerate electrons to velocities comparable to the ones achieved with high-energy short-wavelength drivers since the ponderomotive potential  $U_p$  scales like  $\lambda^2$ . Not surprising, the relativistic threshold ( $a_0 = 1$ ) in laser-matter interaction was first approached at the late 1970s with the development of high energy CO<sub>2</sub> lasers [Burnett77]. However, the pulse duration of the used laser systems was in the nanosecond range, which means that the produced plasma is long-living. Therefore, the duration of the X-ray emission produced under the interaction becomes longer, making them less attractive for many applications. Also, at this time scale, the hydrodynamic expansion during the pulse prevents plasma densities above the critical value.

One of the key differences between long- and short-wavelength drivers is a *mechanism of field ionization* at the beginning of the interaction. This is directly connected to the problem of the temporal pulse contrast which may arise. While mid-IR laser pulses start to ionize matter via tunnel regime, short-wavelength pulses of sufficient intensity can ionize matter via MPI or directly via the photo effect. In the first case, the ionization rate  $\propto \exp(-1/E_L(t))$  ( $E_L$  is the laser field amplitude) at the leading front of the laser pulse will be significantly smaller than for MPI [Wu08]. The reason for that is that the corresponding photon energy of these pulses is close to the work function of the target material. The typical value of the work function in metals is  $\sim 5$  eV and  $\sim 4$  eV, in semiconductors, like ZnO and Si. As a result, a laser pulse with an ideal Gaussian temporal profile and with e.g.  $10^{19}$  W/cm<sup>2</sup> at  $0.4 \mu\text{m}$  (corresponding to  $a_0 \sim 1$ ) will ionize the target surface and create a critical density plasma already before the arrival of the peak intensity (roughly 3 times the laser pulse duration before). Calculations based on the Keldysh model [Keldysh65] show that for a typical pulse duration of 40 - 50 fs the critical density of plasma will be reached  $>100$  fs before the peak in the ideal Gaussian pulse. This behavior becomes

more apparent with higher laser intensities when the onset of ionization will shift even further away on the leading front of the laser pulse. For real laser pulses, this will happen several hundreds of femtoseconds before the peak arrival. On the contrary, for laser pulses at, for instance,  $3.9\ \mu\text{m}$ , the photon energy is as low as  $\sim 0.3\ \text{eV}$ , so only the tunnel ionization takes place. The effective length of the pulse (the time during which ionization takes place) then is considerably shorter. Thus, a significant reduction of the ionization rate is achieved with long-wavelength mid-IR laser pulses, which enables sharp spatial gradients in the plasma density. Note that further ionization in both cases goes via electron impact ionization (Section 2.1.1). For Ti:Sapphire systems based on CPA, the problem of achieving a *high pulse contrast* needs a special treatment (see Section 2.1.5). But since the same relativistic regime of interaction can be realized with a femtosecond long-wavelength laser source at a substantially lower intensity, the issue of the temporal contrast of a long-wavelength driver is much more relaxed. But even then it is essential to know the pulse structure on a nano- and picosecond time scale. As it was mentioned in Chapter 3 and 4 the pulse contrast plays a crucial role in the experiments with nanostructured targets, since any pre-pulse may significantly diminish the volumetric heating effect enabled by the nanowire morphology. Therefore, in our study special attention was paid to the examination of the pulse structure of the used laser system, discussed in the next Section (5.3).

However, the above-mentioned advantages of a long-wavelength relativistic driver can be significantly diminished by *the unfavorable scaling of the critical electron density with the wavelength:  $n_{cr} \propto \lambda^{-2}$* . For the  $3.9\ \mu\text{m}$  (mid-IR) wavelength used in our experiments, the critical electron density is  $7.3 \times 10^{19}\ \text{cm}^{-3}$ . Therefore, a plasma electron density of  $10^{23}\ \text{cm}^{-3}$  (solid density) would correspond to 1000  $n_{cr}$  and hence the laser energy coupling to the plasma would be highly inefficient. In contrast, for  $400\ \text{nm}$  the critical density  $n_{cr}$  is about  $6.9 \times 10^{21}\ \text{cm}^{-3}$ , and as it was shown in Chapter 4 we have obtained solid density plasmas for both, Ti foils and nanostructured targets (ZnO/Si). Whether such extreme densities can be reached with a long-wavelength driver and, more specifically, in the weakly relativistic laser-matter interaction regime with  $a_0 \approx 1$  at all, is a provocative question, which has not been studied yet.

Weisshaupt et al. [Weisshaupt15] have proposed the application of mid-infrared drivers to achieve an increased flux of the characteristic emission, although arguing that there will be no significant difference when modifying the target surface. This

seems to be a reasonable statement for cold emission (from weakly ionized atoms). In particular, it has been recently demonstrated that the  $\propto \lambda^2$  efficiency of vacuum heating is higher using mid-IR driver pulses compared to near-IR pulses, resulting in an enhancement of the  $K_\alpha$  emission from a Cu tape at the equivalent intensity [Weisshaupt14; Weisshaupt15]. However, no research about plasma parameters generated under such conditions has been conducted. In our work, we show that highly overdense and hot plasmas can be generated. Moreover, comparative studies of the polished and nanowire targets, explained in the following sections in detail, lead to the important fundamental result that the potential of long-wavelength laser pulses to generate extreme plasma states can be exploited fully only with a nanostructured morphology of a solid.

## 5.2 Experimental setup

The experiments presented in this chapter were carried out at the high energy OPCPA laser system developed at the Technical University of Vienna. It delivers 90 fs laser pulses at the 3.9  $\mu\text{m}$  idler wavelength with an energy on target up to 25 mJ at 20 Hz repetition rate [Andriukaitis11; Shumakova18]. Since the initial beam (out of the laser system) has a diameter of 18 mm (FWHM), the beam was expanded 4.5 times using a telescope in order to achieve a small focus spot on the next stage. After several meters of the propagation in the air, the p-polarized laser

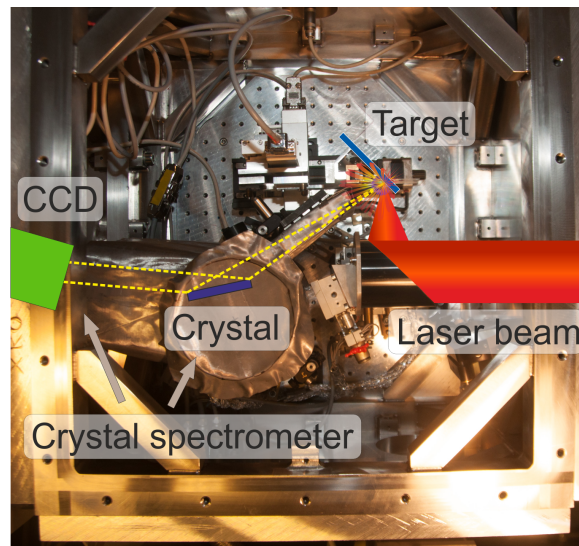


**Fig. 5.1:** Vacuum chamber with the experimental setup.

pulse was finally entering the vacuum chamber through a 35 mm-thick  $\text{CaF}_2$  win-

dow with an anti-reflection coating, where it was focused by an off-axis parabolic mirror (Fig. 5.1). In the performed campaigns, the targets were irradiated under  $0^\circ$  and  $45^\circ$  incidence angles with respect to the normal. Though the experimental conditions were slightly different, the resulting intensities on the target in both of the case were comparable (see Table 5.1). The maximum peak intensity at the target was estimated to be  $10^{17}$  W/cm<sup>2</sup> resulting in a maximum value of  $a_0 \approx 1.1$ .

	Beam diameter (FWHM)	Intensity
Experiment 1: $0^\circ$	13.5 $\mu\text{m}$	$1.1 \times 10^{17}$ W/cm <sup>2</sup>
Experiment 2: $45^\circ$	11.5 $\mu\text{m}$	$9.7 \times 10^{16}$ W/cm <sup>2</sup>

**Tab. 5.1:** Focus parameters for the experimental series at OPCPA laser system (3.9  $\mu\text{m}$ ).

The focal beam size was measured by the knife-edge scan method [Arnaud71; Skinner72; Khosrofian83], because the resolution of the available mid-IR CCD camera was too low to measure the beam profile directly. Though the sensitivity of a standard CCD with a Si chip is pretty low for mid-IR light, it was used to optimize the beam profile. Certainly, the observed signal on the CCD most likely corresponds to one of the harmonics generated in the air by the fundamental beam. However, this method allowed to align the parabolic mirror correctly.

The passage through optical elements (in our case a negative lens of the telescope and the CaF<sub>2</sub> window) influences the pulse duration. In the mid-infrared region ( $\lambda = 3 - 20$   $\mu\text{m}$ ), the sign of GVD (Group Velocity Dispersion) of most transparent materials changes from positive to negative. Furthermore, the pulse is getting recompressed due to the propagation in the air, which has a GVD anomaly in the spectral range 3.5 - 4.2  $\mu\text{m}$  [Voronin17]. Therefore, the chirp of the pulse was optimized in the compressor to get the shortest pulse possible in our configuration. The pulses were characterized by SHG FROG measurements (Fig. 5.2).

In the previous section, we addressed the problem of the pulse contrast and pointed out the advantageously low ionization rate of a long-wavelength driver in comparison to a short-wavelength laser source. Speaking about short-wavelength sources in this dissertation, we refer to laser systems based on CPA, since mostly such laser systems are used for laser-induced plasma experiments. However, the long-wavelength laser system used in this study has principal technical deference influencing the temporal structure of the generated pulses. In conventional CPA laser systems, the temporal contrast at the ns-ps time scale is determined by the level of the amplified spontaneous emission and amplified parasitic pre-pulses.

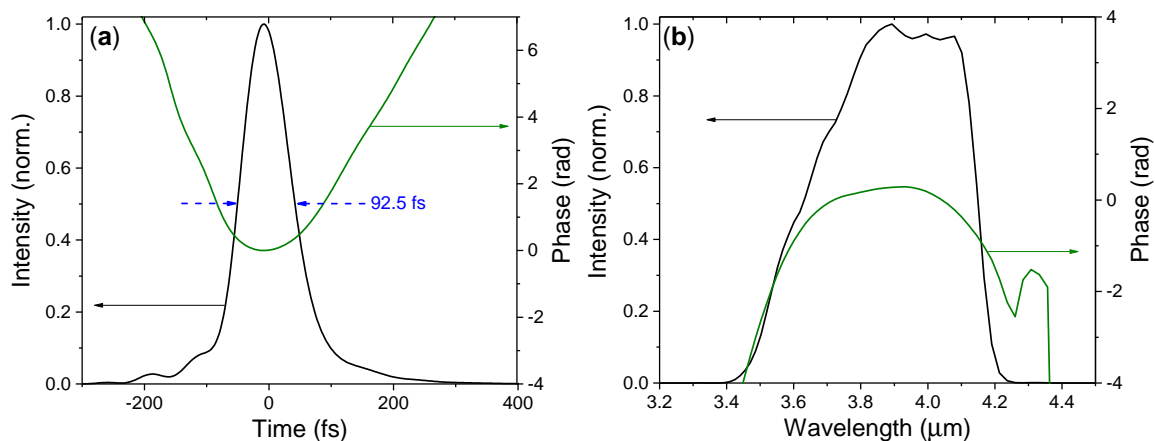


**Fig. 5.2:** Retrieved pulse parameters in (a) the time and (b) the frequency domains for the idler of OPCPA.

For OPCPA, the temporal structure of the output pulse is mainly defined by the emission of superfluorescence, whose duration is equal to the pump pulse duration (80 ps for our system). To measure the energy of the superfluorescence radiation, the seed signal beam was blocked. The background signal was below the mW level which is the sensitivity threshold of the used detector for 20 Hz repetition rate. Therefore, the energy in the 80 ps superfluorescence pulse was below 50  $\mu$ J. This value has to be compared with the amplified idler signal at the 25 mJ output energy of resulting in 500 mW measured average power. Therefore, the peak intensity of superfluorescence was  $\sim 10^{11}$  W/cm<sup>2</sup>, which is too low to produce any significant amount of plasma before the arrival of the main pulse.

The focus of the experimental campaigns was on X-ray spectroscopy, therefore only X-ray detectors were used as the experimental diagnostics. We have performed high-resolution spectral measurements in the spectral range of 1.65 - 2.1 keV and covering characteristic emission lines from <sup>14</sup>Si from  $K_{\alpha}$  to  $K_{\beta}$  and from all charge states up to H-like Si. This was accomplished by using a KAP crystal spectrometer combined with a cooled back-illuminated X-ray CCD camera. The spectrometer was placed very close to the target and, therefore, decent protection from the background had to be built (see Fig. 5.1). Its orientation with respect to the target differed in the performed experiments (from 20° to 50°). The CCD camera was also located inside the vacuum chamber to avoid significant X-ray attenuation which would occur in the air. Hard X-ray bremsstrahlung spectra in a broad energy range were measured with a Timepix detector [Hahn16] placed in ambient air  $\sim 5$  m away from the target and oriented under  $\sim 45^{\circ}$  to the target normal. The vacuum chamber was pumped below  $10^{-4}$  mbar pressure. All the measurements were conducted in a single-shot



regime.

In this chapter, we present experimental results obtained with targets made of Si or ZnO. Furthermore, we have performed a comparative study of the targets with vertically standing nanowires and polished samples. The Si NWs of about 200 nm in diameter resulted in 35% solid density (average material density), while ZnO NWs being relatively thicker ( $\geq 700$  nm) amount to a  $\sim 43\%$  solid density.

## 5.3 X-ray emission spectra

The spectra of the characteristic line emission from the polished and nanowire ZnO targets irradiated under  $0^\circ$  are shown in Fig. 5.3(a). For both types of the targets, the spectral content (number of lines) is relatively modest – only emission from weakly ionized Zn ( $K_\alpha$  and  $K_\beta$ ) is visible. The signal from the polished sample is fairly low, while the NW target generated a remarkably high  $K_\alpha$  flux. The hard X-ray spectra support the observed enhancement (Fig. 5.3(b)). Exponential fits of the spectra in the range of 30 - 150 keV give  $T_{hot}$  different by a factor of 2, while the photon flux is more than an order of magnitude higher for the nanostructured target. As already observed in Chapter 3, the nanostructured targets only weakly respond to the changing incidence angle between  $0^\circ$  and  $45^\circ$ , unlike the polished samples. The spectra obtained with  $\theta = 0^\circ$  being of no particular interest are not shown here. The integrated flux of the  $K_\alpha$  emission at 8.6 keV as well as the total flux in the range 8.55 - 9.60 keV generated with the investigated targets are given in Table 5.2. At  $\theta = 45^\circ$ , the photon flux in the measured energy range for both sample

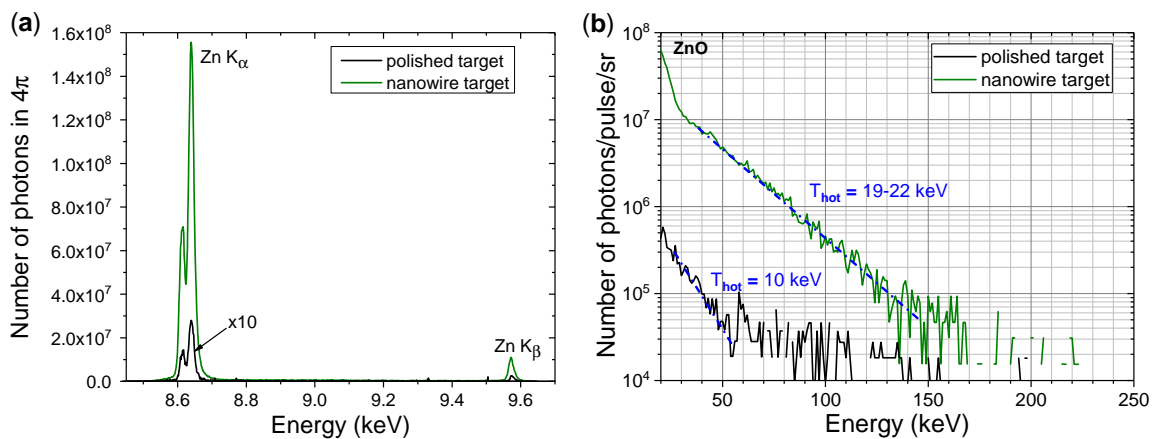


**Fig. 5.3:** (a) Spectra of K-shell line emission from the polished and the nanowire array ZnO targets. (b) Hard X-ray emission spectra with exponential fits. The spectra were measured for a  $0^\circ$  incidence.

morphologies is essentially the same, and the line emission shows the corresponding behavior. It is remarkable that the measured integrated flux of the cold Zn  $K_\alpha$  emission from the NW targets in the normal incidence geometry (Fig. 5.3(a)) is  $3.1 \times 10^9$  photons/pulse, which corresponds to a record high conversion efficiency of  $2.14 \times 10^{-4}$  for several tens of mJ pumping energy. A comparable flux was obtained with a frequency-doubled pulse of JETi-40 laser with an energy of 120 mJ at 400 nm (see Chapter 4).

	$K_\alpha$ flux (photons/pulse)		Total flux (photons/pulse)	
	polished	nanowire	polished	nanowire
Experiment 1: $0^\circ$	$5.4 \times 10^7$	$3.1 \times 10^9$	$6.5 \times 10^7$	$3.5 \times 10^9$
Experiment 2: $45^\circ$	$7.1 \times 10^8$	$6.9 \times 10^8$	$7.8 \times 10^9$	$6.9 \times 10^9$

**Tab. 5.2:** The integrated X-ray flux obtained with ZnO targets in different incidence geometry. Total flux is calculated for the K-shell emission.

The K-shell emission spectra generated under our experimental conditions contain line emission only from weakly ionized Zn ( $Zn^+ - Zn^{20+}$ ) overlapping with each other. Therefore, it cannot be easily used for diagnostics of the plasma parameters. Whether all the mentioned charge states really contribute to the cold emission, one cannot determine. Surely, there are methods which allow retrieving such information from the broadening and the blue shift of the  $K_\alpha$  line [Neumayer09; Zastrau10a], however, the resolution of our crystal spectrometer and the precision of the calibration make it impossible to use those techniques. Lower-Z target materials irradiated by a weakly relativistic mid-IR laser pulse provide more informative emission spectra.

Indeed, the characteristic spectra from Si targets are richer than the ones from ZnO targets (Fig. 5.4). At  $\theta = 45^\circ$ , the  $K_\alpha$  emission from the weakly ionized Si ( $Si^+ - Si^{4+}$ ) is approximately the same for both polished and nanowire samples. This tendency was observed in all our experiments and suggests that in the relativistic limit nanostructured arrays are not profoundly beneficial for the cold line emission in comparison to the flat surfaces. However, the intensity of the emission lines generated via transitions in highly ionized states from nanowire targets dramatically rises. Emission from Li-like ( $Si^{11+}$ ), He-like ( $Si^{12+}$ ) and H-like ( $Si^{13+}$ ) ions, such as  $He_\alpha$ ,  $He_\beta$  and  $Ly_\alpha$  lines, is detected from the nanowire arrays only. This implies that the plasma conditions created in these two cases (nanowire and polished targets) might be quite different. It should be noted that  $K_\beta$  line spectrally overlaps with

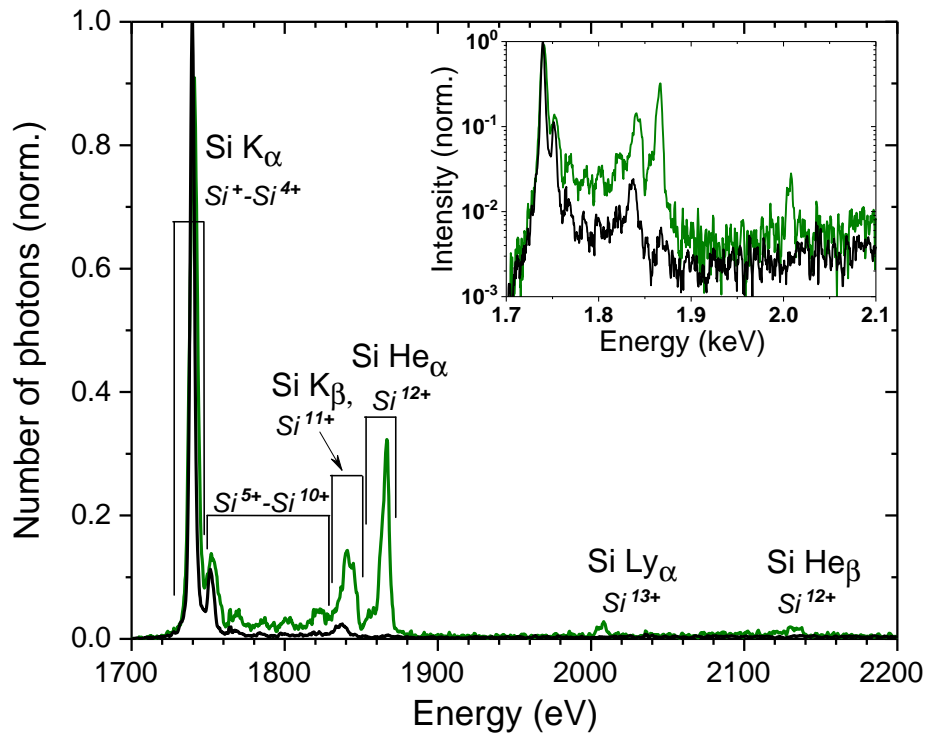


**Fig. 5.4:** Spectra of K-shell line emission from the polished (black line) and the nanowire array (green line) Si targets. *Inset:* The same spectra in logarithmic scale.

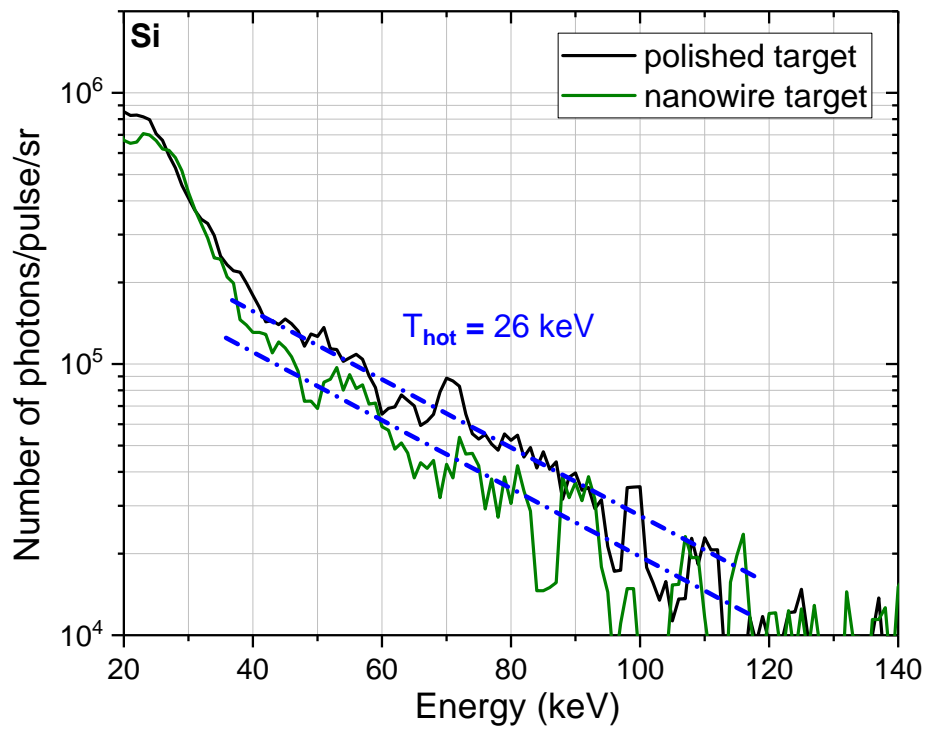


**Fig. 5.5:** Hard X-ray emission spectra with an exponential fit corresponding to the hot electron temperature  $T_{hot}$  of  $\sim 26$  keV.

K-shell emission from  $\text{Si}^{11+}$  ions, though their center of mass and peaks are slightly shifted with respect to each other. To identify which lines are present in the spectra it is worth to turn to the known line ratios. The intensity ratio of  $K_\beta$  to  $K_\alpha$  in cold Si is about 1:50, though this value differs from one reference source to another [X-rayDataBooklet; Khan80]. For the polished sample the measured ratio of 1:42 (inset Fig. 5.4) matches well to the mentioned values. However, the corresponding ratio for the nanowire target of 1:6 proves the dominant contribution of the emission from Li-like Si in the spectral range 1.83 - 1.85 keV.

The bremsstrahlung spectra, similarly to the results obtained for the K-shell emission, demonstrate almost no difference in the flux up to 140 keV (Fig. 5.5). The exponential fit gives for both morphologies of the targets “hot” electron temperature  $T_{hot} = 26$  keV. The fitting is done for the photons with energies 40 - 140 keV. We suppose that the corresponding fraction of electrons is heated during the laser pulse via the Brunel mechanism. This suggestion agrees with the theoretical modeling of the hard X-ray generation recently reported [Weisshaupt15].

The experimental results obtained with low- and mid-Z materials demonstrate that under our experimental conditions, Si samples are more suitable for plasma diagnostics using spectroscopic methods and simulations. Moreover, the Si nanostructured targets irradiated by the mid-IR laser pulses exploit the potential of such a driver to generate extreme states of matter. The difference seen for the used target materials can be explained by the ionization theory. According to the optical field ionization calculations based on Popov-Perelomov-Terentiev (PPT) ionization model [Perelomov66], the laser pulse strips Si atoms up to  $\text{Si}^{3+}$  -  $\text{Si}^{4+}$ . Higher charged states, if observed, are created due to the electron impact ionization. The ionization potential of He-like Si is about 2.44 keV [NIST]. For ZnO targets the situation is different – the laser field is capable to remove only 8 electrons which results in  $\text{Zn}^{8+}$  ions. Further, the energy deposited in the target material is spent on collisional heating. However, it seems that the reached ionization state (must be  $\leq \text{Zn}^{20+}$ ) was not high enough to result in radiative transitions which we can resolve in the measured K-shell emission spectrum. Indeed, the ionization potential of  $\text{Zn}^{21+}$  is about 2 keV and of  $\text{Zn}^{28+}$  (He-like Zn) is almost 12 keV [NIST]. Taking into account that the absorption of the laser energy for Si and ZnO NW targets can differ, we may state a good correlation between the experimental data and the given interpretation.

## 5.4 Simulations of the plasma parameters

In order to retrieve the plasma parameters from the measured data and gain an understanding of the processes at different time scales, we carried out two sets of numerical simulations for Si targets. First, we performed particle-in-cell (PIC) simulations using the Virtual Laser Lab code [Pukhov99] to determine the parameters of the plasma and their dynamics under the conditions close to the experimental ones. To simulate an array of nanowires, this 3D PIC code considers a 200 nm-thick cylindrical Si nanowire with a length of 6  $\mu\text{m}$  in a simulation box with periodic boundary conditions in the transverse direction. A plane wave with a Gaussian envelope in the longitudinal direction (90 fs,  $I = 10^{17}$  W/cm<sup>2</sup>) enters the box and propagates toward the NWs, normal to the target surface. From the results of these simulations, the temporal evolution of the bulk and hot electron temperature as well as electron density at a chosen region of the target can be retrieved. In the second step, the obtained data were used as input in simulations performed with the FLYCHK atomic kinetic code [Chung05] in order to synthesize line emission spectra.

The snapshots of the bulk electron temperature at different moments of time calculated with the PIC code nicely demonstrate the spatial distribution of the electron temperature along the NWs (Fig. 5.6(a)). Time zero corresponds to the moment when the maximum of the laser pulse reaches the tip of NW. The bulk electron temperature  $T_{bulk}$  rises up to 600 eV within  $\approx 1$   $\mu\text{m}$  thick layer at the tip of the NWs during the interaction with the laser pulse. 300 fs after the arrival of the laser peak intensity the entire NW volume is heated almost homogeneously to  $\approx 50$  eV and then rapidly cools down. The spatial distribution of the electron density in the wire volume is shown in Fig. 5.6(b). Within the 1  $\mu\text{m}$ -thick hot upper layer of the NWs on the time scale of the laser pulse duration the electron density  $n_e$  reaches a maximum value of  $\sim 6 \times 10^{23}$  cm<sup>-3</sup>, corresponding to every atom being ionized up to Si<sup>12+</sup> (He-like). After the laser pulse (at 1 ps) the significant part of the volume of the NWs is ionized with electron density  $\sim 3 \times 10^{23}$  cm<sup>-3</sup> and thermalizes to an electron temperature of about 30 eV. Taking into account the value of the critical density  $n_{cr} \approx 7.3 \times 10^{19}$  cm<sup>-3</sup> for a laser wavelength of 3.9  $\mu\text{m}$ , the simulations suggest that the plasma as dense as  $\approx 10^4 n_{cr}$  is generated under the conditions of the experiment. Our simulations show also that the wires stay intact and high plasma density is maintained on the time scale of at least 2 ps. This can be attributed to

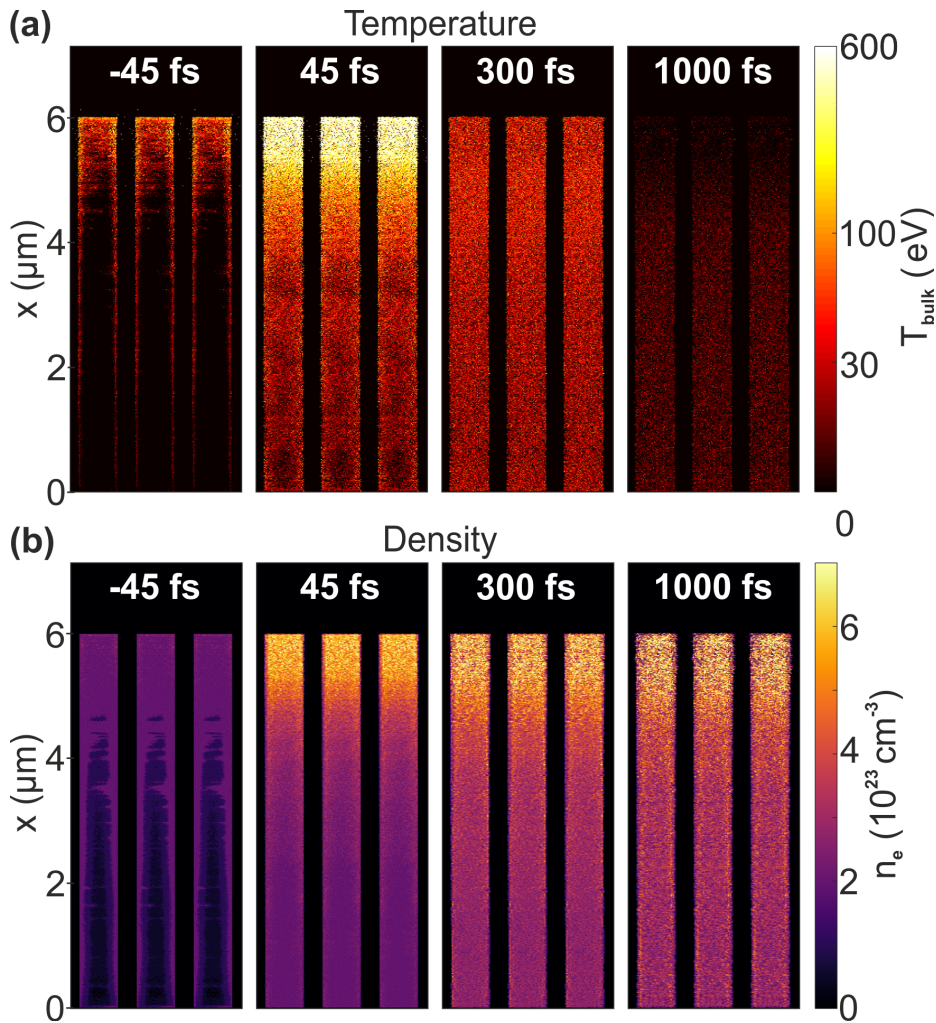


**Fig. 5.6:** The results of PIC simulations for the spatial distribution of (a) the bulk electron temperature  $T_{bulk}$  and  $n_e$  (b) electron density for the Si NW target. The time is given with respect to the arrival of the laser peak intensity at the NW tips.

a relatively low amplitude of the magnetic field in the pulse. As a result, there is no electron current driven by the relativistically intense laser pulse along the wire and, thus, no pinching occurs. Such a pinch effect could additionally increase the electron density but at the same time trigger a very fast expansion of the NWs at femtosecond time scale.

The highest temperature and density plasma is localized within roughly  $1 \mu\text{m}$  of the top part of the NWs corresponding to the penetration depth of the laser pulse into the structure, which is determined by the efficiency of the absorption. The PIC simulations predict that 76% of the laser pulse energy (20 mJ in the given case) are absorbed within the Si NW target and mainly deposited within a  $1 \mu\text{m}$ -thick layer. The absorption efficiency is limited due to the notably high  $n_e/n_{cr}$  ratio and the target geometry. In these series of the experiments, we have not studied NW

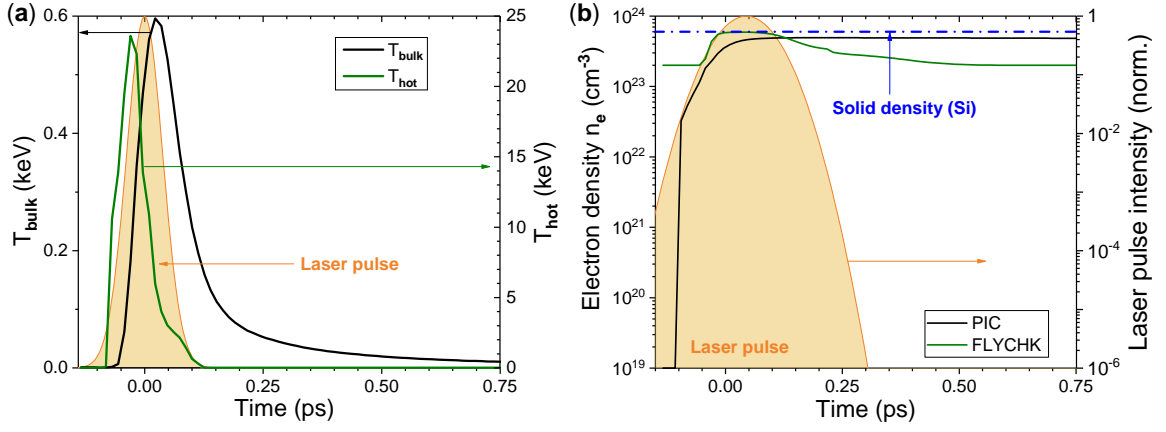


**Fig. 5.7:** (a) The temporal evolution of the bulk and hot electron temperatures ( $T_{bulk}$  and  $T_{hot}$ ) of the electron fractions averaged over the upper 0.5  $\mu\text{m}$  of the NW. (b) The temporal evolution of the electron density  $n_e$  calculated by PIC and FLYCHK simulations (in logarithmic scale).

targets with diverse parameters. Additional simulations of a flat target have shown a significantly reduced laser energy absorption (presented later).

The bulk and hot electron temperatures,  $T_{bulk}$  and  $T_{hot}$ , retrieved from the PIC simulations and averaged over the top 0.5  $\mu\text{m}$  of the NW were directly implemented (Fig. 5.7(a)). The hot electron temperature reaches a maximum of about 20 keV within the laser pulse duration and vanishes as soon as the laser pulse ceased. The calculated maximum value is in a good agreement with the hot electron temperature estimated from the measured hard X-ray spectra (see Fig. 5.5).  $T_{bulk}$  reaches its maximum value  $\approx 0.6$  keV by the end of the laser pulse and cools down within 100 - 200 fs. However, the results for the electron density  $n_e$  should be treated with caution. It might seem surprising that the NWs keep their shape and do not hydrodynamically expand in the absence of any pinching effect in our case. That said, this could be explained by the rapidly decreasing temperature of the vast of the electrons due to the radiative losses. On the other hand, the PIC code does not account for the recombination processes in the plasma, which give the main contribution to the drop of the electron density. In a next step, the time evolution of the plasma parameters calculated by the PIC code was used as the input parameters for FLYCHK simulations, which provide then evolution of the charge states, populations of different excited ion states and resulting emission spectra. For FLYCHK we assumed an ion density of  $5 \times 10^{22} \text{ cm}^{-3}$  kept constant over the simulation time of 1.5 ps, while the electron density was calculated by the code itself. It is also worth mentioning also that the temporal evolution of the electron density during the laser pulse, calculated by the FLYCHK code, agrees well with the evolution of the

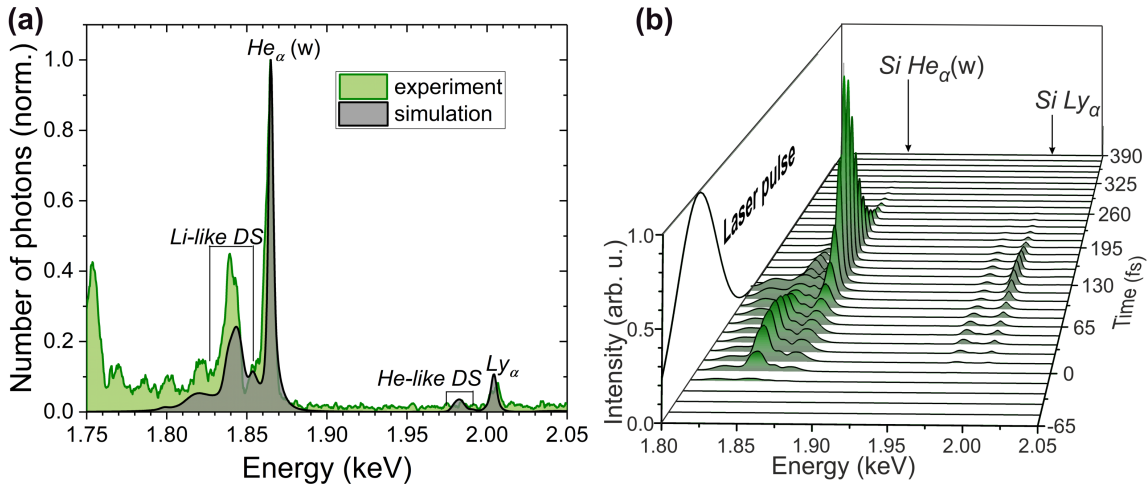


**Fig. 5.8:** (a) The measured and simulated X-ray spectra (time-integrated) for Si NW target. (b) The temporal evolution of the K-shell emission in the spectral region 1.80 - 2.05 keV calculated in FLYCHK.

electron density in the PIC simulations averaged over the upper  $0.5 \mu\text{m}$  (Fig. 5.7(b)). The effect of the efficient recombination is revealed by the 2-fold decrease of the electron density after the laser pulse predicted by FLYCHK.

The large volume of the dense plasma predicted by the PIC simulations results in a large wavelength-dependent plasma opacity. The inclusion of this effect in the simulation of the emission spectrum is of great importance because it causes strong reabsorption of the generated emission and thus influences the emission line ratio. Therefore, we chose the effective thickness of the plasma layer as a fitting parameter to match the simulated spectra to the measured ones. Here, the effective thickness refers to the mean depth, at which the emission was generated. The best fit between the simulated and experimental X-ray line spectra is found for a top plasma layer of about  $0.5 \mu\text{m}$  (Fig. 5.8(a)). Since the generated plasma is multilayered and the detected emission is integrated in space and time, we intended to reconstruct only the most energetic part of the spectrum, consisting of He- and H-like Si emission lines and emitted at the maximum intensity region in the focal distribution. The simulated emission spectrum demonstrates an excellent agreement in this spectral region. The FLYCHK simulations were performed in transient mode and the final spectrum in Fig. 5.8(a) is a sum of the spectra generated over the whole plasma evolution in the range 1.80 - 2.05 keV (Fig. 5.8(b)).

The FLYCHK simulations provide insights into the atomic processes in plasmas helping to understand the temporal structure of the emitted X-ray radiation. In particular, we extracted the temporal evolution of the charge states and the emitted



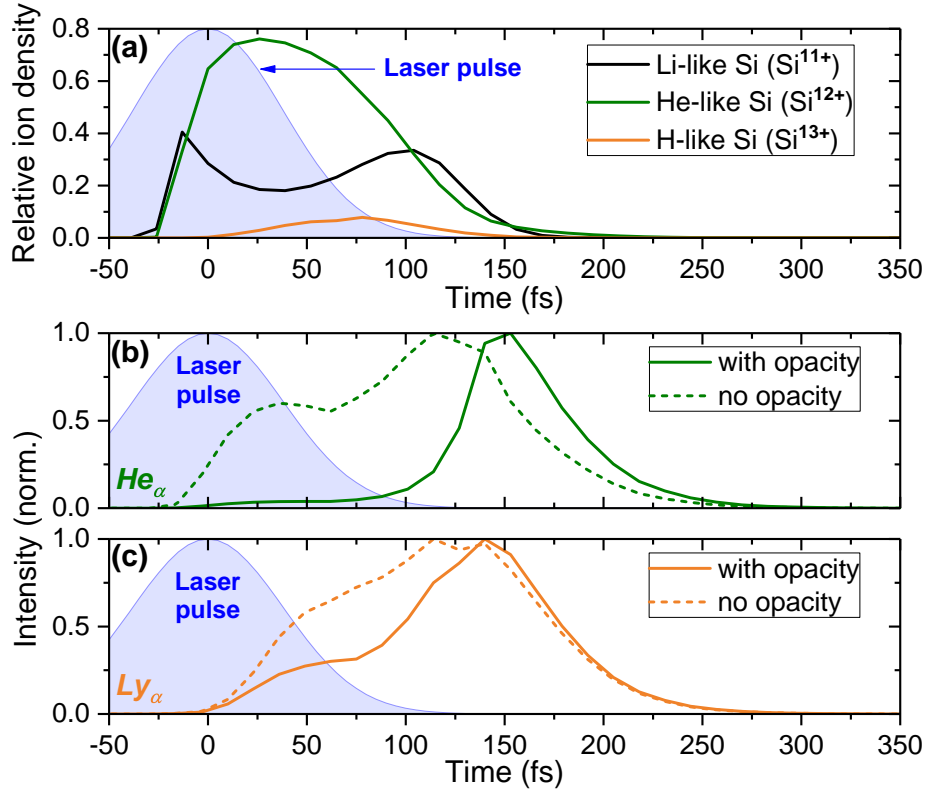


**Fig. 5.9:** (a) The temporal evolution of the relative ion density ( $\text{Si}^{11+}$ ,  $\text{Si}^{12+}$ ,  $\text{Si}^{13+}$ ) calculated by FLYCHK. The temporal evolution of the intensity of  $\text{He}_\alpha$  (b) and  $\text{Ly}_\alpha$  (c) emission lines with/without opacity included.

spectrum (Fig. 5.9), which are governed by the changes of the bulk electron temperature, and collisional and radiative rates. We consider only the behavior of the highest achieved charge states – He-like and H-like Si ions. The formation of  $\text{Si}^{12+}$  and  $\text{Si}^{13+}$  occurs mostly as a result of the collisional ionization of  $\text{Si}^{11+}$  and  $\text{Si}^{12+}$ , respectively. The generation of  $\text{Si}^{12+}$  also happens via recombination channel. Ionization of the L-shell up to the charge state  $\text{Si}^{12+}$  takes place at about 25 fs after the peak of the laser pulse intensity (at the rising edge of the bulk electron temperature, Fig. 5.9(a)). However, the threshold for further ionization can be considered as a bottleneck, since ionization of the K-shell requires electrons with a kinetic energy of more than 2 keV (compared to 100-150 eV for the L-shell). Note that the rates of the collisional processes in plasma drop exponentially with an increasing ratio of the binding energy  $E_{bin}$  to the bulk electron temperature  $T_{bulk}$ . Therefore,  $\text{Si}^{13+}$  ions are generated with a delay with respect to the appearance of  $\text{Si}^{12+}$  and approach their highest density at roughly 75 fs (Fig. 5.9(a)). After reaching their maxima, both ion species decrease in number and there is no further ionization, while  $T_{bulk}$  rapidly drops. The second peak of the  $\text{Si}^{11+}$  density is a result of the recombination

in the cooling plasma. Supplementary steady-state FLYCHK simulations at  $T_{bulk} \approx 600$  eV give a different ion fraction distribution. The maximal fraction of  $\text{Si}^{13+}$  (8%) calculated by the time-dependent FLYCHK simulations is one order of magnitude lower than for the steady-state, while the fraction of  $\text{Si}^{12+}$  is 2 times higher (80% instead of 40%). Such a difference manifests a transient character of the plasma produced under our experimental conditions and excludes the possibility to use simple steady-state simulations with no time dependence included (in contrast to the results in Section 4.1).

The collisional excitation of the K-shell electrons followed by the radiative decay back into the ground state produces the K-shell line emission ( $\text{He}_\alpha$  and  $\text{Ly}_\alpha$ ). The time scale of the build-up of the ion density and the time scale of the electron impact excitation for both  $\text{Si}^{12+}$  and  $\text{Si}^{13+}$  charge states are similar. Therefore, the  $\text{He}_\alpha$  and  $\text{Ly}_\alpha$  line emission appear almost simultaneously to the corresponding ion density. In accordance with the radiative decay times [Chung05], the maximum of the emission intensity is delayed by  $\sim 25$  fs for  $\text{He}_\alpha$  and  $\sim 50$  fs for  $\text{Ly}_\alpha$  with respect to the maximum of the corresponding ion density if we neglect the opacity (Fig. 5.9(b,c)). However, the  $\text{He}_\alpha$  line resembles a double structure, where the second maximum in the emission is related to the recombination channel of the population of the H-like ions. The time-dependent opacity not only reduces the intensity of the outgoing radiation but strongly modifies the temporal profile of the line emission. While plasma stays hot, the radiation is trapped in the plasma volume being strongly reabsorbed and scattered. As a consequence, we observe a delay of the maxima of  $\text{He}_\alpha$  and  $\text{Ly}_\alpha$  emission and a shortening of the effective emission time: a pulse of  $\sim 50$  fs (FWHM) at 1.865 keV ( $\text{He}_\alpha$ ) and a pulse of  $\sim 150$  fs at 2 keV ( $\text{Ly}_\alpha$ ) (Fig. 5.9(b,c)). The expected shorter duration of the  $\text{He}_\alpha$  emission is an effect of higher opacity of the plasma at this emission wavelength. Overall, the ultrashort duration of the generated X-ray emission in the relativistic interaction of ultra-high contrast, ultra-short laser pulses with solids is inherently related to the transient character of high-density plasmas. This transient nature of the plasma evolution has to be taken into consideration when estimating the time scale of radiative cooling processes and determining conditions for new regimes where the plasma cooling caused by plasma self-radiation proceeds faster than hydrodynamic expansion [Hollinger17a]. A high electron density enables ultrafast collisional pumping. Meanwhile, a high ion density (of the corresponding charge state) leads to strong absorption of the emitted line radiation (opacity) and the re-emission of the absorbed photons is heav-

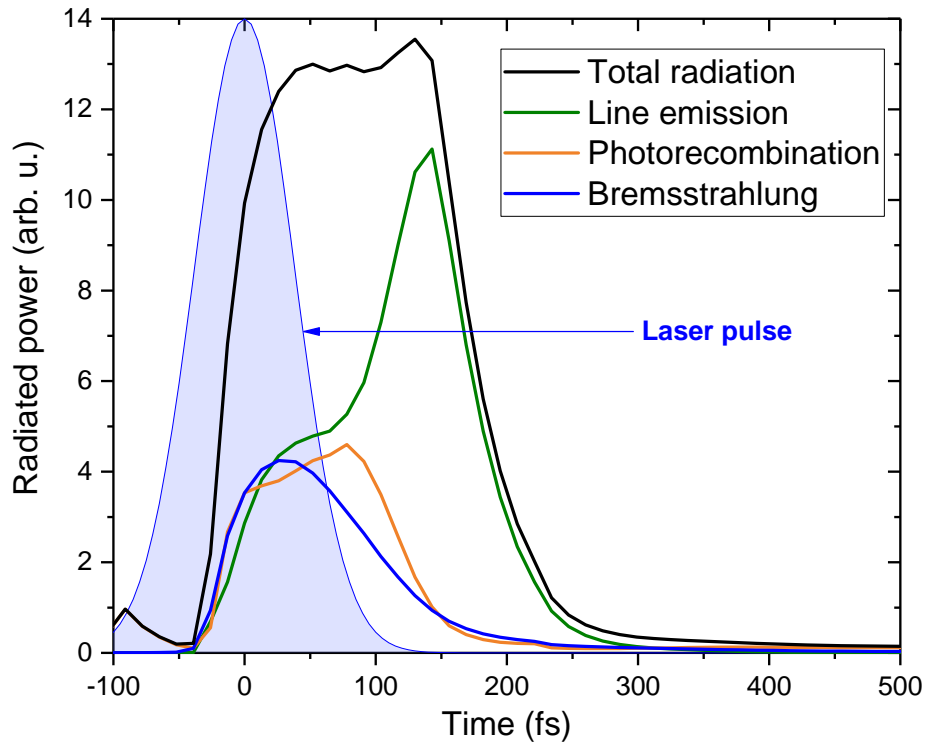


**Fig. 5.10:** The time evolution of the radiated power (losses) for the hottest and densest region of Si NW target (top 0.5  $\mu\text{m}$ -thick layer) calculated with FLYCHK.

ily suppressed due to the collisional de-excitation by free electrons. Thus, a delay between the maximum of the laser pulse and the maximum of the K-shell radiation is expected as it is demonstrated in Fig. 5.9(b,c). The time-dependent radiative losses in the simulated volume (upper 0.5  $\mu\text{m}$  of the NW target) are illustrated in Fig. 5.10. In contrast to the picosecond duration estimated from assumptions of an optically thin plasma under steady-state conditions [Hollinger17a], we conclude that the dynamically changing at a sub-picosecond time scale the high temperature and the density of the plasma in interplay with opacity effects are determining the femtosecond duration of the line X-ray emission.

Finally, in order to understand the observed differences in the emission for the different targets morphologies, we attempted to perform simulations for the spectrum measured from a polished Si sample. The 3D PIC simulations used for the Si NWs failed to converge for a reasonable set of numerical parameters. The primary cause of the difficulties is the very high (in critical density units) density of plasma requiring a high resolution (the interaction is expected to happen at a very thin skin layer). Besides that, for a polished sample, it is important to account for a  $45^\circ$  incidence angle and introduce a Gaussian profile of the incoming laser pulse. Therefore, the simulations were carried out in two dimensions. The results of the

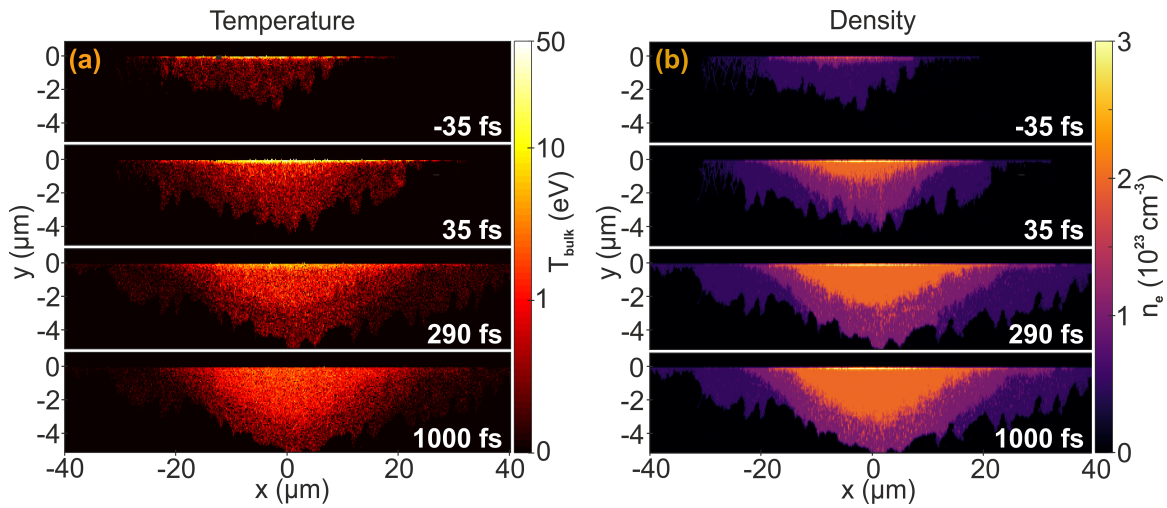


**Fig. 5.11:** The results of PIC simulations for the spatial distribution of (a) the bulk electron temperature  $T_{bulk}$  and (b) electron density  $n_e$  for the polished Si target. The zero moment of time corresponds to the moment of the peak intensity arrival at the surface boundary.

spatial and temporal evolution of the bulk electron temperature and density are presented in Fig. 5.11. As can be seen from Fig. 5.11(b), the plasma density  $n_e$  for flat targets can be as high as  $3 \times 10^{19} \text{ cm}^{-3}$  which is just a factor of 2 smaller than the electron density calculated for NWs (Fig. 5.7(b)). This density would correspond to a volume fully ionized to  $\text{Si}^{6+}$ . However, the maximum bulk electron temperature  $T_{bulk}$  is only 50 eV and reached just within a  $\sim 100 \text{ nm}$ -thin layer near the surface. The densest plasma is also localized in this small volume. Compared to nanowires, for which the predicted bulk electron temperature rises up to 600 eV, the significantly lower temperature can be explained by a very weak laser energy absorption (2%). Unfortunately, for such dense and low-temperature plasma conditions, FLYCHK is unable to simulate the spectrum. However, it is clear that the experimentally observed line emission can be generated in a relatively cold matter only (Fig. 5.4). The observed spectrum can be understood by applying the concept of Brunel electron heating [Brunel87] extending into the relativistic regime [Weisshaupt15]. With this mechanism, electrons are efficiently accelerated near the critical density and the subsequent collision creates holes in the K-shell of neutral Si atoms and weakly ionized Si ions which leads to cold  $K_\alpha$  emission.

Although the synthesis of matching spectra covering the whole range of K-shell emission measured in the experiments is not of interest for this study, it is worth to discuss the nature of this emission. Presumably, the weak emission in the range of 1.747 - 1.827 keV (Fig. 5.4 (inset)), observed for all the targets and originating from the Si ions up to  $\text{Si}^{10+}$ , is generated due to inner-shell collisional ionization

by energetic electrons emerging from the Brunel heating process. Therefore, in contrast to the emission from highly charged Si ions that appears with a delay to the maximum of the laser pulse intensity, the radiation of the low/intermediately charged Si ions exist only around the intensity peak so long as the hot electrons are present. Almost one order of magnitude difference in the yield of this emission between the nanowires and the bulk target originates from the difference in the bulk electron temperature and its spatial distribution (in depth and breadth).

## 5.5 Discussions

Our research presents new aspects of the interaction of relativistically intense, high temporal contrast, mid-IR femtosecond laser pulses with solids. This very first comparative study of the X-ray emission generated from polished and nanostructured solid surfaces within a novel regime emphasizes the advantages of a long-wavelength driver. In this regime, the laser field ionization and the pre-plasma formation on the rising edge of the laser pulse, always revealing itself in experiments with relativistic UV-visible-near-IR laser pulses, are strongly suppressed. As a consequence, the peak of the laser pulse interacts with solid matter and the ionization has predominantly collisional character.

One of the more significant findings emerging from this study is that, despite a very low critical electron density, the high electron density plasma can be created (up to  $6 \times 10^{23} \text{ cm}^{-3} \approx 10^4 n_{cr}$ ). It is shown that under our experimental conditions the NW array morphology enables dramatic enhancement of the efficiency of the characteristic line emission from highly charged states, whereas it does not influence the efficiency of the  $K_\alpha$  line emission from the cold material (demonstrated with ZnO and Si targets). In particular, the K-shell emission from He- and H-like Si was only detected from Si NW arrays as a target. The transient character of the plasma means that K-shell ionization and electronic excitation processes occur on a femtosecond time scale of the laser pulse and sub-picosecond time scale of free plasma cooling after the pulse, respectively. Therefore, the observed spectra can be explained only by high density and temperature of the generated plasma. Indeed, it was inferred from the simulations, which are in very good agreement with the experimental data, that an electron density for Si NW arrays approached  $6 \times 10^{23} \text{ cm}^{-3}$ . The electron density of the plasma generated from the polished Si target is just slightly smaller than the density retrieved for the nanowires. However, there is a striking difference

(an order of magnitude) in the bulk electron temperatures. This can be interpreted as a result of the morphology dependence of the laser energy absorption in the plasma (76% for the NW and 2% for the polished samples). Taken together, the obtained results show that nanowire morphology of the target is crucial for reaching high temperatures in extremely dense plasmas generated by mid-IR pulses.

An absence of the pinching effect under moderate intensities but yet relativistic mid-infrared pulses explains an unprecedentedly long lifetime of overdense plasma predicted under the condition of our experiment. We assume that there is an energy window for a mid-infrared laser pulse within which plasmas created with NW targets can be heated up to keV temperatures and remain at solid density.

The generated plasma emits ultrashort X-ray pulses ( $\leq 150$  fs) at Si He $_{\alpha}$  (1.865 keV) and Si Ly $_{\alpha}$  (2.006 keV) as indicated by the FLYCHK simulations. In fact, the high electron density of the plasmas ensures high collision rates that govern ionization and excitation of atoms and ions, which then result into an ultrashort pulse duration of the emitted radiation as observed with the short-wavelength driver (Chapter 4). We believe that such pulses are very attractive for time-resolved X-ray radiography of high-density plasmas. Moreover, solid density plasmas with keV-level bulk temperatures produced with NW targets and mid-IR laser pulses are very promising for applications in laser-driven nuclear physics [Gunst14; Gunst15]. Our results provide not only new fundamental knowledge but also a stimulus for the development of a new type of X-ray sources based on an interaction of the relativistically intense long-wavelength drivers with nanostructured targets. More broadly, research is also needed to determine further possibilities which femtosecond mid-infrared laser sources could offer. Apart from the X-rays generation, one may think of investigating other secondary radiation generated in this experimental scheme.

## Summary & Perspectives

The aim of this thesis was to investigate the influence of nanowire arrays on the properties of laser-induced plasmas. The performed experiments and simulations highlight the unique features of plasmas enabled with this specific target morphology. Our study also provides considerable new insight into the relativistic laser-matter interaction with flat solids at a high pulse contrast. Since up to now there are almost no thorough investigations of plasmas under these conditions, it was especially important to conduct comparative studies for different morphologies.

The main advantage of nanowires compared to polished targets is a *substantially enhanced absorption* of the incident laser pulse energy. This energy is then spent on electron heating leading to substantial collisional ionization. A strong enhancement of the X-ray emission (from highly charged ion states) serves as a benchmark of a high laser energy absorption (Chapter 4 and Chapter 5). This advantage becomes especially feasible when the critical density  $n_{cr}$  is low like in the case of mid-infrared laser pulses. In Chapter 5 it was pointed out that NW morphology allows to exploit the full potential of a long-wavelength driver and use all the provided benefits. With just 20 mJ energy at 3.9  $\mu\text{m}$  we were able to generate plasmas with an electron density of  $\approx 8000n_{cr}$  and bulk electron temperature of 0.6 keV using Si NW targets. We suggest that the primary *absorption mechanism* is Brunel mechanism. This conclusion has been done based on the polarization dependence of the X-ray flux for different target morphologies (Chapter 3). The experimental observations support a suggestion that the large surface area of NWs is one of the key points for effective laser energy absorption.

Another essential difference is related to the size of the *activated volume* and efficient *volumetric heating*. Our experimental results have demonstrated that the NW targets produce stronger line emission originating from the regions of the hottest and densest plasma. The simulations support this finding suggesting that the NWs were heated up within a top layer exceeding 0.5  $\mu\text{m}$ , while with flat targets only a very thin layer (<150 nm) of hot and dense plasmas was produced. Nevertheless, it was clearly shown that keV hot solid-density plasmas can be also produced without any

target surface modification. However, it seems that in the case of the NW targets we may expect further growth of the plasma volume with growing laser intensity, while for flat targets the penetration depth is strictly limited. Though such a trend has been observed for X-ray emission (line and continuum) and ion generation, it should be treated with the utmost caution until additional measurements/simulations are done.

Naturally, *X-ray spectra* contain a wealth of information about the plasma evolution, which can be challenging to retrieve. One of our approaches is based on *simulations of X-ray spectra* with data calculated by the PIC code. It enabled us to retrieve plasma parameters such as electron temperature, electron density, ion charge distribution, etc. Plasmas generated by intense femtosecond pulses have a transient character, meaning that the time-dependence of their parameters must be taken into account. Thanks to the PIC simulations it was possible to incorporate fast plasma dynamics into the spectral simulations. First successful results were presented in Chapter 4 and Chapter 5.

The *plasma kinetics* taking place for the NW targets is completely different. If in the case of a flat surface a 2D expansion of plasmas and perhaps shock wave compression are expected, the geometry of the NWs implies a more complicated picture. The NWs irradiated by an intense laser pulse may preferably expand in the lateral plane filling the gaps between the NWs with overcritical plasmas. The velocity of expansion (acoustic speed) depends on the temperature of the electrons and ions as well as their charge-to-mass ratio. However, depending on the strength of the applied laser field, a strong return current running along the NW can induce a magnetic field able to keep the NW together or even compress its volume. This effect called pinch effect [Kaymak16] was not observed in the simulations for the interaction with a long-wavelength driver but may have occurred with a short-wavelength driver (experiments at JETi-40).

We have observed an increase in the *ion flux* produced within the relativistic interaction. With the NW targets, the cut-off energies, as well as the number of energetic ions, were significantly higher than with the polished samples. We concluded that the ions were accelerated due to the thermal expansion. The ion spectra for all targets were dominated by low-charge ions. This interesting observation has been specifically discussed and attributed to the charge transfer and neutralization of the ions in expanding plasmas.

The fact that the pointed out trends were observed for all investigated materials



and with different laser systems speaks for its generality. In the experiments where complex diagnostics setup was used, the results were consistent with each. This makes us confident about our findings. In summary, our study has enhanced our understanding of the role of a nanowire morphology in the generation of extreme states of matter.

## **Outlook**

Surely, the already obtained data may provide further insights into physics involved in relativistic interactions of ultra-short laser pulses with solids. Further analysis of the X-ray spectra requiring line profile simulations and addition PIC simulations is ongoing.

Despite considerable progress, there are still a lot of open questions. One of them is related to the parameters of the NW arrays. With which NW it is possible to heat the volume more effectively, depends on the laser pulse. A NW should be long enough to absorb maximum energy, but short enough to let the generated emission out. Long NWs are not necessarily better. It is clear that the diameters of NWs should be smaller than the wavelength of the laser pulse to be seen as structures (not flat). At the same time, if the radius of the NWs smaller or comparable with the skin depth, the interaction is possible with the whole NW at once. The spacing between the NWs is another parameter to consider. In our future experiments, we would like to explore how sensitive for NW array dimensions the plasma parameters are. For such a study it makes sense to use the NW targets with well-defined periodic structure.

Although we have witnessed that the efficiency of the laser energy absorption is significantly higher for the NW targets, there were no direct measurements of the absorption performed. Yet it can be even more crucial to answer the question where the absorbed energy goes or how it is spent. This is a vital step for future research which may help to explain the observed phenomena and verify the simulation results. Further experiments on the absorption of high-intensity laser pulses are scheduled for the next beam time.

The pulse contrast is a crucial issue in the experiments with nanostructured targets. To use the benefits of the morphology one needs a clean pulse with high contrast. However, quantifying a good temporal contrast is not a simple task. To address this question we plan to perform an experiment with NW targets using a controllable pre-pulse (delay and intensity).

The encouraging results obtained with a long-wavelength driver serve as a stimulus to proceed with further studies. With higher energies and complex diagnostics, we might be able to move further towards the development of a compact source of ultra-hot and dense plasmas. We believe that this novel regime has a lot to offer for the field of HED physics.

# Appendices

## A Few-electron ions: transitions

Few-electron ions, particularly helium- and hydrogen-like ions, provide an important ground for the X-ray spectroscopy. Such systems are relatively simple, therefore the simulation of the atomic process for them can be rather accurate. But already three-electron and more-electron systems become very challenging to simulate, thus the accuracy of results drops.

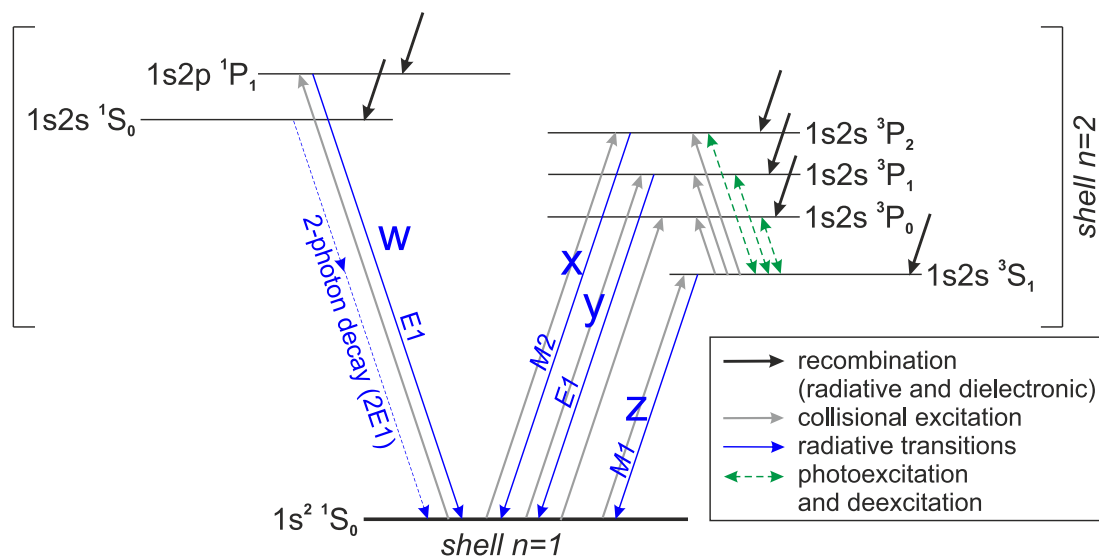


**Fig. A.1:** Simplified level diagram of fine-structure states of He-like ions.

In this Appendix, we illustrate the radiative and non-radiate transitions in He-like ions using a simplified energy level diagram (Fig. A.1). In the X-ray range, the He-like triplet has three energetically close emission lines: the resonance line (denoted  $w$ ), the intercombination lines ( $x$  &  $y$ ) and the forbidden line ( $z$ ). All of them correspond to the transitions between the  $n = 2$  shell and ground state ( $n = 1$  shell). The resonance line is the strongest line and arises from a transition  $1s2p \ ^1P_1 \rightarrow 1s^2 \ ^1S_0$ . The intercombination line  $y$  is also a electric-dipole (E1) transition:  $1s2p \ ^3P_1 \rightarrow 1s^2 \ ^1S_0$ , while the other line  $x$  ( $1s2p \ ^3P_2 \rightarrow 1s^2 \ ^1S_0$ ) is a magnetic-dipole transition (M1). The intensities of these lines are sensitive on electron temperature and density in a different manner. The radiative times of the 4 levels ( $^1P$ ,  $^3P$ ,  $^1S$ ,  $^3S$ ) are quite different but depend on  $n_e$ . The upper levels of  $x$ ,  $y$ ,  $z$  transitions are metastable. Since the emission line intensities are proportional to the population of the upper levels and the decay rates. These lines can be

well pronounced in a spectrum of a low-density plasma (Corona model) while the corresponding upper levels are vastly populated. An increase in electron density causes a collisional depletion of the metastable levels (e.g.,  $1s2p\ ^3S_1$ ), decreasing the intensity of the forbidden transition. The collisional excitation rates do not behave the same way with a changing electron temperature for the resonance line as for the intercombination and forbidden lines. Thus, a weak resonance line manifests a plasma dominated by photoionization, and otherwise - a collision-dominated plasma. More details regarding temperature and density diagnostics can be found in [Ralchenko16; Porquet10]. Besides that, the self-absorption/opacity of He-like triplet also strongly influences the observed emission spectra. While the resonant line, in general, has a significant optical depth  $\tau$  for the line absorption, the forbidden and intercombination lines have a small  $\tau$ .

Typically, real X-ray spectra of warm/hot dense plasmas accumulate information about the whole plasma evolution, i.e. emission lines originating from plasmas of different temperatures and densities. To probe warm/dense hot matter only "the hottest" part of the spectrum is used - emission line of few-electron ions. The discussed above lines are partially or fully merge with corresponding dielectronic satellites (e.g., Li-like) depending on the element. The dielectronic satellites on the red side of the line result into an asymmetric broadening in low-resolution spectrometers. In this case, an accurate spectral analysis is hardly possible. The role of the dielectronic satellites in the experimental spectra has been widely studied by a number of groups [Rosmej98; Schollmeier06; Wang17].

## K-shell emission lines<sup>1</sup>

Zn (Z = 30)		Ti (Z = 22)	
Line	Energy (eV)	Line	Energy (eV)
K <sub>α2</sub>	8615.78	K <sub>α2</sub>	4504.86
K <sub>α1</sub>	8628.86	K <sub>α1</sub>	4510.84
K <sub>β</sub>	9572.00	K <sub>β</sub>	4931.81
He <sub>α</sub> (y)	8949.78	He <sub>α</sub> (y)	4727.00
He <sub>α</sub> (w)	8998.73	He <sub>α</sub> (w)	4749.70
Ly <sub>α</sub> 2p <sub>1/2</sub>	9280.83	He <sub>β</sub>	4872.91
Ly <sub>α</sub> 2p <sub>3/2</sub>	9318.71	He <sub>γ</sub>	4930.16
		Ly <sub>α</sub> 2p <sub>1/2</sub>	4967.31
		Ly <sub>α</sub> 2p <sub>3/2</sub>	4977.29

Si (Z = 14)	
Line	Energy (eV)
K <sub>α2</sub>	1739.38
K <sub>α1</sub>	1739.98
K <sub>β</sub>	1835.94
He <sub>α</sub> (y)	1853.90
He <sub>α</sub> (w)	1865.10
He <sub>β</sub>	2182.46
He <sub>γ</sub>	2293.98
He <sub>δ</sub>	2345.70
Ly <sub>α</sub> 2p <sub>1/2</sub>	2004.30
Ly <sub>α</sub> 2p <sub>3/2</sub>	2006.10
Ly <sub>β</sub>	2376.093
Ly <sub>γ</sub>	2506.0356
Ly <sub>δ</sub>	2566.1804

<sup>1</sup>Only lines which were observed in our experimental X-ray spectra

## B Targets fabrication

Modern techniques allow synthesizing nanostructures of almost any morphology one could think of. In this Appendix a short description of methods used to produce the samples studied in this work is given.

Generally, the methods of NW production can be attributed to either of two basic approaches: top-down and bottom-up. The top-down approach starts with a bulk material containing information about the future shape of structures and evolves scaling the sample down to nanoscopic formation, in other words, removing excess material. It offers a possibility of a precise patterning of the structures and is widely used in the semiconductor industry. Among the most popular top-down techniques for nanofabrication is lithography. On the contrary, the bottom-up approach can be compared with growth when starting from elemental objects (atoms and molecules) a complex structure is formed. There are a number of methods implying the use of such mechanisms as the metal-catalyst-assisted vapor–liquid–solid (VLS) [Wagner64] mechanism, the vapor–solid (VS) mechanism [Yang02; Liu05; Hsu05], and the template-assisted (TA) mechanism [Zhang03].

### **ZnO nanowire samples**

The ZnO NW samples were provided by the group “Physics of nano-scale solids” of Prof. Ronning (Institute of Solid State Physics, FSU Jena). All the samples (vertically and randomly oriented NW arrays) were grown by a vapor transport technique in a horizontal tube furnace. The adjustment of the synthesis conditions (e.g., temperature, pressure) results in different morphologies. A pure ZnO powder or its mixture with graphite powder (1:1) was evaporated at high temperatures (1350 °C or 1350 °C) for the randomly and vertically oriented NW arrays, respectively. The vapor was transported by a carrier gas (Ar or Ar + O<sub>2</sub>) downstream towards the cooled 500 μm-thick Si substrates. For the growth of the randomly oriented ZnO NWs, the substrate was covered beforehand with 10 nm gold droplets acting as a liquid catalyst. The synthesis was developing then according to the VLS mechanism. While for the growth of the vertically oriented NWs, the substrate was covered with a 500 nm Al-doped ZnO seed layer (AZO) and then the NWs grew self-catalytically according to the VS approach. Typical lengths and diameters for the ZnO NWs investigated within our project are about 5 - 15 μm and 50 - 700 nm. Though the described bottom-up technique is rather cost-efficient, the primary concern is the

control of the NW parameters and anisotropy of the NW arrays.

### Si nanowire samples

The Si NW samples were fabricated at the Institute of Applied Physics (FSU) by the students of Jun.-Prof. Stefanie Kroker. The preparation of the Si substrates included its coating with a chromium layer followed by an electron beam sensitive resist. In order to create a mask/define the periodic patterns, the electron beam lithography (EBL) with character projection was applied. The resist may be used directly as a mask or used together with a template mask transferring the pattern to it. After the development of a resist, the structure was transferred into the chromium and underlying substrate via reactive ion etching. Finally, the resist residuals and chromium were removed by wet chemical etching. Note, that the residuals were never fully eliminated. The resulting sample had a periodic structure of Si NWs. However, if the aspect ratio of the NWs is high, there is a risk that the structures tilt and even get in contact with each other instead of freestanding. Further details on the fabrication of Si NWs can be found in [Kroker13]. With this technique one can nicely control the geometry of nanowires, however, the cost of such a target is rather high.

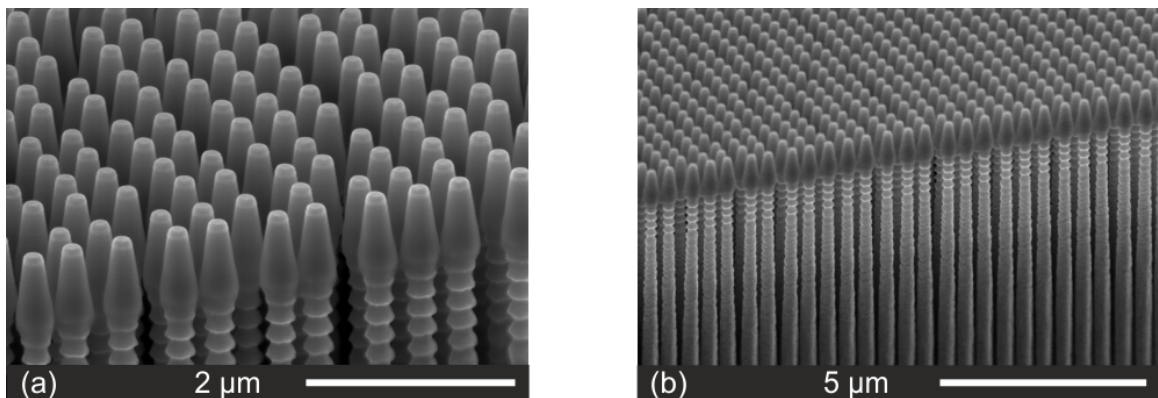


**Fig. B.1:** SEM images of a Si nanowire sample (the sample was tilted by 30°).

### Scanning electron microscopy

Most of the samples were characterized by a high-resolution scanning electron microscope (SEM). The most frequently used system is FEI DualBeam Helios NanoLab 600i FIB system equipped with a field emission electron gun. The samples could be measured with a lateral resolution of  $\sim 1 - 2$  nm. We normally used the secondary electron detection to acquire SEM images of the NW targets.

# C JETi-40 laser system

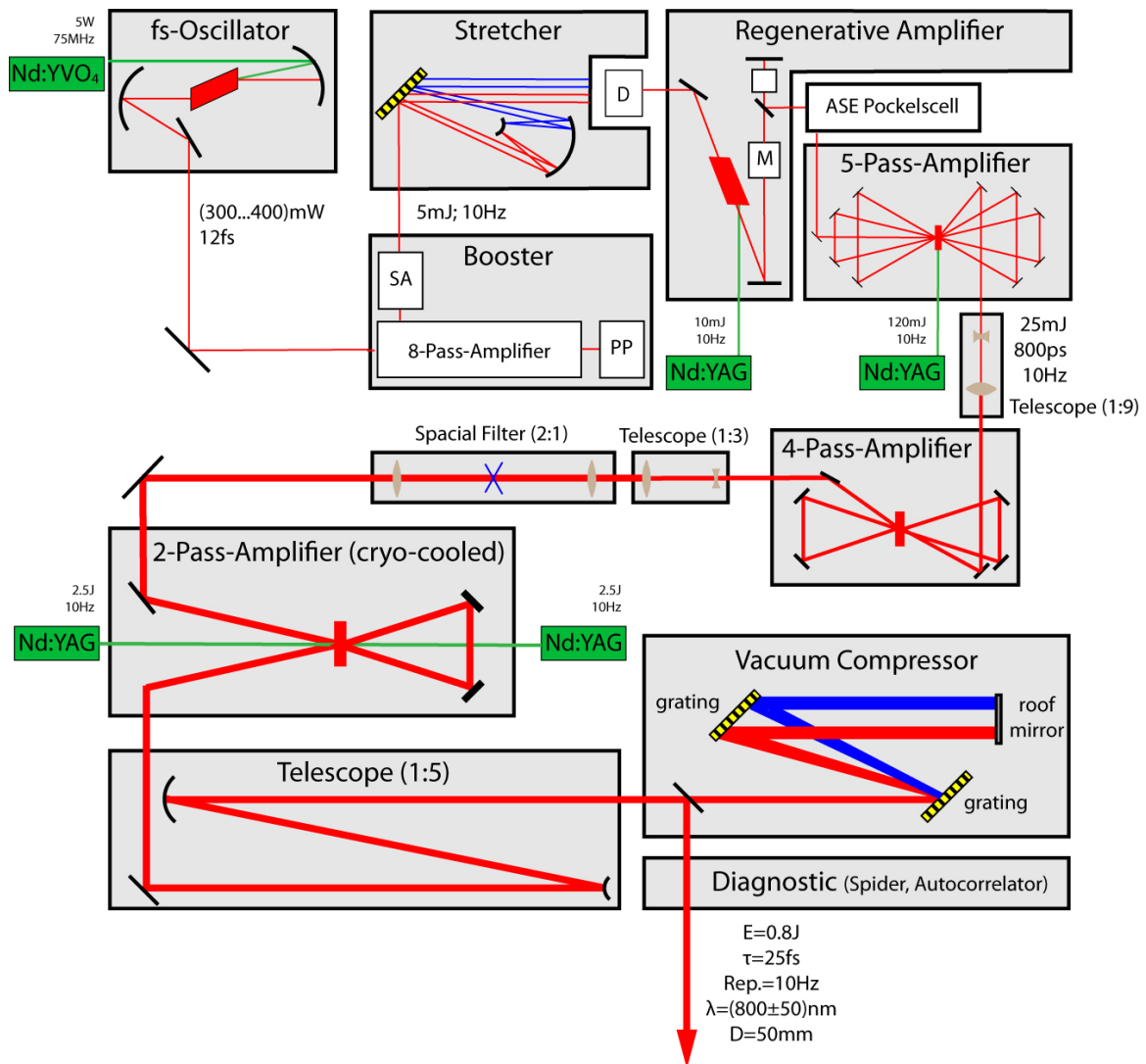


Fig. C.1: Technical scheme of JETi-40. (Courtesy of JETi laser team.)



# D Crystal spectrometers & X-ray detectors

KAP 001

Flat	
Bragg spectrometer	
Size	$50 \times 22 \text{ mm}^2$
Double net plane distance	$2d = 0.266 \text{ nm}$
Bragg angle for Si $K_{\alpha 1}$	$15.54^\circ$
Spectral resolution, $\lambda / \Delta\lambda$	$>1000$

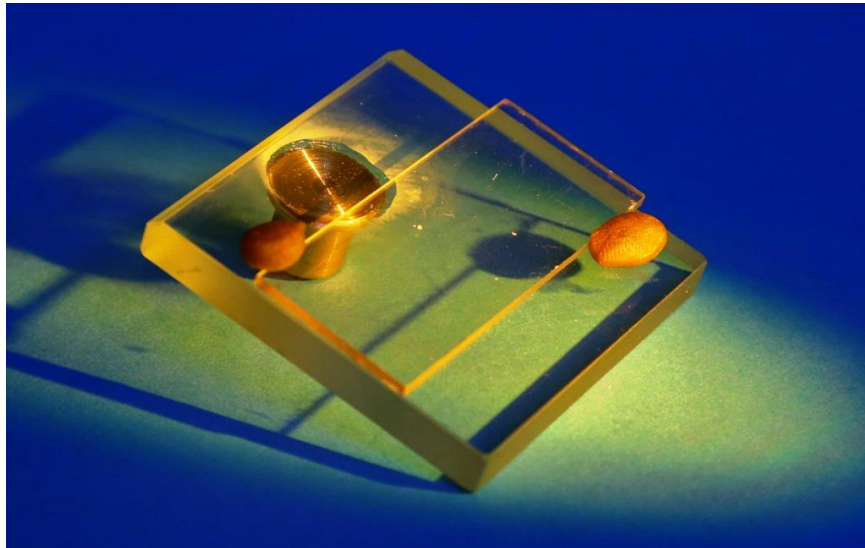


Fig. D.1: Photo of the used in the experiments KAP crystal.

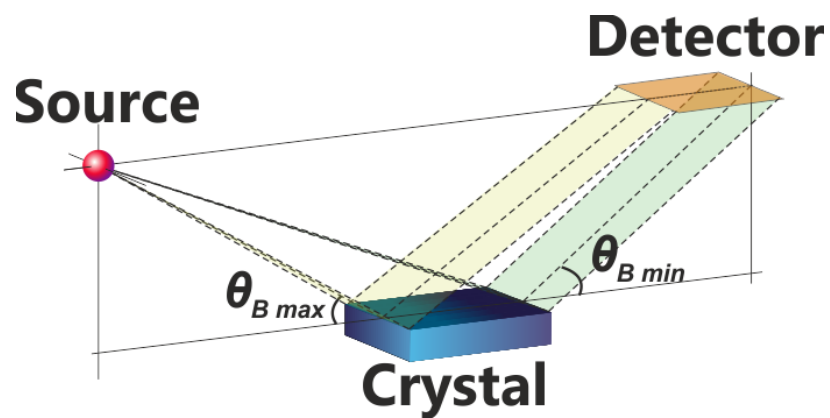
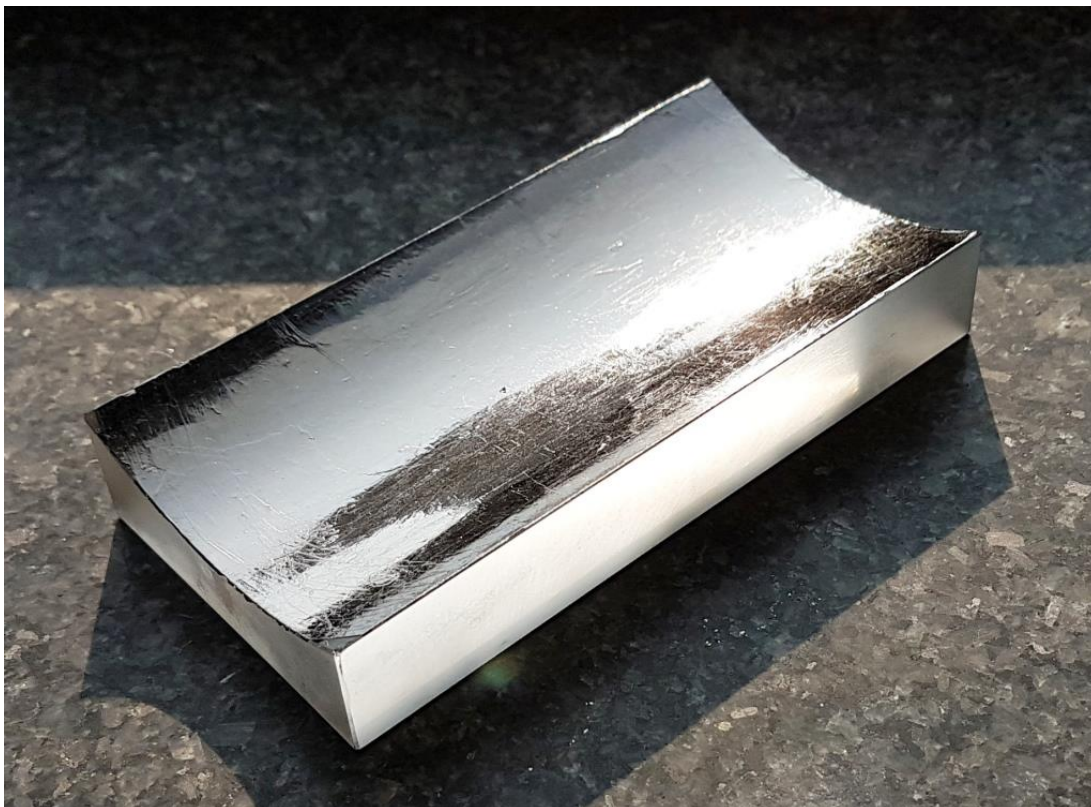


Fig. D.2: Schematic geometry of a Bragg crystal spectrometer.

## HOPG

Cylindrically bent ( $R = 50$ mm)	
von Hamos geometry	
Size	$100 \times 50$ mm <sup>2</sup>
Double net plane distance	$2d = 0.671$ nm
Bragg angle for Ti $K_{\alpha 1}$	$11.82^\circ$
Spectral resolution, $\lambda / \Delta\lambda$	$\sim 1000$



**Fig. D.3:** Photo of the used in the experiments HOPG crystal.

## LiF 220

Mosaic, cylindrically bent ( $R = 100$ mm)	
von Hamos geometry	
Size	$50 \times 60$ mm <sup>2</sup>
Double net plane distance	$2d = 0.2848$ nm
Bragg angle for Zn $K_{\alpha 1}$	$30.25^\circ$
Spectral resolution, $\lambda / \Delta\lambda$	$< 2000$

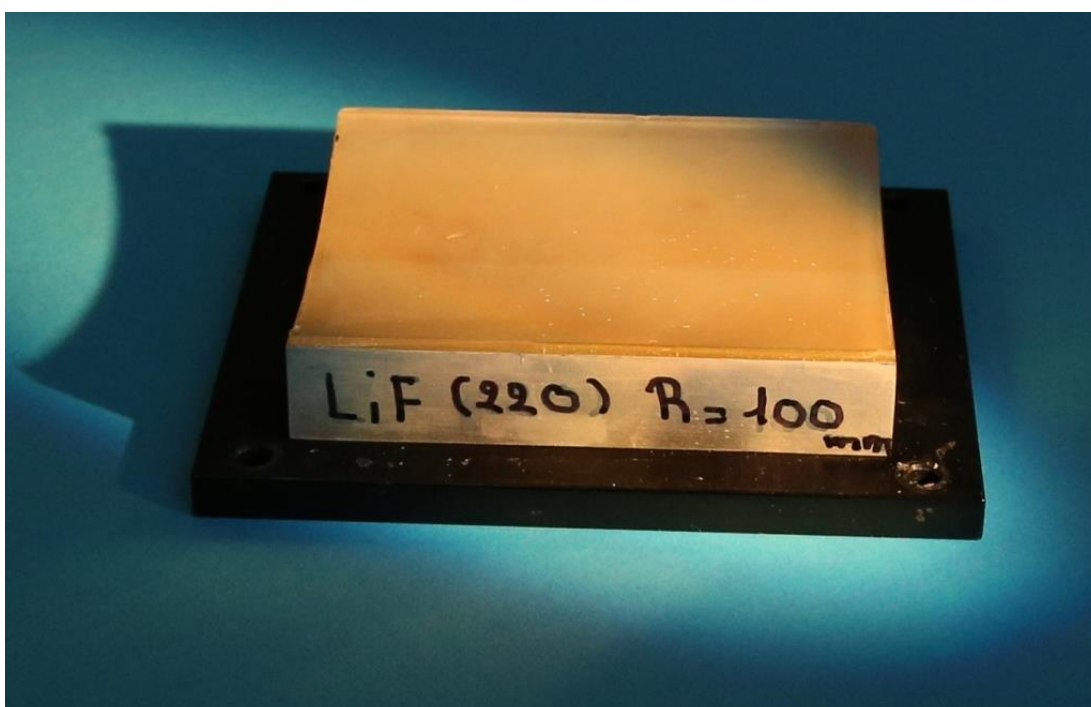


Fig. D.4: Photo of the used in the experiments LiF crystal.

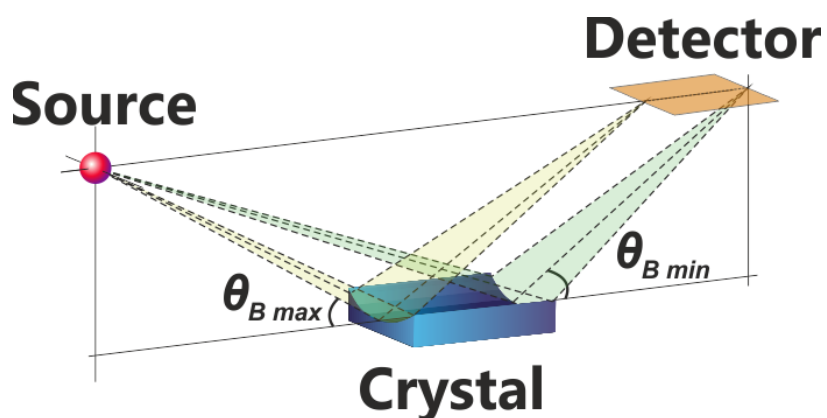


Fig. D.5: Schematic geometry of a von Hamos crystal spectrometer.  $\theta_{B \min, \max}$  – possible Bragg angles.

## Quartz 40-4

Toroidally bent ( $R_{hor} = 149.79$ mm, $R_{ver} = 106.39$ mm)	
Johann geometry	
Size	$23 \times 9$ mm <sup>2</sup>
Double net plane distance	$2d = 0.1671618$ nm
Bragg angle for Zn $K_{\alpha 1}$	$63.09^\circ$
Spectral resolution (CCD limit), $\lambda / \Delta\lambda$	$< 1500$

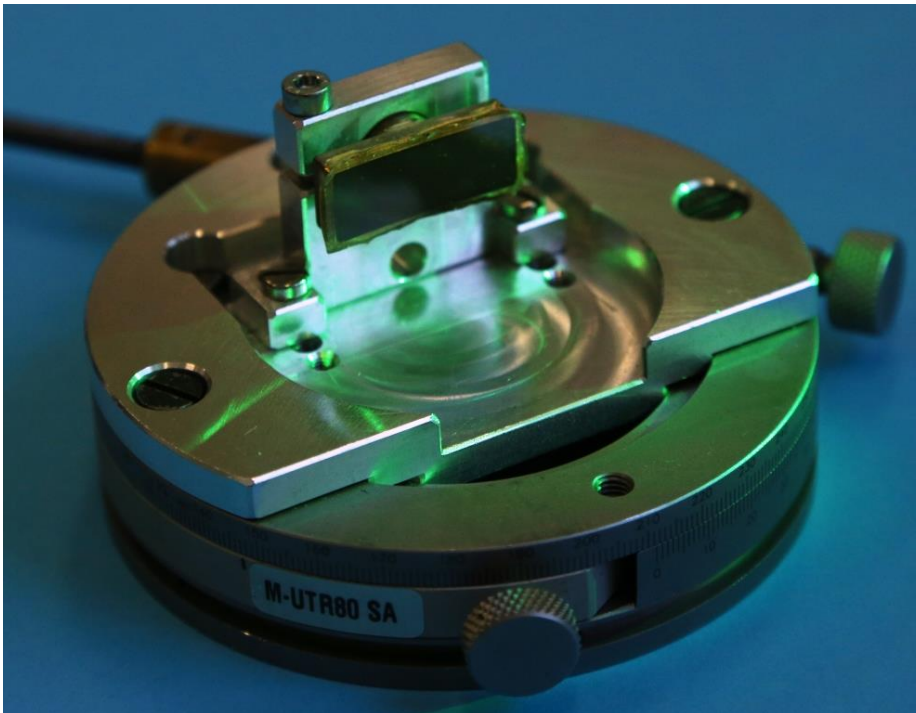


Fig. D.6: Photo of the used in the experiments quartz crystal in a holder.

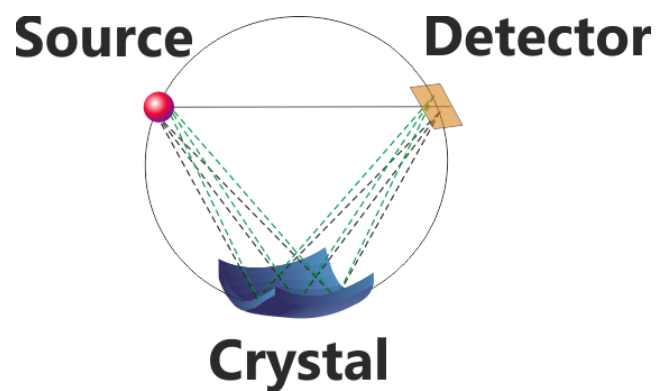


Fig. D.7: Schematic geometry of a Johann crystal spectrometer.

## Andor 420DX-BD-DD

Chip size (available area)	26.6×6.7 mm <sup>2</sup>
Pixels	1024×256
Readout time	4.5 s
Sensor material	Silicon (Si)
Chip thickness	50 μm
Energy resolution	340 eV

## Roper PI-MTE 1300B

Chip size (available area)	26.8×26.0 mm <sup>2</sup>
Pixels	1340×1300
Readout time	0.2-33.4 s
Sensor material	Silicon (Si)
Chip thickness	20 μm

## Timepix

Chip size (available area)	14.08×14.08 mm <sup>2</sup>
Pixels	256×256 or 128×128
Readout time	10 ms
Sensor material	Cadmium telluride (CdTe)
Chip thickness	1 mm

## E Thomson parabola spectrometer

Parameters	Values
Distance between the capacitor plates, $d$	$(0.025 \pm 0.001)$ m
Voltage across the capacitor plates, $U$	$\approx 7$ kV
Electric field, $E$	$(2.8 \pm 0.1) \times 10^5$ V/m
Magnetic field, $B$	$(0.525 \pm 0.025)$ T
The length of the field region, $L_1$	$(0.10 \pm 0.01)$ m
The distance from the end of the field region to MCP, $L_2$	0.0415-0.0515 m

**Tab. E.1:** The main parameters of the Thomson parabola spectrometer used in the experiments.

Assuming uniform electric and magnetic fields, the ion dispersion can be calculated from the Lorentz equation (Eq. 2.4). The resulting parabolic traces on MCP are described by the formula:

$$y = \frac{m}{q} \frac{E}{B^2 L_1 (L_2 + L_1/2)} x^2,$$

where  $(x, y)$  are the coordinates of a point on the MCP detector with respect to the zero-deflection point<sup>1</sup>,  $m$  is the ion mass,  $q$  is the charge state.

The size of the MCP plate (about 45 mm) sets the lower limit of the ion energy which can be detected. The MCP has two microchannel plates a phosphor screen. For the chosen configuration, we applied a voltage of 1 kV, 1.6 - 1.75 kV, and 5 kV, respectively.

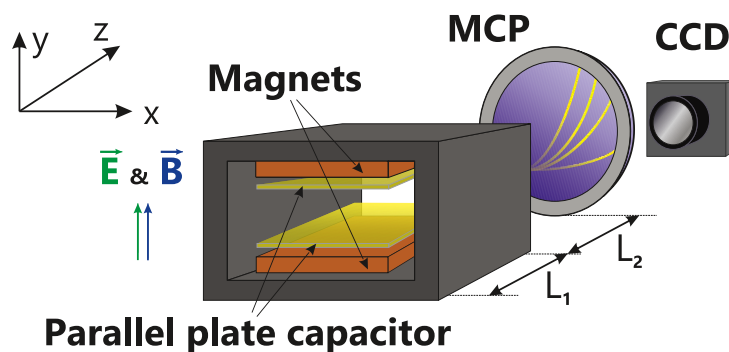


**Fig. E.1:** Schematic of the Thomson parabola spectrometer. The ion beam propagates along the z-axis.

<sup>1</sup>The point where the line connecting the source and the spectrometer's entrance pinholes on the detector would hit the detector (in our case, MCP). The neutral particles and photons would also end up at this point.



## F Reconstruction of X-ray spectra

An important part of the data processing is a reconstruction of the spectra. In our experiments, we used detectors with and without a dispersive element. The preparation of the images obtained with CCD cameras and Timepix starts from the selection of the images suitable for the analysis. On this step, we select only those images which a) contain data and b) represent an average result. For the detectors operating in a single-photon regime we consider only those images for which  $N/N_p \leq 0.15$  ( $N$  – a number of photons,  $N_p$  – a number of pixels). After that, the background must be subtracted. It is essential to exclude all hot spots and other not relevant artifacts.

To reconstruct spectra measured with a crystal spectrometer we cut out only the area of the image containing emission lines (Fig. F.1(a,b)). Then a histogram of a number of counts versus position in pixels is plotted. The positions can be recalculated into energies of photons; thereafter the line spectrum is obtained (see Fig. F.1 (c)).

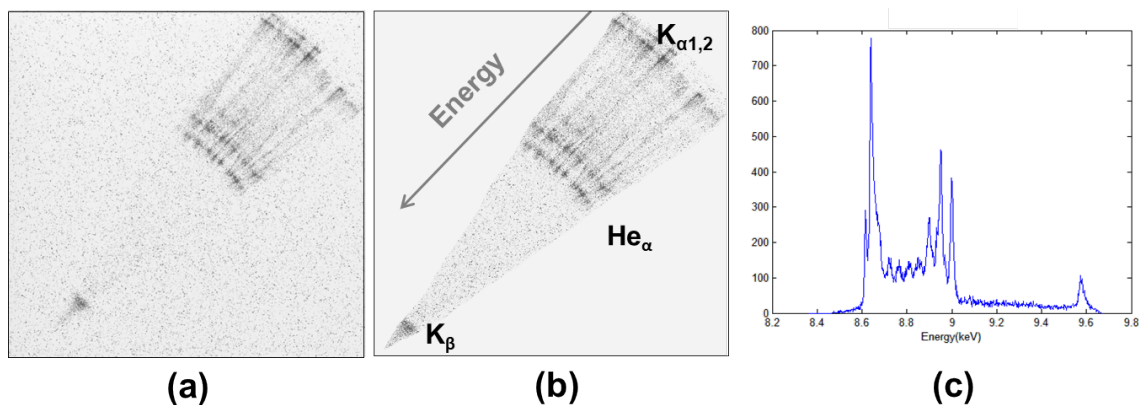


**Fig. F.1:** Reconstruction of a Zn spectrum measured with the LiF crystal spectrometer: (a) the original image, (b) the selected area with identified emission lines and (c) the resulting spectrum.

With the devices with no dispersive elements, the procedure differs. Making use of the fact that every single photon deposits energy into the chip of CCD creating a charge proportional to it, one can create a graph presenting the number of hits (channels) as a function of the charge. An algorithm searching for single events is applied. It operates as follows. A Matlab program searches for a group of closely located pixels with non-zero counts - clusters. Each pixel in a cluster is treated separately and either summed up with a neighbor as a single event or split into several events depending on the count distribution within the cluster. After

calibration of the detector, the created graph is nothing else but an X-ray spectrum. Finally, after processing of all available images, the spectra are averaged over a number of shots and corrected for absorption and sensitivity of the detector if necessary.



## G Target damage introduced during the interaction

### FemtoX experiments (Chapter 3)

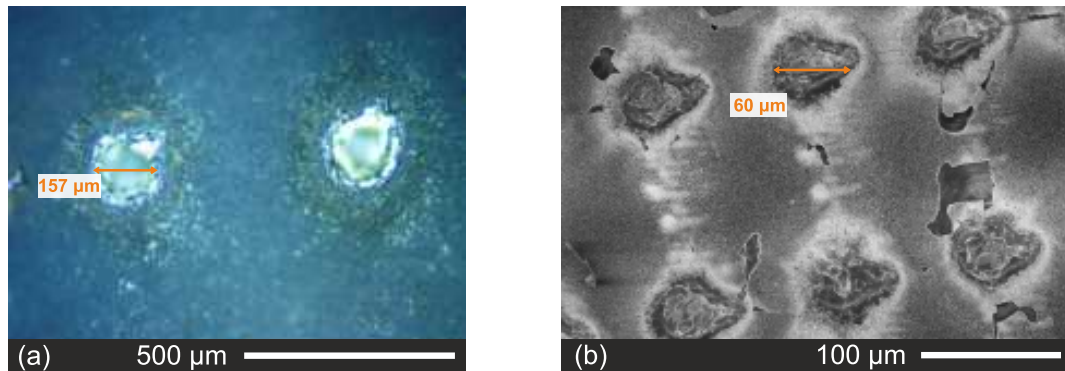


**Fig. G.1:** (a) Optical microscope image and (b) SEM image of the ZnO nanowire target.

### JETi-40 experiments (Chapter 4)

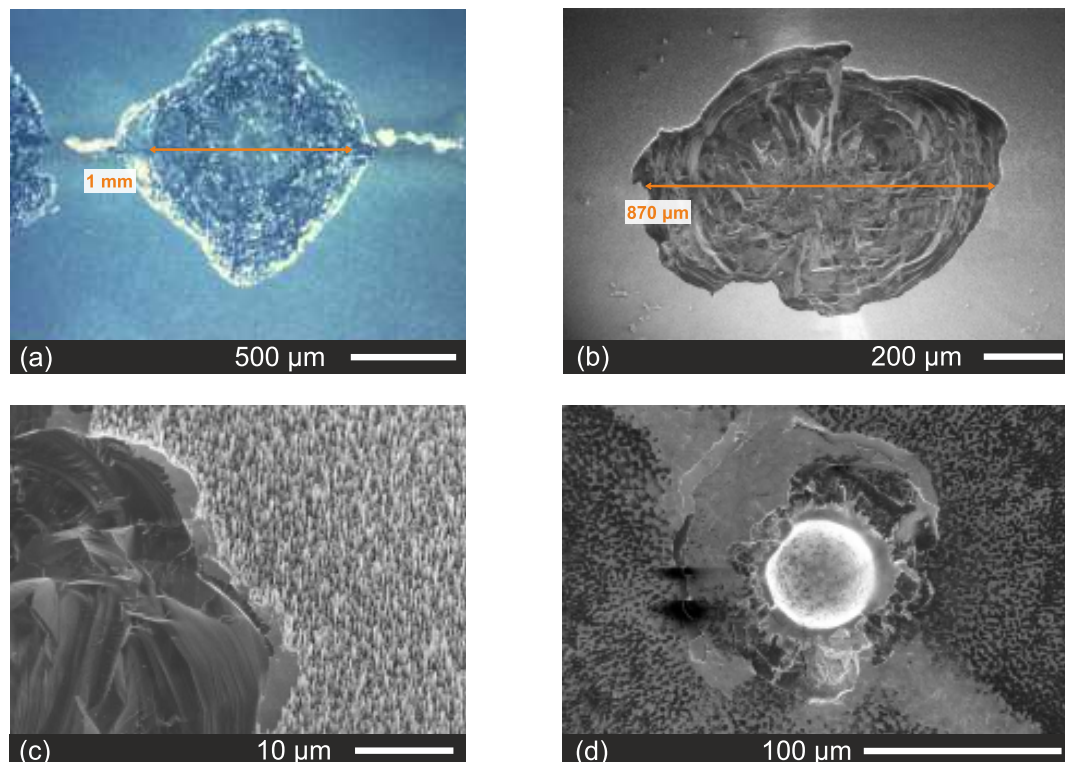


**Fig. G.2:** (a) Optical microscope image and (b) SEM image (with a tilt of 30°) of the ZnO nanowire target. (c) Edge of the damaged spot on the NW target. (d) SEM image of the polished ZnO target.

## OPCPA experiments (Chapter 5)

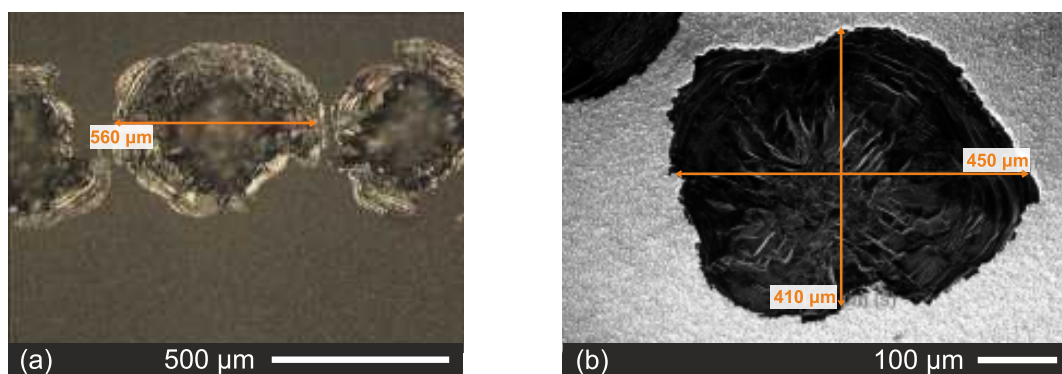


**Fig. G.3:** (a) Optical microscope image and (b) SEM image of the ZnO nanowire target.

# References

- [Ammosov86] M. V. Ammosov, N. B. Delone, and V. P. Krainov. „Ionization of atoms in an alternating electric field“. In: *JETP (Russian original - ZhETF, Vol. 91, No. 6, 1986)* 64.4 (1986), p. 1191 (cit. on pp. 10, 57).
- [Andreev13] A. A. Andreev and Yu. Platonov. „Interaction of ultra high intensity laser pulse with structured target and fast particle generation in a stable mode“. In: *Contributions to Plasma Physics* 53.2 (2013), pp. 173–178 (cit. on p. 42).
- [Andreev16] N. E. Andreev, L. P. Pugachev, M. E. Povarnitsyn, and P. R. Levashov. „Electron acceleration at grazing incidence of a subpicosecond intense laser pulse onto a plane solid target“. In: *Laser and Particle Beams* 34.1 (2016), pp. 115–122 (cit. on p. 56).
- [Andriukaitis11] G. Andriukaitis, T. Balčiūnas, S. Ališauskas, A. Pugžlys, A. Baltuška, T. Popmintchev, M.-C. Chen, M. M. Murnane, and H. C. Kapteyn. „90 GW peak power few-cycle mid-infrared pulses from an optical parametric amplifier“. In: *Optics Letters* 36.15 (2011), p. 2755 (cit. on p. 80).
- [Arnaud71] J. A. Arnaud, W. M. Hubbard, G. D. Mandeville, B. de la Clavière, E. A. Franke, and J. M. Franke. „Technique for fast measurement of Gaussian laser beam parameters“. In: *Applied Optics* 10.12 (1971), p. 2775 (cit. on p. 81).
- [Aurand13] B. Aurand, S. Kuschel, O. Jäckel, C. Rdel, H. Y. Zhao, S. Herzer, A. E. Paz, J. Bierbach, J. Polz, B. Elkin, G. G. Paulus, A. Karmakar, P. Gibbon, T. Kuehl, and M. C. Kaluza. „Radiation pressure-assisted acceleration of ions using multi-component foils in high-intensity laser-matter interactions“. In: *New Journal of Physics* 15.3 (2013), p. 033031 (cit. on p. 56).
- [Badziak07] J. Badziak. „Laser-driven generation of fast particles“. In: *Opto-Electronics Review* 15.1 (2007), pp. 1–12 (cit. on p. 73).

- [Bagchi11] S. Bagchi, P. Prem Kiran, K. Yang, A. M. Rao, M. K. Bhuyan, M. Krishnamurthy, and G. Ravindra Kumar. „Bright, low debris, ultrashort hard x-ray table top source using carbon nanotubes“. In: *Physics of Plasmas* 18.1 (2011), p. 014502 (cit. on p. 49).
- [Bagnoud16] V. Bagnoud and F. Wagner. „Ultrahigh temporal contrast performance of the PHELIX petawatt facility“. In: *High Power Laser Science and Engineering* 4 (2016) (cit. on p. 24).
- [Bargsten17] C. Bargsten, R. Hollinger, M. G. Capeluto, et al. „Energy penetration into arrays of aligned nanowires irradiated with relativistic intensities: Scaling to terabar pressures“. In: *Science Advances* 3.1 (2017). 1601558[PII], e1601558 (cit. on pp. 4, 62).
- [Basov85] N. G. Basov. „Editor’s foreword“. In: *Journal of Soviet Laser Research* 6.2 (1985), pp. 81–82 (cit. on p. 57).
- [Batani02] D. Batani. „Transport in dense matter of relativistic electrons produced in ultra-high-intensity laser interactions“. In: *Laser and Particle Beams* 20.02 (2002) (cit. on p. 36).
- [Batani10] D. Batani, R. Jafer, M. Veltcheva, R. Dezulian, O. Lundh, F. Lindau, A. Persson, K. Osvay, C.-G. Wahlström, D. C. Carroll, P. McKenna, A. Flacco, and V. Malka. „Effects of laser prepulses on laser-induced proton generation“. In: *New Journal of Physics* 12.4 (2010), p. 045018 (cit. on p. 24).
- [Beg97] F. N. Beg, A. R. Bell, A. E. Dangor, C. N. Danson, A. P. Fews, M. E. Glinsky, B. A. Hammel, P. Lee, P. A. Norreys, and M. Tatarakis. „A study of picosecond laser–solid interactions up to  $1E19\text{ W/cm}^2$ “. In: *Physics of Plasmas* 4.2 (1997), pp. 447–457 (cit. on pp. 17, 41).
- [Benesch04] F. Benesch, T. Lee, Y. Jiang, and C. G. Rose-Petruck. „Ultrafast laser-driven x-ray spectrometer for X-ray absorption spectroscopy of transition metal complexes“. In: *Optics Letters* 29.9 (2004), p. 1028 (cit. on p. 41).
- [Borm16] B. Borm, F. Gärtner, D. Khaghani, and P. Neumayer. „Improvement of density resolution in short-pulse hard X-ray radiographic imaging using detector stacks“. In: *Review of Scientific Instruments* 87.9 (2016), p. 093104 (cit. on p. 56).
- [Brunel87] F. Brunel. „Not-so-resonant, resonant absorption“. In: *Physical Review Letters* 59 (1987), pp. 52–55 (cit. on pp. 17, 48, 94).
- [Burgess65] A. Burgess. „A general formula for the estimation of dielectronic recombination coefficients in low-density plasmas“. In: *Astrophysical Journal* 141 (1965), pp. 1588–1590 (cit. on p. 34).

- [Burnett77] N. H. Burnett, H. A. Baldis, M. C. Richardson, and G. D. Enright. „Harmonic generation in CO<sub>2</sub> laser target interaction“. In: *Applied Physics Letters* 31.3 (1977), pp. 172–174 (cit. on p. 78).
- [Burnett86] N. H. Burnett and G. D. Enright. „Hot-electron generation and transport in high-intensity laser interaction“. In: *Canadian Journal of Physics* 64.8 (1986), pp. 920–931 (cit. on p. 47).
- [Catto77] P. J. Catto and R. M. More. „Sheath inverse bremsstrahlung in laser produced plasmas“. In: *The Physics of Fluids* 20.4 (1977), pp. 704–705 (cit. on p. 19).
- [Chakravarty11] U. Chakravarty, P. A. Naik, B. S. Rao, V. Arora, H. Singhal, G. M. Bhalerao, A. K. Sinha, P. Tiwari, and P. D. Gupta. „Enhanced soft X-ray emission from carbon nanofibers irradiated with ultra-short laser pulses“. In: *Applied Physics B* 103.3 (2011), pp. 571–577 (cit. on p. 4).
- [Chen01] L. M. Chen, J. Zhang, Q. L. Dong, H. Teng, T. J. Liang, L. Z. Zhao, and Z. Y. Wei. „Hot electron generation via vacuum heating process in femtosecond laser-solid interactions“. In: *Physics of Plasmas* 8.6 (2001), pp. 2925–2929 (cit. on p. 48).
- [Chen09] C. D. Chen, P. K. Patel, D. S. Hey, et al. „Bremsstrahlung and K<sub>α</sub> fluorescence measurements for inferring conversion efficiencies into fast ignition relevant hot electrons“. In: *Physics of Plasmas* 16.8 (2009), p. 082705 (cit. on p. 45).
- [Chen84] F. F. Chen. *Introduction to Plasma Physics and Controlled Fusion. Volume 1: Plasma Physics*. Springer US, 1984 (cit. on p. 8).
- [Chung05] H.-K. Chung, M. H. Chen, W. L. Morgan, Y. Ralchenko, and R. W. Lee. „FLYCHK: Generalized population kinetics and spectral model for rapid spectroscopic analysis for all elements“. In: *High Energy Density Physics* 1.1 (2005), pp. 3–12 (cit. on pp. 39, 58, 59, 68, 87, 92).
- [Chung15] H.-K. Chung. *Atomic processes in dense plasmas, [Online]*. 2015 Joint ICTP-IAEA Advanced School and Workshop on Modern Methods in Plasma Spectroscopy. 2015 (cit. on p. 28).
- [Corde13] S. Corde, K. Ta Phuoc, G. Lambert, R. Fitour, V. Malka, A. Rousse, A. Beck, and E. Lefebvre. „Femtosecond X-rays from laser-plasma accelerators“. In: *Reviews of Modern Physics* 85.1 (2013), pp. 1–48 (cit. on p. 3).
- [Cowan00] T. E. Cowan, A. W. Hunt, T. W. Phillips, S. C. Wilks, M. D. Perry, C. Brown, W. Fountain, S. Hatchett, J. Johnson, M. H. Key, T. Parnell, D. M. Pennington, R. A. Snavely, and Y. Takahashi. „Photonuclear fission from high energy electrons from ultraintense laser-solid interactions“. In: *Physical Review Letters* 84 (2000), pp. 903–906 (cit. on p. 41).

- [Cristoforetti14] G. Cristoforetti, A. Anzalone, F. Baffigi, G. Bussolino, G. D'Arrigo, L. Fulgentini, A. Giulietti, P. Koester, L. Labate, S. Tudisco, and L. A. Gizzi. „Investigation on laser-plasma coupling in intense, ultrashort irradiation of a nanostructured silicon target.“ In: *Plasma Physics and Controlled Fusion* 56.9 (2014), p. 095001 (cit. on pp. 4, 42).
- [Cristoforetti17] G. Cristoforetti, P. Londrillo, P. K. Singh, F. Baffigi, G. D'Arrigo, Amit D. Lad, R. G. Milazzo, A. Adak, M. Shaikh, D. Sarkar, G. Chatterjee, J. Jha, M. Krishnamurthy, G. R. Kumar, and L. A. Gizzi. „Transition from Coherent to Stochastic electron heating in ultrashort relativistic laser interaction with structured targets“. In: *Scientific Reports* 7.1 (2017) (cit. on p. 20).
- [Curtis18] A. Curtis, C. Calvi, J. Tinsley, R. Hollinger, V. Kaymak, A. Pukhov, S. Wang, A. Rockwood, Y. Wang, V. N. Shlyaptsev, and J. J. Rocca. „Micro-scale fusion in dense relativistic nanowire array plasmas“. In: *Nature Communications* 9.1 (2018) (cit. on p. 4).
- [Dalui15] M. Dalui, W.-M. Wang, T. M. Trivikram, S. Sarkar, S. Tata, J. Jha, P. Ayyub, Z. M. Sheng, and M. Krishnamurthy. „Preferential enhancement of laser-driven carbon ion acceleration from optimized nanostructured surfaces“. In: *Scientific Reports* 5.1 (2015) (cit. on p. 74).
- [Dalui17] M. Dalui, T. M. Trivikram, J. Colgan, J. Pasley, and M. Krishnamurthy. „Compact acceleration of energetic neutral atoms using high intensity laser-solid interaction“. In: *Scientific Reports* 7.1 (2017) (cit. on p. 74).
- [Ditmire99] T. Ditmire, J. Zweiback, V. P. Yanovsky, T. E. Cowan, G. Hays, and K. B. Wharton. „Nuclear fusion from explosions of femtosecond laser-heated deuterium clusters“. In: *Nature* 398.6727 (1999), pp. 489–492 (cit. on p. 3).
- [Dittrich94] T. R. Dittrich, B. A. Hammel, C. J. Keane, R. McEachern, R. E. Turner, S. W. Haan, and L. J. Suter. „Diagnosis of Pusher-Fuel Mix in Indirectly Driven Nova Implosions“. In: *Physical Review Letters* 73.17 (1994), pp. 2324–2327 (cit. on p. 3).
- [Drake06] R. P. Drake. *High-Energy-Density Physics: Fundamentals, Inertial Fusion, and Experimental Astrophysics (Shock Wave and High Pressure Phenomena)*. Springer Berlin Heidelberg, 2006 (cit. on p. 21).
- [Einstein05] A. Einstein. „Über einen die Erzeugung und Verwandlung des Lichtes betreffenden heuristischen Gesichtspunkt“. In: *Annalen der Physik* 322.6 (1905), pp. 132–148 (cit. on p. 8).
- [Eliezer02] S. Eliezer. *The Interaction of High-Power Lasers with Plasmas*. CRC Press, 2002 (cit. on pp. 8, 21).

- [Elliot93] J. A. Elliot. *Plasma kinetic theory. Plasma physics: An introductory course, Chapter 2.* Dendy R. O. (ed.), 1993. Cambridge University Press, 1993 (cit. on p. 26).
- [Faisal76] F. H. M. Faisal. „Exact perturbation theory of multiphoton processes at high intensities“. In: *Il Nuovo Cimento B Series 11* 33.2 (1976), pp. 775–795 (cit. on p. 9).
- [Fourmaux16] S. Fourmaux and J. C. Kieffer. „Laser-based  $K_{\alpha}$  X-ray emission characterization using a high contrast ratio and high-power laser system“. In: *Applied Physics B* 122.6 (2016), p. 162 (cit. on p. 41).
- [Fuchs05] J. Fuchs, P. Antici, E. d’Humières, et al. „Laser-driven proton scaling laws and new paths towards energy increase“. In: *Nature Physics* 2.1 (2005), pp. 48–54 (cit. on p. 3).
- [Fujioka09] S. Fujioka, H. Takabe, N. Yamamoto, et al. „X-ray astronomy in the laboratory with a miniature compact object produced by laser-driven implosion“. In: *Nature Physics* 5 (2009), 821 EP – (cit. on p. 3).
- [Fullagar07] W. Fullagar, M. Harbst, S. Canton, J. Uhlig, M. Walczak, C.-G. Wahlström, and V. Sundström. „A broadband laser plasma X-ray source for application in ultrafast chemical structure dynamics“. In: *Review of Scientific Instruments* 78.11 (2007), p. 115105 (cit. on p. 41).
- [Gaunt30] J. A. Gaunt. „Continuous Absorption“. In: *Proceedings of the Royal Society A: Mathematical, Physical and Engineering Sciences* 126.803 (1930), pp. 654–660 (cit. on p. 31).
- [Gavrilov04] S. A. Gavrilov, D. M. Golishnilov, V. M. Gordienko, A. B. Savel’ev, and R. V. Volkov. „Efficient hard X-ray source using femtosecond plasma at solid targets with a modified surface“. In: *Laser and Particle Beams* 22.03 (2004) (cit. on p. 4).
- [Gibbon05] P. Gibbon. *Short Pulse Laser Interactions with Matter: An Introduction.* Imperial College Press, 2005 (cit. on p. 8).
- [Gibbon92] P. Gibbon and A. R. Bell. „Collisionless absorption in sharp-edged plasmas“. In: *Physical Review Letters* 68.10 (1992), pp. 1535–1538 (cit. on p. 48).
- [Glenzer10] S. H. Glenzer, B. J. MacGowan, P. Michel, et al. „Symmetric inertial confinement fusion implosions at ultra-high laser energies“. In: *Science* 327.5970 (2010), pp. 1228–1231 (cit. on p. 3).
- [Gordon94] S. P. Gordon, T. Donnelly, A. Sullivan, H. Hamster, and R. W. Falcone. „X rays from microstructured targets heated by femtosecond lasers“. In: *Optics Letters* 19.7 (1994), pp. 484–486 (cit. on p. 4).

- [Gregori12] G. Gregori, A. Ravasio, C. D. Murphy, et al. „Generation of scaled protogalactic seed magnetic fields in laser-produced shock waves“. In: *Nature* 481.7382 (2012), pp. 480–483 (cit. on p. 3).
- [Griem63] H. R. Griem. „Validity of local thermal equilibrium in plasma spectroscopy“. In: *Physical Review* 131 (1963), pp. 1170–1176 (cit. on p. 38).
- [Guethlein96] G. Guethlein, M. E. Foord, and D. Price. „Electron temperature measurements of solid density plasmas produced by intense ultrashort laser pulses“. In: *Physical Review Letters* 77.6 (1996), pp. 1055–1058 (cit. on p. 3).
- [Gunst14] J. Gunst, Y. A. Litvinov, C. H. Keitel, and A. Pálffy. „Dominant secondary nuclear photoexcitation with the X-ray Free-Electron Laser“. In: *Physical Review Letters* 112.8 (2014) (cit. on p. 96).
- [Gunst15] J. Gunst, Y. Wu, N. Kumar, C. H. Keitel, and A. Pálffy. „Direct and secondary nuclear excitation with X-ray free-electron lasers“. In: *Physics of Plasmas* 22.11 (2015), p. 112706 (cit. on p. 96).
- [Hagedorn03] M. Hagedorn, J. Kutzner, G. Tsilimis, and H. Zacharias. „High-repetition-rate hard X-ray generation with sub-millijoule femtosecond laser pulses“. In: *Applied Physics B* 77.1 (2003), pp. 49–57 (cit. on p. 41).
- [Hahn16] C. Hahn, G. Weber, R. Martin, S. Höfer, T. Kämpfer, and Th. Stöhlker. „CdTe Timepix detectors for single-photon spectroscopy and linear polarimetry of high-flux hard X-ray radiation“. In: *Review of Scientific Instruments* 87.4 (2016), p. 043106 (cit. on pp. 45, 82).
- [Haines09] M. G. Haines, M. S. Wei, F. N. Beg, and R. B. Stephens. „Hot-electron temperature and laser-light absorption in fast ignition“. In: *Physical Review Letters* 102 (2009), p. 045008 (cit. on p. 48).
- [Henke93] B. L. Henke, E. M. Gullikson, and J. C. Davis. „X-Ray interactions: photoabsorption, scattering, transmission, and reflection at  $E = 50\text{--}30,000$  eV,  $Z = 1\text{--}92$ “. In: *Atomic Data and Nuclear Data Tables* 54 (1993), pp. 181–342 (cit. on p. 52).
- [Hoefler14] S. Höfer. „Zeitaufgelöste Röntgenbeugung an einkristallinem Indiumantimonid“. PhD thesis. Friedrich-Schiller-Universität, Jena, 2014 (cit. on p. 43).
- [Hoefler16] S. Höfer, T. Kämpfer, E. Förster, T. Stöhlker, and I. Uschmann. „The formation of rarefaction waves in semiconductors after ultrashort excitation probed by grazing incidence ultrafast time-resolved X-ray diffraction“. In: *Structural Dynamics* 3 (2016), p. 051101 (cit. on p. 41).



- [Hollinger17a] R. Hollinger, C. Bargsten, V. N. Shlyaptsev, V. Kaymak, A. Pukhov, M. G. Capeluto, S. Wang, A. Rockwood, Y. Wang, A. Townsend, A. Prieto, P. Stockton, A. Curtis, and J. J. Rocca. „Efficient picosecond X-ray pulse generation from plasmas in the radiation dominated regime“. In: *Optica* 4.11 (2017), pp. 1344–1349 (cit. on pp. 92, 93).
- [Holtz17] M. Holtz, C. Hauf, J. Weisshaupt, A.-A. H. Salvador, M. Woerner, and T. Elsaesser. „Towards shot-noise limited diffraction experiments with table-top femtosecond hard X-ray sources“. In: *Structural Dynamics* 4.5 (2017), p. 054304 (cit. on p. 41).
- [Hsu05] C.-L. Hsu, S.-J. Chang, Y.-R. Lin, P.-C. Li, T.-S. Lin, S.-Y. Tsai, T.-H. Lu, and I.-C. Chen. „Ultraviolet photodetectors with low temperature synthesized vertical ZnO nanowires“. In: *Chemical Physics Letters* 416.1-3 (2005), pp. 75–78 (cit. on p. 104).
- [Ivanov13] K. A. Ivanov, S. A. Shulyapov, A. A. Turinge, A. V. Brantov, D. S. Uryupina, R. V. Volkov, A. V. Rusakov, R. M. Djilkibaev, V. G. Nedorezov, V. Yu. Bychenkov, and A. B. Savel'ev. „X-Ray diagnostics of ultrashort laser-driven plasma: experiment and simulations“. In: *Contributions to Plasma Physics* 53.2 (2013), pp. 116–121 (cit. on p. 47).
- [Ivanov17] K. A. Ivanov, I. N. Tsymbalov, S. A. Shulyapov, D. A. Krestovskikh, A. V. Brantov, V. Yu. Bychenkov, R. V. Volkov, and A. B. Savel'ev. „Pre-pulse controlled electron acceleration from solids by a femtosecond laser pulse in the slightly relativistic regime“. In: *Physics of Plasmas* 24.6 (2017), p. 063109 (cit. on p. 56).
- [Jiang14a] S. Jiang, A. G. Krygier, D. W. Schumacher, K. U. Akli, and R. R. Freeman. „Effects of front-surface target structures on properties of relativistic laser-plasma electrons“. In: *Physical Review E* 89.1 (2014) (cit. on pp. 4, 20).
- [Jiang14b] S. Jiang, A. G. Krygier, D. W. Schumacher, K. U. Akli, and R. R. Freeman. „Enhancing Bremsstrahlung production from ultraintense laser-solid interactions with front surface structures“. In: *The European Physical Journal D* 68.10 (2014), p. 283 (cit. on p. 20).
- [Jiang16] S. Jiang, L. L. Ji, H. Audesirk, K. M. George, J. Snyder, A. Krygier, P. Poole, C. Willis, R. Daskalova, E. Chowdhury, N. S. Lewis, D. W. Schumacher, A. Pukhov, R. R. Freeman, and K. U. Akli. „Microengineering Laser Plasma Interactions at Relativistic Intensities“. In: *Physical Review Letters* 116 (2016), p. 085002 (cit. on p. 4).
- [Kaluza04] M. Kaluza, J. Schreiber, M. I. K. Santala, G. D. Tsakiris, K. Eidmann, J. Meyer-ter Vehn, and K. J. Witte. „Influence of the laser prepulse on proton acceleration in thin-foil experiments“. In: *Physical Review Letters* 93 (2004), p. 045003 (cit. on p. 56).

- [Kaymak16] V. Kaymak, A. Pukhov, V. N. Shlyaptsev, and J. J. Rocca. „Nanoscale Ultradense Z-Pinch Formation from Laser-Irradiated Nanowire Arrays“. In: *Physical Review Letters* 117 (2016), p. 035004 (cit. on pp. 5, 98).
- [Keldysh65] L. V. Keldysh. „Ionization in the field of a strong electromagnetic wave“. In: *Soviet Physics JETP* 20 (1965), pp. 1307–1314 (cit. on pp. 8, 78).
- [Keppler15] Sebastian Keppler, Alexander Sävert, Jörg Körner, Marco Hornung, Hartmut Liebetrau, Joachim Hein, and Malte Christoph Kaluza. „The generation of amplified spontaneous emission in high-power CPA laser systems“. In: *Laser & Photonics Reviews* 10.2 (2015), pp. 264–277 (cit. on p. 24).
- [Khaghani17] D. Khaghani, M. Lobet, B. Borm, L. Burr, F. Gärtner, L. Gremillet, L. Movsesyan, O. Rosmej, M. E. Toimil-Molares, F. Wagner, and P. Neumayer. „Enhancing laser-driven proton acceleration by using micro-pillar arrays at high drive energy“. In: *Scientific Reports* 7.1 (2017) (cit. on pp. 4, 69).
- [Khan80] Md. R. Khan and M. Karimi. „ $K_{\beta}/K_{\alpha}$  ratios in energy-dispersive x-ray emission analysis“. In: *X-Ray Spectrometry* 9.1 (1980), pp. 32–35 (cit. on p. 86).
- [Khattak05] F. Y. Khattak, R. J. Clarke, E. J. Divall, M. Edwards, P. S. Foster, C. J. Hooker, A. J. Langley, P. Mistry, D. Neely, O. A. M. B. Percie du Sert, J. Smith, C. Spindloe, G. Tallents, M. Tolley, and D. Riley. „Enhanced  $He_{\alpha}$  emission from "smoked" Ti targets irradiated with 400 nm, 45 fs laser pulses“. In: *EPL (Europhysics Letters)* 72.2 (2005), p. 242 (cit. on p. 4).
- [Khosrofian83] J. M. Khosrofian and B. A. Garetz. „Measurement of a Gaussian laser beam diameter through the direct inversion of knife-edge data“. In: *Applied Optics* 22.21 (1983), p. 3406 (cit. on p. 81).
- [Klimo11] O. Klimo, J. Psikal, J. Limpouch, J. Proska, F. Novotny, T. Ceccotti, V. Floquet, and S. Kawata. „Short pulse laser interaction with microstructured targets: simulations of laser absorption and ion acceleration“. In: *New Journal of Physics* 13.5 (2011), p. 053028 (cit. on p. 4).
- [Koenig04] M. Koenig, E. Henry, G. Huser, et al. „High pressures generated by laser driven shocks: applications to planetary physics“. In: *Nuclear Fusion* 44.12 (2004), S208–S214 (cit. on p. 3).
- [Kramers23] H. A. Kramers. „XCIII. On the theory of X-ray absorption and of the continuous X-ray spectrum“. In: *The London, Edinburgh, and Dublin Philosophical Magazine and Journal of Science* 46.275 (1923), pp. 836–871 (cit. on p. 30).

- [Kroker13] S. Kroker, T. Käsebier, S. Steiner, E.-B. Kley, and A. Tünnermann. „High efficiency two-dimensional grating reflectors with angularly tunable polarization efficiency“. In: *Applied Physics Letters* 102.16 (2013), p. 161111 (cit. on p. 105).
- [Kruer88] W.L. Kruer. *The physics of laser plasma interactions*. Frontiers in physics. Addison-Wesley, 1988 (cit. on pp. 8, 16, 21, 48).
- [Kulsar00] G. Kulcsár, D. AlMawlawi, F. W. Budnik, P. R. Herman, M. Moskovits, L. Zhao, and R. S. Marjoribanks. „Intense picosecond X-ray pulses from laser plasmas by use of nanostructured "velvet" targets“. In: *Physical Review Letters* 84 (2000), pp. 5149–5152 (cit. on pp. 4, 41).
- [Liseykina15] T. Liseykina, P. Mulser, and M. Murakami. „Collisionless absorption, hot electron generation, and energy scaling in intense laser-target interaction“. In: *Physics of Plasmas* 22.3 (2015), p. 033302 (cit. on p. 48).
- [Liu05] R. Liu, A. Bell, F. A. Ponce, C. Q. Chen, J. W. Yang, and M. A. Khan. „Luminescence from stacking faults in gallium nitride“. In: *Applied Physics Letters* 86.2 (2005), p. 021908 (cit. on p. 104).
- [Livet00] F. Livet, F. Bley, J. Mainville, R. Caudron, S. G. J. Mochrie, E. Geissler, G. Dolino, D. Abernathy, G. Grübel, and M. Sutton. „Using direct illumination CCDs as high-resolution area detectors for X-ray scattering“. In: *Nuclear Instruments and Methods in Physics Research Section A: Accelerators, Spectrometers, Detectors and Associated Equipment* 451.3 (2000), pp. 596–609 (cit. on p. 46).
- [Loetzsch12a] R. Loetzsch, O. Jäckel, S. Höfer, T. Kämpfer, J. Polz, I. Uschmann, M. C. Kaluza, E. Förster, E. Stambulchik, E. Kroupp, and Y. Maron. „K-shell spectroscopy of silicon ions as diagnostic for high electric fields“. In: *Review of Scientific Instruments* 83.11 (2012), p. 113507 (cit. on p. 46).
- [Lotz67a] W. Lotz. „An empirical formula for the electron-impact ionization cross-section“. In: *Zeitschrift für Physik* 206.2 (1967), pp. 205–211 (cit. on p. 10).
- [Luebcke17] A. Lübcke, A. A. Andreev, S. Höhm, R. Grunwald, L. Ehrentraut, and M. Schnürer. „Prospects of target nanostructuring for laser proton acceleration“. In: *Scientific Reports* 7.1 (2017) (cit. on pp. 4, 20).
- [Macchi13] A. Macchi, M. Borghesi, and M. Passoni. „Ion acceleration by superintense laser-plasma interaction“. In: *Reviews of Modern Physics* 85.2 (2013), pp. 751–793 (cit. on p. 3).
- [Malka12] V. Malka. „Laser plasma accelerators“. In: *Physics of Plasmas* 19.5 (2012), p. 055501 (cit. on p. 3).

- [Malka97] G. Malka, J. Fuchs, F. Amiranoff, S. D. Baton, R. Gaillard, J. L. Miquel, H. Pépin, C. Rousseaux, G. Bonnaud, M. Busquet, and L. Lours. „Suprathermal electron generation and channel formation by an ultrarelativistic laser pulse in an underdense preformed plasma“. In: *Physical Review Letters* 79.11 (1997), pp. 2053–2056 (cit. on p. 13).
- [McCall82] G. H. McCall. „Calculation of X-ray bremsstrahlung and characteristic line emission produced by a Maxwellian electron distribution“. In: *Journal of Physics D: Applied Physics* 15.5 (1982), pp. 823–831 (cit. on p. 47).
- [Mewe72] R. Mewe. „Interpolation formula for the electron impact excitation of ions in the H-, He-, Li-, and Ne- sequences“. In: *Astronomy and Astrophysics* 20 (1972), p. 215 (cit. on p. 32).
- [Mondal11] S. Mondal, I. Chakraborty, S. Ahmad, D. Carvalho, P. Singh, A. D. Lad, V. Narayanan, P. Ayyub, G. R. Kumar, J. Zheng, and Z.M. Sheng. „Highly enhanced hard X-ray emission from oriented metal nanorod arrays excited by intense femtosecond laser pulses“. In: *Physical Review B* 83 (2011), p. 035408 (cit. on pp. 4, 49).
- [Moore95] C. I. Moore, J. P. Knauer, and D. D. Meyerhofer. „Observation of the Transition from Thomson to Compton Scattering in Multiphoton Interactions with Low-Energy Electrons“. In: *Physical Review Letters* 74.13 (1995), pp. 2439–2442 (cit. on p. 13).
- [More82] R. M. More. „Electronic energy-levels in dense plasmas“. In: *Journal of Quantitative Spectroscopy and Radiative Transfer* 27.3 (1982), pp. 345–357 (cit. on p. 36).
- [Mulser12] P. Mulser, S. M. Weng, and Tatyana Liseykina. „Analysis of the Brunel model and resulting hot electron spectra“. In: *Physics of Plasmas* 19.4 (2012), p. 043301 (cit. on p. 48).
- [Neumayer09] P. Neumayer, H. J. Lee, D. Offerman, E. Shipton, A. Kemp, A. L. Kritcher, T. Döppner, C. A. Back, and S. H. Glenzer. „Isochoric heating of reduced mass targets by ultra-intense laser produced relativistic electrons“. In: *High Energy Density Physics* 5.4 (2009), pp. 244–248 (cit. on p. 84).
- [Neumayer10] P. Neumayer, B. Aurand, M. Basko, B. Ecker, P. Gibbon, D. C. Hochhaus, A. Karmakar, E. Kazakov, T. Kühl, C. Labaune, O. Rosmej, An. Tauschwitz, B. Zielbauer, and D. Zimmer. „The role of hot electron refluxing in laser-generated K-alpha sources“. In: *Physics of Plasmas* 17.10 (2010), p. 103103 (cit. on p. 51).
- [Nishikawa04] T. Nishikawa, S. Suzuki, Y. Watanabe, O. Zhou, and H. Nakano. „Efficient water-window X-ray pulse generation from femtosecond-laser-produced plasma by using a carbon nanotube target“. In: *Applied Physics B* 78.7 (2004), pp. 885–890 (cit. on p. 4).

- [Park06] H.-S. Park, D. M. Chambers, H.-K. Chung, et al. „High-energy  $K_{\alpha}$  radiography using high-intensity, short-pulse lasers“. In: *Physics of Plasmas* 13.5 (2006), p. 056309 (cit. on p. 41).
- [Park08] H.-S. Park, B. R. Maddox, E. Giraldez, et al. „High-resolution 17-75 keV backlighters for high energy density experiments“. In: *Physics of Plasmas* 15.7 (2008), p. 072705 (cit. on p. 41).
- [Perelomov66] A. M. Perelomov, V. S. Popov, and M. V. Terent'ev. „Ionization of atoms in an alternating electric field“. In: *JETP (Russian original - ZhETF, Vol. 50, No. 5, 1966)* 23.5 (1966), p. 924 (cit. on pp. 10, 69, 71, 86).
- [Pfeifer06] T. Pfeifer, C. Spielmann, and G. Gerber. „Femtosecond X-ray science“. In: *Reports on Progress in Physics* 69.2 (2006), pp. 443–505 (cit. on p. 3).
- [Porquet10] D. Porquet, J. Dubau, and N. Grosso. „He-like Ions as Practical Astrophysical Plasma Diagnostics: From Stellar Coronae to Active Galactic Nuclei“. In: *Space Science Reviews* 157.1-4 (2010), pp. 103–134 (cit. on p. 102).
- [Povarnitsyn13] M. E. Povarnitsyn, N. E. Andreev, P. R. Levashov, K. V. Khishchenko, D. A. Kim, V. G. Novikov, and O. N. Rosmej. „Laser irradiation of thin films: Effect of energy transformation“. In: *Laser and Particle Beams* 31.4 (2013), pp. 663–671 (cit. on p. 60).
- [Pugachev16] L. P. Pugachev, N. E. Andreev, P. R. Levashov, and O. N. Rosmej. „Acceleration of electrons under the action of petawatt-class laser pulses onto foam targets“. In: *Nuclear Instruments and Methods in Physics Research Section A: Accelerators, Spectrometers, Detectors and Associated Equipment* 829 (2016). 2nd European Advanced Accelerator Concepts Workshop - EAAC 2015, pp. 88–93 (cit. on p. 56).
- [Pukhov99] A. Pukhov. „Three-dimensional electromagnetic relativistic particle-in-cell code VLPL (Virtual Laser Plasma Lab)“. In: *Journal of Plasma Physics* 61.3 (1999), pp. 425–433 (cit. on pp. 27, 87).
- [Purvis13] M. A. Purvis, V. N. Shlyaptsev, R. Hollinger, C. Bargsten, A. Pukhov, A. Prieto, Y. Wang, B. M. Luther, L. Yin, S. Wang, and J. J. Rocca. „Relativistic plasma nanophotonics for ultrahigh energy density physics“. In: *Nature Photonics* 7 (2013), p. 796 (cit. on pp. 4, 5, 42, 62, 63, 67, 69).
- [Rajeev02] P. P. Rajeev, S. Banerjee, A. S. Sandhu, R. C. Issac, L. C. Tribedi, and G. R. Kumar. „Role of surface roughness in hard-X-ray emission from femtosecond-laser-produced copper plasmas“. In: *Physical Review A* 65 (2002), p. 052903 (cit. on pp. 4, 41).
- [Rajeev03] P. P. Rajeev, P. Taneja, P. Ayyub, A. S. Sandhu, and G. R. Kumar. „Metal nanoplasmas as bright sources of hard X-ray pulses“. In: *Physical Review Letters* 90 (2003), p. 115002 (cit. on pp. 4, 41).

- [Ralchenko15] Y. Ralchenko. *Introduction to atomic data and spectroscopy*, [Online]. 2015 Joint ICTP-IAEA Advanced School and Workshop on Modern Methods in Plasma Spectroscopy. **2015** (cit. on p. 28).
- [Ralchenko16] Y. Ralchenko, ed. *Modern Methods in Collisional-Radiative Modeling of Plasmas*. Springer International Publishing, **2016** (cit. on p. 102).
- [Rassuchine09] J. Rassuchine, E. d’Humières, S. D. Baton, et al. „Enhanced hot-electron localization and heating in high-contrast ultraintense laser irradiation of microcone targets“. In: *Physical Review E* 79.3 (**2009**) (cit. on p. 4).
- [Regemorter62] H. van Regemorter. „Rate of collisional excitation in stellar atmospheres.“ In: *Astrophysical Journal* 136 (**1962**), p. 906 (cit. on p. 31).
- [Remington15] B. A. Remington, R. E. Rudd, and J. S. Wark. „From microjoules to megajoules and kilobars to gigabars: Probing matter at extreme states of deformation“. In: *Physics of Plasmas* 22.9 (**2015**), p. 090501 (cit. on p. 41).
- [Remington99] B. A. Remington. „Modeling Astrophysical Phenomena in the Laboratory with Intense Lasers“. In: *Science* 284.5419 (**1999**), pp. 1488–1493 (cit. on p. 3).
- [Roedel10] C. Rödel, M. Heyer, M. Behmke, M. Kübel, O. Jäckel, W. Ziegler, D. Ehrhart, M. C. Kaluza, and G. G. Paulus. „High repetition rate plasma mirror for temporal contrast enhancement of terawatt femtosecond laser pulses by three orders of magnitude“. In: *Applied Physics B* 103.2 (**2010**), pp. 295–302 (cit. on p. 26).
- [Rosmej17] O. N. Rosmej. *Röntgenstrahlung im Universum und Labor*, [Lecture scripts]. Goethe-Universität Frankfurt. **2016** (cit. on p. 28).
- [Rosmej18] O. N. Rosmej, Z. Samsonova, S. Höfer, et al. „Generation of keV hot near-solid density plasma states at high contrast laser-matter interaction“. In: *Physics of Plasmas* 25.8 (**2018**), p. 083103 (cit. on pp. 47, 55, 62, 71).
- [Rosmej95] O. N. Rosmej and F. B. Rosmej. „The diagnostic ratio of the intercombination and resonance lines of He-like ions: influence of energetic electrons and non-stationarity“. In: *Nuclear Instruments and Methods in Physics Research Section B: Beam Interactions with Materials and Atoms* 98.1 (**1995**), pp. 37–40 (cit. on p. 59).
- [Rosmej98] F. B. Rosmej and J. Abdallah. „Blue satellite structure near  $\text{He}_\alpha$  and  $\text{He}_\beta$  and redistribution of level populations“. In: *Physics Letters A* 245.6 (**1998**), pp. 548–554 (cit. on p. 102).
- [Roth13] M. Roth, D. Jung, K. Falk, et al. „Bright Laser-Driven Neutron Source Based on the Relativistic Transparency of Solids“. In: *Physical Review Letters* 110.4 (**2013**) (cit. on p. 3).

- [Roth14] M. Roth and M. Schollmeier. „Ion Acceleration - Target Normal Sheath Acceleration“. In: *CERN Yellow Reports 1.0* (2014), p. 231 (cit. on pp. 24, 73).
- [Salzmann02] D. Salzmann, Ch. Reich, I. Uschmann, E. Förster, and P. Gibbon. „Theory of  $K_{\alpha}$  generation by femtosecond laser-produced hot electrons in thin foils“. In: *Physical Review E* 65 (2002), p. 036402 (cit. on p. 50).
- [Salzmann98] D. Salzmann. *Atomic Physics in Hot Plasmas. International series on monographs on physics*. Oxford University Press, 1998 (cit. on pp. 28, 29, 36).
- [Samsonova17] Z. Samsonova, S. Höfer, A. Hoffmann, B. Landgraf, M. Zürich, I. Uschmann, D. Khaghani, O. Rosmej, P. Neumayer, R. Röder, L. Trefflich, C. Ronning, E. Förster, C. Spielmann, and D. Kartashov. „X-ray emission generated by laser-produced plasmas from dielectric nanostructured targets“. In: *AIP Conference Proceedings* 1811 (2017), p. 180001 (cit. on pp. 55, 67).
- [Samsonova18] Z. Samsonova, S. Höfer, R. Hollinger, T. Kämpfer, I. Uschmann, R. Röder, L. Trefflich, O. Rosmej, E. Förster, C. Ronning, D. Kartashov, and C. Spielmann. „Hard X-ray generation from ZnO nanowire targets in a non-relativistic regime of laser-solid interactions“. In: *Applied Sciences* 8.10 (2018), p. 1728 (cit. on p. 40).
- [Samsonova19] Z. Samsonova, S. Höfer, V. Kaymak, S. Ališauskas, V. Shumakova, A. Pugžlys, A. Baltuška, T. Siefke, S. Kroker, A. Pukhov, O. Rosmej, I. Uschmann, C. Spielmann, and D. Kartashov. „Relativistic interaction of long-wavelength ultrashort laser pulses with nanowires“. In: *Physical Review X* (submitted) (2018) (cit. on p. 77).
- [Sarkar17] D. Sarkar, P. K. Singh, G. Cristoforetti, A. Adak, G. Chatterjee, M. Shaikh, A. D. Lad, P. Londrillo, G. D'Arrigo, J. Jha, M. Krishnamurthy, L. A. Gizzi, and G. R. Kumar. „Silicon nanowire based high brightness, pulsed relativistic electron source“. In: *APL Photonics* 2.6 (2017), p. 066105 (cit. on p. 4).
- [Schollmeier06] M. Schollmeier, G. Rodríguez Prieto, F. B. Rosmej, G. Schaumann, A. Blazevic, O. N. Rosmej, and M. Roth. „Investigation of laser-produced chlorine plasma radiation for non-monochromatic X-ray scattering experiments“. In: *Laser and Particle Beams* 24.03 (2006) (cit. on pp. 58, 102).
- [Schwoerer01] H. Schwoerer, P. Gibbon, S. Düsterer, R. Behrens, C. Ziener, C. Reich, and R. Sauerbrey. „MeV X Rays and photoneutrons from femtosecond laser-produced plasmas“. In: *Physical Review Letters* 86 (2001), pp. 2317–2320 (cit. on p. 41).

- [Scott15] G. G. Scott, V. Bagnoud, C. Brabetz, R. J. Clarke, J. S. Green, R. I. Heathcote, H. W. Powell, B. Zielbauer, T. D. Arber, P. McKenna, and D. Neely. „Optimization of plasma mirror reflectivity and optical quality using double laser pulses“. In: *New Journal of Physics* 17.3 (2015), p. 033027 (cit. on p. 26).
- [Sherlock09] M. Sherlock. „Universal scaling of the electron distribution function in one-dimensional simulations of relativistic laser-plasma interactions“. In: *Physics of Plasmas* 16.10 (2009), p. 103101 (cit. on p. 47).
- [Shukla17] C. Shukla and A. Das. „Observation of enhanced absorption of laser radiation by nanostructured targets in PIC simulations“. In: *Physics of Plasmas* 24.9 (2017), p. 093118 (cit. on p. 20).
- [Shumakova18] V. Shumakova, S. Ališauskas, P. Malevich, C. Gollner, A. Baltuška, D. Kartashov, A. M. Zheltikov, A. V. Mitrofanov, A. A. Voronin, D. A. Sidorov-Biryukov, and A. Pugžlys. „Filamentation of mid-IR pulses in ambient air in the vicinity of molecular resonances“. In: *Optics Letters* 43.9 (2018), p. 2185 (cit. on p. 80).
- [Silies09] M. Silies, H. Witte, S. Linden, J. Kutzner, I. Uschmann, E. Förster, and H. Zacharias. „Table-top kHz hard X-ray source with ultrashort pulse duration for time-resolved X-ray diffraction“. In: *Applied Physics A* 96.1 (2009), pp. 59–67 (cit. on p. 41).
- [Sjoegren03] A. Sjögren, M. Harbst, C.-G. Wahlström, S. Svanberg, and C. Olsson. „High-repetition-rate, hard X-ray radiation from a laser-produced plasma: Photon yield and application considerations“. In: *Review of Scientific Instruments* 74.4 (2003), pp. 2300–2311 (cit. on p. 45).
- [Skinner72] D. R. Skinner and R. E. Whitcher. „Measurement of the radius of a high-power laser beam near the focus of a lens“. In: *Journal of Physics E: Scientific Instruments* 5.3 (1972), pp. 237–238 (cit. on p. 81).
- [Spitzer53] L. Spitzer and R. Härm. „Transport phenomena in a completely ionized gas“. In: *Physical Review* 89 (1953), pp. 977–981 (cit. on p. 20).
- [Stambulchik08] E. Stambulchik and Y. Maron. „Stark effect of high- $n$  hydrogen-like transitions: quasi-contiguous approximation“. In: *Journal of Physics B: Atomic, Molecular and Optical Physics* 41.9 (2008), p. 095703 (cit. on p. 72).
- [Stambulchik11] E. Stambulchik and Y. Maron. „Plasma formulary interactive“. In: *Journal of Instrumentation* 6.10 (2011), P10009 (cit. on p. 37).
- [Strickland85] D. Strickland and G. Mourou. „Compression of amplified chirped optical pulses“. In: *Optics Communications* 56.3 (1985), pp. 219–221 (cit. on pp. 3, 23).
- [Suckewer09] S. Suckewer and P. Jaeglé. „X-Ray laser: past, present, and future“. In: *Laser Physics Letters* 6.6 (2009), pp. 411–436 (cit. on p. 3).



- [Tata18] S. Tata, A. Mondal, S. Sarkar, J. Jha, Y. Ved, A. D. Lad, J. Colgan, J. Pasley, and M. Krishnamurthy. „Recombination of protons accelerated by a high intensity high contrast laser“. In: *Physical Review Letters* 121 (2018), p. 134801 (cit. on pp. 74, 75).
- [Umstadter03] D. Umstadter. „Relativistic laser-plasma interactions“. In: *Journal of Physics D: Applied Physics* 36.8 (2003), R151 (cit. on p. 41).
- [Uschmann09] I. Uschmann, T. Kämpfer, F. Zamponi, A. Lübcke, U. Zastra, R. Loetzsch, S. Höfer, A. Morak, and E. Förster. „Investigation of fast processes in condensed matter by time-resolved X-ray diffraction“. In: *Applied Physics A* 96.1 (2009), pp. 91–98 (cit. on p. 47).
- [Voronin17] A. Voronin and M. Zheltikov. „The generalized Sellmeier equation for air“. In: *Scientific Reports* 7 (2017), srep46111 (cit. on p. 81).
- [Wagner64] R. S. Wagner and W. C. Ellis. „Vapor-liquid-solid mechanism of single crystal growth“. In: *Applied Physics Letters* 4.5 (1964), pp. 89–90 (cit. on p. 104).
- [Wang17] F. Wang, B. Han, D. Salzmann, and G. Zhao. „Contribution of satellite lines to temperature diagnostics with He-like triplet lines in photoionized plasma“. In: *Physics of Plasmas* 24.4 (2017), p. 041403 (cit. on p. 102).
- [Weisshaupt14] J. Weisshaupt, V. Juvé, M. Holtz, S. Ku, M. Woerner, T. Elsaesser, S. Ališauskas, A. Pugžlys, and A. Baltuška. „High-brightness tabletop hard X-ray source driven by sub-100-femtosecond mid-infrared pulses“. In: *Nature Photonics* 8.12 (2014), pp. 927–930 (cit. on p. 80).
- [Weisshaupt15] J. Weisshaupt, V. Juvé, M. Holtz, M. Woerner, and T. Elsaesser. „Theoretical analysis of hard X-ray generation by nonperturbative interaction of ultrashort light pulses with a metal“. In: *Structural Dynamics* 2.2 (2015), p. 024102 (cit. on pp. 79, 80, 86, 94).
- [Wilks97] S. C. Wilks and W. L. Kruer. „Absorption of ultrashort, ultra-intense laser light by solids and overdense plasmas“. In: *IEEE Journal of Quantum Electronics* 33.11 (1997), pp. 1954–1968 (cit. on p. 16).
- [Wu08] J. Wu and C. Guo. „Wavelength effects on strong-field single electron ionization“. In: *Adv. Studies Theor. Phys.* 2.6 (2008), pp. 271–279 (cit. on p. 78).
- [Yang02] P. Yang, H. Yan, S. Mao, R. Russo, J. Johnson, R. Saykally, N. Morris, J. Pham, R. He, and H.-J. Choi. „Controlled Growth of ZnO Nanowires and Their Optical Properties“. In: *Advanced Functional Materials* 12.5 (2002), pp. 323–331 (cit. on p. 104).

- [Young98] B. K. F. Young, B. G. Wilson, D. F. Price, and R. E. Stewart. „Measurement of x-ray emission and thermal transport in near-solid-density plasmas heated by 130 fs laser pulses“. In: *Physical Review E* 58.4 (1998), pp. 4929–4936 (cit. on p. 3).
- [Zamponi09] F. Zamponi, Z. Ansari, C. v. Korff Schmising, P. Rothhardt, N. Zavoronkov, M. Woerner, T. Elsaesser, M. Bargheer, T. Trobitzsch-Ryll, and M. Haschke. „Femtosecond hard X-ray plasma sources with a kilohertz repetition rate“. In: *Applied Physics A* 96.1 (2009), pp. 51–58 (cit. on pp. 41, 47).
- [Zastrau10a] U. Zastrau, P. Audebert, V. Bernshtam, et al. „Temperature and  $K_{\alpha}$ -yield radial distributions in laser-produced solid-density plasmas imaged with ultrahigh-resolution X-ray spectroscopy“. In: *Physical Review E* 81 (2010), p. 026406 (cit. on p. 84).
- [Zepf98] M. Zepf, G. D. Tsakiris, G. Pretzler, I. Watts, D. M. Chambers, P. A. Norreys, U. Andiel, A. E. Dangor, K. Eidmann, C. Gahn, A. Machacek, J. S. Wark, and K. Witte. „Role of the plasma scale length in the harmonic generation from solid targets“. In: *Physical Review E* 58 (1998), R5253–R5256 (cit. on p. 24).
- [Zhang03] R.-Q. Zhang, Y. Lifshitz, and S.-T. Lee. „Oxide-assisted growth of semi-conducting nanowires“. In: *Advanced Materials* 15.78 (2003), pp. 635–640 (cit. on p. 104).
- [Zhidkov00] A. Zhidkov, A. Sasaki, T. Utsumi, I. Fukumoto, T. Tajima, F. Saito, Y. Hironaka, K. G. Nakamura, K. Kondo, and M. Yoshida. „Prepulse effects on the interaction of intense femtosecond laser pulses with high-Z solids“. In: *Physical Review E* 62 (2000), pp. 7232–7240 (cit. on p. 24).
- [Zielbauer11] B. Zielbauer, T. Kuehl, B. Aurand, et al. *X-ray laser developments at PHELIX*. Springer Netherlands, 2011, pp. 31–38 (cit. on p. 3).
- [Ziener02] C. Ziener, I. Uschmann, G. Stobrawa, C. Reich, P. Gibbon, T. Feurer, A. Morak, S. Düsterer, H. Schwoerer, E. Förster, and R. Sauerbrey. „Optimization of  $K_{\alpha}$  bursts for photon energies between 1.7 and 7 keV produced by femtosecond-laser-produced plasmas of different scale length“. In: *Physical Review E* 65 (2002), p. 066411 (cit. on p. 24).
- [Zigler11] A. Zigler, T. Palchan, N. Bruner, E. Schleifer, S. Eisenmann, M. Botton, Z. Henis, S. A. Pikuz, A. Y. Faenov, D. Gordon, and P. Sprangle. „5.5–7.5 MeV proton generation by a moderate-intensity ultrashort-pulse laser interaction with  $H_2O$  nanowire targets“. In: *Physical Review Letters* 106.13 (2011) (cit. on p. 4).

## Websites

- [ESTAR] M. J. Berger, J. S. Coursey, M. A. Zucker, and J. Chang. *ESTAR, PSTAR, and ASTAR: Computer programs for calculating stopping-power and range tables for electrons, protons, and helium Ions (version 1.2.3)*. [Online]. English. **2005**. URL: <https://www.nist.gov/pml/stopping-power-range-tables-electrons-protons-and-helium-ions> (cit. on pp. 52, 53).
- [NIST] A. Kramida, Yu. Ralchenko, J. Reader, and NIST ASD Team. *NIST Atomic Spectra Database (version 5.5.6)*, [Online]. **2018**. URL: <https://physics.nist.gov/asd> (cit. on pp. 11, 86).
- [X-rayDataBooklet] Editors: A. C. Thompson and D. Vaughan. *X-ray data booklet*. 3rd Edition. **2009**. URL: <http://xdb.lbl.gov/> (cit. on p. 86).

# List of Figures

1.1	Illustration of the interaction of an intense laser pulse with a nanowire solid target. . . . .	5
2.1	Schematic picture of different regimes of the optical ionization: (a) multiphoton ionization, (b) above-threshold ionization, and (c) tunnel and barrier-suppression ionization. $V$ is the effective potential which, in the cases of TI and BS, is equal to the ionization potential $I_p$ or falls below it at a certain position, respectively. . . . .	9
2.2	The collisional cross-sections for Li-like and H-like ions ((a) Si, (b) Zn) calculated according to the Lotz formula (Eq. 2.2). . . . .	11
2.3	Schematic of the heating mechanisms: (a) Brunel heating, (b) $\vec{j} \times \vec{B}$ mechanism. . . . .	18
2.4	Schematic illustration of the temporal structure of a typical (green line) and an ideal Gaussian (shaded orange area) pulses. . . . .	24
2.5	JETi-40 laser pulse contrast. The measured third-order correlation trace of the fundamental laser pulse. The pulse contrast was calculated for the frequency-doubled laser pulse (SHG, 20% efficiency). The level of residual radiation at 800 nm (with two dichroic mirrors used) is shown. (Courtesy of Dr. Alexander Sävert.) . . . . .	25
2.6	The PIC computational cycle. The index $i$ denotes a macro-particle. . .	27
2.7	Schematic diagram of (a) radiative recombination, (b) electron impact (or collisional) deexcitation and (c) three-body recombination. . . . .	32
2.8	Schematic diagram of (a) dielectronic capture, (b) dielectronic recombination (Li-like dielectronic satellite) and (c) autoionization.) . . . . .	34
3.1	SEM images of the investigated ZnO nanowire targets: (a) vertically oriented and (b) randomly oriented NWs. . . . .	42

3.2	(a) The pulse contrast measured with a third-order cross-correlator Sequoia. Adapted from [Hoefer14]. (b) The beam profile in the focal plane. . . . .	43
3.3	(b) Interior of the vacuum chamber (photo). (a) The scheme of the experimental setup. The CCD 3 camera recording the X-rays reflected from the quartz (SiO <sub>2</sub> ) crystal detected also signal not reflected from the crystal. . . . .	44
3.4	The laser-target interaction geometry for (a) vertically and (b) randomly oriented NW targets (ZnO). $\vec{E}_p$ and $\vec{E}_s$ – p- and s-polarized electric fields of the incoming laser pulse with $\vec{k}$ , respectively. $\vec{n}$ – a normal vector of the target surface. . . . .	45
3.5	The X-ray spectra from the polished and nanowire ZnO targets for (a) p-polarization and (b) s-polarization measured by CCD 1 in single-photon counting mode. The solid blue lines correspond to the exponential fits providing an estimation of the electron temperature $T_e$ . . . . .	47
3.6	The hard X-ray spectra from the polished and nanowire ZnO targets for (a) p-polarization and (b) s-polarization measured by Timepix detector. The ratios of the hard X-ray flux from NW and polished targets are given for the marked (blue) energy range. The spectra were fitted with an exponential function (solid blue lines) providing an estimation of the electron “hot” temperatures $T_e$ . . . . .	48
3.7	The K-shell emission and K <sub>α</sub> -doublet ( <i>Insets</i> ) from ZnO targets (polished (black), vertically (green) and randomly (orange) oriented NW targets) detected with LiF and SiO <sub>2</sub> bent crystal spectrometers, respectively. The spectra were obtained from interaction with (a) p-polarized and (b) s-polarized laser pulse. . . . .	50
3.8	The background signal from the polished and nanowire ZnO targets for (a) p-polarization and (b) s-polarization detected by CCD 3 (in quartz crystal spectrometer setup). . . . .	52
3.9	(a) The test measurements of the background signal: with and without Al foil blocking the exit of the vacuum chamber. (b) The transmission of X-ray photons through a 2 mm-thick Al foil. . . . .	52

4.1	K-shell emission spectrum from a planar Ti foil measured with the HOPG crystal spectrometer (the intensity is in PSL units (Photo Stimulated Fluorescence)). The shaded blue part of the spectrum corresponds to the emission from the densest and hottest plasma region. <i>Inset</i> : The spectrum recorded on the image plate before the reconstruction. . . . .	58
4.2	The measured and the simulated X-ray spectra for the Ti foil. The simulations in FLYCHK [Chung05] are performed for (a) a steady-state approximation and (b) a transient-state plasma. The fine structure of the spectra from FLYCHK (no convolution with instrument function) visualizes the contribution of the various line groups into the final spectra (orange line). . . . .	59
4.3	The evolution of the Ti ion charge states calculated with FLYCHK code. Only the highly charged states are shown (Ti <sup>18+</sup> - Ti <sup>21+</sup> ). . . . .	61
4.4	Hydrodynamic simulations of the bulk electron temperature distribution $T_{bulk}$ over the Fe target depth for different times during and after the laser pulse. The shaded areas correspond to the regions of the target from where K-shell emission in certain ion species may originate. . . . .	61
4.5	(a) Simplified scheme of the setup for the experiments at JETi-40. (b) Vacuum chamber with the Thomson parabola setup. . . . .	64
4.6	The diagnostics setup (top view): two crystal spectrometers (KAP and LiF crystal spectrometers), a Timepix detector, a Thomson parabola, and a focus diagnostics setup. . . . .	65
4.7	SEM images of some of the investigated ZnO nanowire samples (the samples were tilted by 20°). . . . .	66
4.8	SEM images of one the investigated Si nanowire samples: (a) side view; (b) the sample was tilted by 30°. . . . .	66
4.9	(a) Spectra of K-shell emission from the polished and the nanowire ZnO targets (normal incidence). (b) The measured and simulated X-ray spectra for the Si nanowire target. The simulations are performed for a steady-state approximation. . . . .	68
4.10	(a) Spectra of K-shell emission from the polished and the nanowire ZnO targets (45° incidence). (b) Hard X-ray emission spectra with an exponential fit. . . . .	70

4.11	(a) Ratio of the flux obtained from the nanowire sample to the flux obtained with the polished sample ( $K_{\alpha}$ , $He_{\alpha}$ and bremsstrahlung emission). (b) $Zn^{+}$ ion spectra measured with the polished and the nanowire ZnO samples at different values of the normalized vector potential $a_0$ . . . . .	71
4.12	(a) Spectra of K-shell line emission from the polished and the nanowire ZnO targets. (b) Hard X-ray emission spectra with an exponential fit. . . . .	71
4.13	Emission spectra of He- and H-like Rydberg ions measured from the polished and nanowire Si targets. The spectrum from the polished target is 5x magnified. . . . .	73
4.14	MCP images of the ion spectra recorded from the polished (a) and nanowire (b) Si targets. The traces of the identified ions (Si and impurity elements) are marked. . . . .	74
4.15	Reconstructed ion spectra from the polished and nanowire Si targets: (a) $Si^{+}$ ions, (b) $C^{+}$ ions. . . . .	75
4.16	Scheme of ion acceleration and neutralization with a cold bunch of co-propagating electrons. Adapted from [Tata18]. . . . .	75
5.1	Vacuum chamber with the experimental setup. . . . .	80
5.2	Retrieved pulse parameters in (a) the time and (b) the frequency domains for the idler of OPCPA. . . . .	82
5.3	(a) Spectra of K-shell line emission from the polished and the nanowire array ZnO targets.(b) Hard X-ray emission spectra with exponential fits. The spectra were measured for a $0^{\circ}$ incidence. . . . .	83
5.4	Spectra of K-shell line emission from the polished (black line) and the nanowire array (green line) Si targets. <i>Inset</i> : The same spectra in logarithmic scale. . . . .	85
5.5	Hard X-ray emission spectra with an exponential fit corresponding to the hot electron temperature $T_{hot}$ of $\sim 26$ keV. . . . .	85
5.6	The results of PIC simulations for the spatial distribution of (a) the bulk electron temperature $T_{bulk}$ and $n_e$ (b) electron density for the Si NW target. The time is given with respect to the arrival of the laser peak intensity at the NW tips. . . . .	88

5.7	(a) The temporal evolution of the bulk and hot electron temperatures ( $T_{bulk}$ and $T_{hot}$ ) of the electron fractions averaged over the upper 0.5 $\mu\text{m}$ of the NW. (b) The temporal evolution of the electron density $n_e$ calculated by PIC and FLYCHK simulations (in logarithmic scale). . . . .	89
5.8	(a) The measured and simulated X-ray spectra (time-integrated) for Si NW target. (b) The temporal evolution of the K-shell emission in the spectral region 1.80 - 2.05 keV calculated in FLYCHK. . . . .	90
5.9	(a) The temporal evolution of the relative ion density ( $\text{Si}^{11+}$ , $\text{Si}^{12+}$ , $\text{Si}^{13+}$ ) calculated by FLYCHK. The temporal evolution of the intensity of $\text{He}_\alpha$ (b) and $\text{Ly}_\alpha$ (c) emission lines with/without opacity included. . .	91
5.10	The time evolution of the radiated power (losses) for the hottest and densest region of Si NW target (top 0.5 $\mu\text{m}$ -thick layer) calculated with FLYCHK. . . . .	93
5.11	The results of PIC simulations for the spatial distribution of (a) the bulk electron temperature $T_{bulk}$ and (b) electron density $n_e$ for the polished Si target. The zero moment of time corresponds to the moment of the peak intensity arrival at the surface boundary. . . . .	94
A.1	Simplified level diagram of fine-structure states of He-like ions. . . . .	101
B.1	SEM images of a Si nanowire sample (the sample was tilted by $30^\circ$ ). . . . .	105
C.1	Technical scheme of JETi-40. (Courtesy of JETi laser team.) . . . . .	106
D.1	Photo of the used in the experiments KAP crystal. . . . .	107
D.2	Schematic geometry of a Bragg crystal spectrometer. . . . .	107
D.3	Photo of the used in the experiments HOPG crystal. . . . .	108
D.4	Photo of the used in the experiments LiF crystal. . . . .	109
D.5	Schematic geometry of a von Hamos crystal spectrometer. $\theta_{B \text{ min, max}}$ – possible Bragg angles. . . . .	109
D.6	Photo of the used in the experiments quartz crystal in a holder. . . . .	110
D.7	Schematic geometry of a Johann crystal spectrometer. . . . .	110
E.1	Schematic of the Thomson parabola spectrometer. The ion beam propagates along the z-axis. . . . .	112
F.1	Reconstruction of a Zn spectrum measured with the LiF crystal spectrometer: (a) the original image, (b) the selected area with identified emission lines and (c) the resulting spectrum. . . . .	113



G.1	(a) Optical microscope image and (b) SEM image of the ZnO nanowire target. . . . .	115
G.2	(a) Optical microscope image and (b) SEM image (with a tilt of 30°) of the ZnO nanowire target. (c) Edge of the damaged spot on the NW target. (d) SEM image of the polished ZnO target. . . . .	115
G.3	(a) Optical microscope image and (b) SEM image of the ZnO nanowire target. . . . .	116

# List of Tables

2.1	Important atomic processes in plasma relevant to laser-matter interaction. $\rightsquigarrow$ indicates radiative processes. $X^{Z+}$ denotes an ion of type $X$ with charge $Z$ . The symbol $*$ indicates an excited state. $E_{1,2}$ - kinetic energy. . . . .	29
3.1	The mean values of the integrated Zn $K_{\alpha}$ emission for the investigated targets obtained with p- and s-polarized laser pulse. The values are normalized on the integrated Zn $K_{\alpha}$ flux from the polished sample. . .	51
5.1	Focus parameters for the experimental series at OPCPA laser system (3.9 $\mu\text{m}$ ). . . . .	81
5.2	The integrated X-ray flux obtained with ZnO targets in different incidence geometry. Total flux is calculated for the K-shell emission. . . . .	84
E.1	The main parameters of the Thomson parabola spectrometer used in the experiments. . . . .	112

# Selbstständigkeitserklärung

Ich erkläre hiermit ehrenwörtlich, dass ich die vorliegende Arbeit selbständig, ohne unzulässige Hilfe Dritter und ohne Benutzung anderer als der angegebenen Hilfsmittel und Literatur angefertigt habe. Die aus anderen Quellen direkt oder indirekt übernommenen Daten und Konzepte sind unter Angabe der Quelle gekennzeichnet.

Bei der Auswahl und Auswertung folgenden Materials bzw. der Beisteuerung von Material/Daten haben mir die nachstehend aufgeführten Personen in der jeweils beschriebenen Weise entgeltlich/unentgeltlich geholfen:

- Prof. Dr. C. Spielmann, Dr. D. Kartashov und Dr. O. Rosmej mit Diskussion und Interpretation der Resultate;
- Die Gruppe um Prof. Dr. N. E. Andreev mit den Particle-In-Cell und hydrodynamischen Simulationen der Laser-Material-Wechselwirkung (in Kapitel 4);
- M. Sc. V. Kaymak und Prof. Dr. A. Pukhov mit den Particle-In-Cell Simulationen der Laser-Material-Wechselwirkung (in Kapitel 5);
- M. Sc. L. Trefflich, Dr. R. Röder und Prof. Dr. C. Ronning mit der Herstellung der ZnO Nanodrähte;
- M. Sc. T. Siefke und Jun.-Prof. Dr. S. Kroker mit der Herstellung der Si Nanodrähte.

Weitere Personen waren an der inhaltlich-materiellen Erstellung der vorliegenden Arbeit nicht beteiligt. Insbesondere habe ich hierfür nicht die entgeltliche Hilfe von Vermittlungs- bzw. Beratungsdiensten (Promotionsberater oder andere Personen) in Anspruch genommen. Niemand hat von mir unmittelbar oder mittelbar geldwerte Leistungen für Arbeiten erhalten, die im Zusammenhang mit dem Inhalt der vorgelegten Dissertation stehen.

Die Arbeit wurde bisher weder im In- noch im Ausland in gleicher oder ähnlicher Form einer anderen Prüfungsbehörde vorgelegt. Die geltende Promotionsordnung der Physikalisch-Astronomischen Fakultät ist mir bekannt.

Ich versichere ehrenwörtlich, dass ich nach bestem Wissen die reine Wahrheit gesagt und nichts verschwiegen habe.

Jena, den 05.12.2018

Zhanna Samsonova

# Lebenslauf

## PERSÖNLICHE DATEN

---

**Name** *Zhanna Samsonova*  
**Geburtsort und Geburtsdatum** *UdSSR (Oblast Moskau), 11. April 1991*  
**Staatsbürgerschaft** *russisch*

## PROMOTION

---

- Friedrich-Schiller Universität Jena** Mai 2014 - März 2019  
*Wissenschaftliche Mitarbeiterin* *Jena, Deutschland*
- Physikalisch-Astronomische Fakultät \* Institut für Optik und Quantenelektronik (IOQ) \* Lehrstuhl Quantenelektronik
  - Stipendium: Research School of Advanced Photon Science (RS-APS) des Helmholtz-Instituts Jena (2014-2017)
  - Thema der Dissertation: "Relativistic interaction of ultra-short laser pulses with nanostructured solids"

## HOCHSCHULSTUDIUM

---

- Nationale Kernforschungsuniversität "MIFI "** Sept. 2008 - März 2014  
*Dipl.-Phys. Ing. [Diplom eines Spezialisten]* *Moskau, Russland*
- Fakultät: Experimentelle und Theoretische Physik \* Fachrichtung: Laserphysik
  - Preis für die beste wissenschaftliche Arbeit der 7. und 9. Semester
  - Spezialisierung: Physik des kondensierten Stoffzustandes
  - Diplomarbeit: "Pulsed Raman fiber laser operating at 1118 nm for second harmonic generation"

## SCHULBILDUNG

---

- Städtische allgemeinbildende Einrichtung – Pushkin-Lyzeum 6** Sept. 1997 - Juni 2008  
*mittlere (vollendete) Schulbildung* *Oblast Moskau, Russland*
- Abschlusszeugnis mit Auszeichnung

# List of Publications

## Peer-reviewed Journals and Proceedings

Z. Samsonova, S. Höfer, V. Kaymak, S. Ališauskas, V. Shumakova, A. Pugžlys, A. Baltuška, T. Siefke, S. Kroker, A. Pukhov, O. Rosmej, I. Uschmann, C. Spielmann, and D. Kartashov, "*Relativistic interaction of long-wavelength ultrashort laser pulses with nanowires*," arXiv preprint arXiv:1809.08882, submitted to Physical Review X (2018).

Z. Samsonova, S. Höfer, R. Hollinger, T. Kämpfer, I. Uschmann, R. Röder, L. Trefflich, O. Rosmej, E. Förster, C. Ronning, D. Kartashov, and Christian Spielmann, "*Hard X-ray generation from ZnO nanowire targets in a non-relativistic regime of laser-solid interactions*," Applied Sciences **8**, 10, 1728 (2018). DOI: 10.3390/app8101728.

Z. Samsonova, D. Kartashov, C. Spielmann, S. Bodrov, A. Murzanev, V. Jukna, M. Petrarca, A. Couairon, and P. Polynkin, "*Measurements of fluence profiles in femtosecond laser sparks and superfilaments in air*," Physical Review A **97**, 063841 (2018). DOI: 10.1103/PhysRevA.97.063841.

O. Rosmej, Z. Samsonova, S. Höfer, D. Kartashov, C. Arda, D. Khaghani, A. Schoenlein, S. Zähler, A. Hoffmann, R. Loetzsch, A. Saevart, I. Uschmann, M. E. Povarnitsyn, N. E. Andreev, L. P. Pugachev, M. C. Kaluza, and C. Spielmann, "*Generation of keV hot near-solid density plasma states at high contrast laser-matter interaction*," Physics of Plasmas **25**, 083103 (2018). DOI: 10.1063/1.5027463.

R. Hollinger, Z. Samsonova, D. Gupta, C. Spielmann, R. Röder, L. Trefflich, C. Ronning, and D. Kartashov, "*Enhanced absorption and cavity effects of three-photon pumped ZnO nanowires*," Applied Physics Letters **111**, 213106 (2017). DOI: 10.1063/1.4999690.

Z. Samsonova, S. Höfer, A. Hoffmann, B. Landgraf, M. Zürich, I. Uschmann, D. Khaghani, O. Rosmej, P. Neumayer, R. Röder, L. Trefflich, C. Ronning, E. Förster, C. Spielmann, and D. Kartashov, "*X-ray emission generated by laser-produced plasmas from dielectric nanostructured targets*," AIP Conference Proceedings **1811**, 180001 (2017). DOI: 10.1063/1.4975743.

B. Landgraf, A. Hoffmann, D. Kartashov, F. Gärtner, Z. Samsonova, P. Polynkin, J. Jacoby, T. Kühl, and C. Spielmann, "Generation of multi-millijoule red-shifted pulses for seeding stimulated Raman backscattering amplifiers," *Optics Express* **23**, 7400 (2015). DOI: 10.1364/OE.23.007400.

## Scientific and Annual reports

Z. Samsonova, S. Höfer, S. Ališauskas, V. Shumakova, A. Pugžlys, A. Baltuška, T. Siefke, S. Kroker, O. Rosmej, A. Pukhov, I. Uschmann, C. Spielmann, and D. Kartashov, "Relativistic interaction of mid-infrared laser pulses with nanowire targets: towards a novel laser-plasma interaction regime," *Helmholtz Institute Jena Annual Reports 2017*, p. 38 (2018).

Z. Samsonova, S. Ališauskas, A. Baltuška, E. Förster, S. Höfer, D. Kartashov, V. Kaymak, S. Kroker, A. Pugžlys, A. Pukhov, C. Ronning, C. Spielmann, L. Trefflich, and I. Uschmann, "X-ray emission from a laser-induced plasma with ZnO nanostructured targets," *Helmholtz Institute Jena Annual Reports 2016*, p. 53 (2017).

S. Zähler, A. Schoenlein, O. Rosmej, Z. Samsonova, D. Khaghani, C. Arda, N. E. Andreev, A. Hoffmann, S. Höfer, M. C. Kaluza, D. Kartashov, L. P. Pugachev, I. Uschmann, and C. Spielmann, "Generation of keV hot near-solid density plasma states at high contrast laser-matter interaction<sup>1</sup>," *GSI Scientific Report 2016*, Darmstadt: GSI **486**, p. 288 (2017). DOI:10.15120/GR-2017-1.

Z. Samsonova, E. Förster, S. Höfer, A. Hoffmann, D. Kartashov, D. Khaghani, B. Landgraf, P. Neumayer, R. Röder, C. Ronning, O. Rosmej, C. Spielmann, L. Trefflich, I. Uschmann, and M. Zürch, "X-ray emission from laser-induced plasma with ZnO nanostructured targets<sup>2</sup>," *GSI Scientific Report 2015*, Darmstadt: GSI **395**, p. 182 (2016). DOI:10.15120/GR-2016-1.

B. Landgraf, F. Gärtner, D. Kartashov, A. Hoffmann, Z. Samsonova, G. Vieux, G. McKendrick, D. Jaroszynski, J. Jacoby, T. Kühl, and C. Spielmann, "Technical report

---

<sup>1</sup>This report has been also published in the HI Jena Annual Report 2016 and News and Reports from High Energy Density generated by Heavy Ion and Laser Beams 2016.

<sup>2</sup>This report has been also published in the HI Jena Annual Report 2015 and in News and Reports from High Energy Density generated by Heavy Ion and Laser Beams 2015.

for P073, *stimulated Raman Backscattering at PHELIX*<sup>3</sup>," GSI Scientific Reports 2015, Darmstadt: GSI 395, p. 173 (2016). DOI: 10.15120/GR-2016-1.

Z. Samsonova, R. Hollinger, D. Kartashov, M. Zürch, R. Röder, L. Trefflich, O. Rosmej, P. Neumayer, C. Ronning, and C. Spielmann, "*Interaction of ZnO nanostructured targets with intense laser pulses*," Helmholtz Institute Jena Annual Reports 2014, p. 60 (2015).

B. Landgraf, A. Hoffmann, D. Kartashov, F. Gärtner, Z. Samsonova, P. Polynkin, J. Jacoby, T. Kühl, and C. Spielmann, "*Generation of multimillijoule redshifted beams for stimulated Raman scattering*<sup>4</sup>," GSI Scientific Report 2014, Darmstadt: GSI 395, p. 277 (2015). DOI: 10.15120/GR-2015-1-APPA-MML-PP-03.

---

<sup>3</sup>This report has been also published in the HI Jena Annual Report 2015.

<sup>4</sup>This report has been also published in the HI Jena Annual Report 2014.



# List of conferences

## Oral presentations

### **8th Conference of the International Committee on Ultrahigh Intensity Lasers (ICUIL)**

Sept 2018, Lindau, Germany

*"Wavelength dependence the relativistic interaction of ultrashort laser pulses with nanostructured solids"*

### **7th International doctoral conference on optics and photonics (DoKDoK)**

Sept 2018, Friedrichroda, Germany

*"Fluence profiles in femtosecond laser sparks and superfilaments in air"*

### **6th International doctoral conference on optics and photonics (DoKDoK)**

Sept 2017, Suhl, Germany

*"Interaction of relativistic mid-infrared laser pulses with nanostructured targets as a novel regime of interaction"*

### **Conference on Lasers and Electro-Optics/Europe (CLEO/Europe-EQEC)**

June 2017, München, Germany

*"X-ray emission from nanostructured targets irradiated by a relativistically intense mid-infrared driver"*

### **Frühjahrstagung der Deutschen Physikalischen Gesellschaft (DPG)**

Mar 2017, Bremen, Germany

*"Highly efficient source of  $K_{\alpha}$  radiation driven by relativistic interaction of mid-infrared laser pulses with nanostructured solid targets"*

### **19th International Conference on Atomic Processes in Plasmas**

Apr 2016, Paris, Germany

*"X-ray emission generated by laser-produced plasma from dielectric nanostructured targets"*

**Super Intense Laser-Atom Physics Conference**

Sept 2015, Bordeaux, France

*"Hard X-ray and fast electron generation from dielectric nanostructured targets"*

**Poster presentations**

**International Conference on High Intensity Lasers in Israel (CHILI)**

Dec 2017, Tel-Aviv, Israel

*"Relativistic nanophotonics in long-wavelength regime"*

**10th International Conference on Inertial Fusion Sciences and Applications (IFSA)**

Sept 2017, Saint Malo, France

*"Relativistic interaction of nanostructured solids with short and long wavelength ultra-short laser pulses"*

**Conference on Lasers and Electro-Optics/Europe (CLEO/Europe-EQEC)**

June 2015, Munich, Germany

*"Second harmonic generation from ZnO nanostructured surface by femtosecond laser pulses at near damage threshold intensities"*

# List of seminars

## Invited seminars

**Seminar "Aktuelle Probleme der Angewandten Physik" in the Institute of Applied Physics, Goethe University Frankfurt**

May 2018, Frankfurt am Main, Germany

*"Nanostrukturen unter Laserbeschuss"* with Dr. O. Rosmej

**Plasma Seminar in Weizmann Institute**

Apr 2018, Rehovot, Israel

*"Interaction of the relativistic pulses with structured targets for enhanced production of X-rays and high energy particles"* with Prof. Dr. N. Andreev, Dr. O. Rosmej and Dr. D. Kartashov

**Plasmaphysik Seminar in GSI Helmholtz Centre for Heavy Ion Research**

Apr 2017, Darmstadt, Germany

*"Study of X-ray generation from mid-infrared laser interaction with nanostructured targets"*

**Guest Seminar in the Institute for Theoretical Physics I, Heinrich-Heine-University Düsseldorf**

May 2017, Düsseldorf, Germany

*"Study of X-ray emission generated by ultra-short laser pulses with nanostructured targets"*

## **Other seminars**

### **IOQ Group Seminar**

Jan 2017, Jena, Germany

*"X-Ray emission from nano-structured targets using a mid-infrared driver"*

### **RS-APS Seminar, Helmholtz Institute Jena**

Jan 2016, Jena, Germany

*"Interaction of ultra-short intense laser pulses with ZnO nanostructured targets"*

### **IOQ Group Seminar**

Nov 2015, Jena, Germany

*"Hard X-ray generation by a moderate intensity ultra-short laser pulse interaction with dielectric nanostructured targets"*

### **Abbe School of Photonics Seminar**

June 2015, Jena, Germany

*"Extreme nonlinear optics with nanostructured targets"*

### **IOQ Group Seminar**

Dec 2014, Jena, Germany

*"Development of fiber lasers operating in the visible spectral range"*